Modeling the lamellipodium of motile cells

Formation, stability and strength of membrane protrusions

D I S S E R T A T I O N

zur Erlangung des akademischen Grades

doctor rerum naturalium
(Dr. rer. nat.)
im Fach Biophysik

eingereicht an der
Mathematisch-Naturwissenschaftlichen Fakultät I
Humboldt-Universität zu Berlin

von
Dipl.-Phys. Juliane Zimmermann

Präsident der Humboldt-Universität zu Berlin:
Prof. Dr. Jan-Hendrik Olbertz

Dekan der Mathematisch-Naturwissenschaftlichen Fakultät I:
Prof. Stefan Hecht, Ph.D.

Gutachter:
1. Prof. Dr. Andreas Herrmann
2. Dr. habil. Martin Falcke
3. Prof. Dr. Josef Käs

eingereicht am: 01.11.2012
Tag der mündlichen Prüfung: 24.04.2013

Abstract

Many cells move over surfaces during embryonic development, immune response, wound healing or cancer metastasis by protruding flat lamellipodia into the direction of migration. Although the phenomenon of cell motility has been fascinating scientists for many years, we are only beginning to gain a quantitative understanding. Many issues remain unresolved. Open questions are for example: Why and how do lamellipodia initially form? Why do some cells exhibit stable lamellipodia while others show protruding and retracting lamellipodia or form a lamellipodium that subsequently collapses? Which changes occur inside the lamellipodium during phases of protrusion and retraction? Is the activation of signaling molecules necessary? The force-velocity relation of keratocytes has been measured experimentally. What is the reason for its unexpected concave shape? Why do moving cells first react very sensitively to tiny forces but can then still move at forces that are orders of magnitude larger? How large are the forces that cells can exert on surrounding cells in tissue and what determines the strength of lamellipodia? What are the mechanical properties of the lamellipodium and which structures bring them about?

In this thesis, a mathematical model is developed that contributes substantially to answering those questions. It describes the formation of lamellipodia, their stability, strength and leading edge dynamics. Two regions of the lamellipodium are distinguished in the model. The bulk of the lamellipodium contains a dense cross-linked actin network called actin gel. The newly polymerized tips of the actin filaments at the leading edge constitute a highly dynamic boundary layer called semiflexible region (SR). The forces that single treadmilling actin filaments in the SR exert on the leading edge membrane are calculated, and the balance of forces with viscous and external forces determines the velocity of the leading edge. Specifically, the previously published filament model is supplemented by including retrograde flow in the actin gel, and a feasible description of a variable filament density in the SR due to nucleation of new and capping and severing of existing filaments. With several simplifications, the model is represented by a system of ordinary differential equations for a one dimensional cross-section through the thin lamellipodium.

A stability analysis of the model identifies three qualitatively different parameter regions: with stationary filament density and leading edge motion, oscillatory motion, or a filament density of zero and no leading edge motion. That defines criteria for the existence of stable lamellipodia and allows for describing different cell types. Zero filament density means no stable lamellipodium can exist. However, due to excitability, lamellipodia can still form transiently. The measured subsequent protrusions and retractions of lamellipodia in epithelial cells are very well reproduced by assuming random nucleation of single short filaments from the actin cortex in the excitable regime. The modeling results support ideas on lamellipodium formation, the formation of actin arcs in the lamellum, and show that in principle no signaling is necessary for cycles of protrusion and retraction.

Furthermore, the model results are fitted to the force-velocity relation of keratocytes, which has been measured by placing a flexible scanning force microscopy (SFM)-cantilever into the cell's path of migration. Due to the good agreement between experiment and simulations, a mechanism leading to the characteristic features of the force-velocity relation is suggested. Moreover, properties of the structure of the stable keratocyte lamellipodium, like the length of actin filaments at

the leading edge and the branch point density, can be concluded. It is shown that the force-velocity relation measured with a cantilever is a dynamic phenomenon. A stationary force-velocity relation is predicted that should apply if cells experience a constant force, e.g. exerted by surrounding tissue.

Zusammenfassung

Das Kriechen von Zellen über Oberflächen spielt eine entscheidende Rolle bei lebenswichtigen Prozessen wie der Embryonalentwicklung, der Immunantwort und der Wundheilung, aber auch bei der Metastasenbildung von Tumoren. Die Zellbewegung erfolgt über die Bildung einer flachen Ausstülpung der Zellmembran, des Lamellipodiums. Unterhalb der Zellmembran polymerisieren die Aktinfilamente des Zytoskeletts und schieben die Vorderkante des Lamellipodiums in Bewegungsrichtung. Obwohl das Phänomen der Zellmigration Wissenschaftler seit Jahrzehnten fasziniert, sind viele Fragen noch immer unbeantwortet, wie zum Beispiel: Wie und weshalb bilden sich neue Lamellipodien? Wieso weisen manche Zelltypen stabile Lamellipodien auf, während das Lamellipodium anderer Zellen vorgeschoben und zurückgezogen wird, oder sich bildet und anschließend kollabiert? Wie verändert sich die Struktur des Lamellipodiums während der Phasen des Vorschiebens und Zurückziehens? Wird diese Dynamik durch Signalmoleküle gesteuert? Wie reagieren Zellen auf die Einwirkung äußerer Kräfte? Wie kann die Kraft-Geschwindigkeits-Kurve kriechender Zellen erklärt werden? Welche Strukturen bestimmen die mechanischen Eigenschaften des Lamellipodiums?

Mathematische Modellierung kann einen wichtigen Beitrag zu einem quantitativen Verständnis der Zellmigration liefern. In dieser Arbeit wird ein Modell entwickelt, das die Bildung, Stabilität und Stärke des Lamellipodiums, sowie die Dynamik der Zellvorderkante beschreibt. Dabei werden zwei Bereiche innerhalb des Lamellipodiums unterschieden. Im Hauptteil besteht das Lamellipodium aus einem dichten Netzwerk von Aktinfilamenten mit vielen Querverbindungen, dem sogenannten Aktingel. An der Vorderkante wachsen die Enden der Aktinfilamente durch Polymerisation und bilden einen dynamischen Grenzbereich, der semiflexible Region genannt wird. Die Kräfte, die die einzelnen Aktinfilamente in der semiflexiblen Region auf die Zellmembran an der Vorderkante ausüben, werden berechnet. Das Gleichgewicht zwischen den Filamentkräften und den viskosen sowie den äußeren Kräften bestimmt die Geschwindigkeit, mit der sich die Zellvorderkante bewegt. Das bereits publizierte Modell für die semiflexible Region wird in dieser Arbeit ergänzt. Eingefügt werden der retrograde Fluss im Aktingel und eine einfache Beschreibung einer variablen Filamentdichte aufgrund der Verzweigung und Kappung und Zertrennung vorhandener Filamente. Mit einigen Vereinfachungen wird das Modell für einen eindimensionalen Querschnitt durch das flache Lamellipodium durch ein System gewöhnlicher Differentialgleichungen dargestellt.

Mithilfe einer Stabilitätsanalyse des dynamischen Systems können drei qualitativ verschiedene Bereiche im Parameterraum identifiziert werden: (1) das Lamellipodium weist eine stationäre Filamentdichte und Bewegung der Vorderkante auf; (2) die Filamentdichte und Position der Zellvorderkante oszillieren; (3) die Filamentdichte fällt auf Null und die Zellvorderkante bewegt sich nicht. Dadurch werden Bedingungen für die Existenz stabiler Lamellipodien definiert und eine Beschreibung verschiedener Zelltypen wird ermöglicht. Im Bereich mit Filamentdichte Null kann kein stabiles Lamellipodium existieren, Lamellipodien können aber aufgrund von Anregbarkeit trotzdem vorrübergehend gebildet werden. Wenn man annimmt, dass sich einzelne kurze Filamente zufällig am Aktinkortex bilden, beschreibt das Modell im anregbaren Parameterbereich sehr gut das in Epithelzellen gemessene aufeinanderfolgende Vorschieben und Zurückziehen von Lamellipodien. Ideen zur

Beschreibung der Neubildung von Lamellipodien und der Formation bogenförmiger Aktinbündel im Lamellum werden durch die Ergebnisse bestätigt. Das Modell zeigt, dass prinzipiell keine Änderung in der Konzentration von Signalmolekülen innerhalb der Zelle notwendig ist, um die Zyklen von Vorschieben und Zurückziehen des Lamellipodiums zu beschreiben.

Das Modell wird auch auf die Kraft-Geschwindigkeits-Beziehung von Fischkeratozyten angewandt. Diese wird gemessen, indem eine Zelle auf einen flexiblen Cantilever zukriecht. Die Modellparameter werden durch Fits der Ergebnisse an den Geschwindigkeitsverlauf der gesamten Messung bestimmt. Dies führt zu experimentell bestätigten oder biologisch und physikalisch sinnvollen Parameterwerten. Aufgrund der guten Übereinstimmung zwischen Experiment und Simulationen wird ein Mechanismus vorgeschlagen, der die charakteristischen Merkmale der Kraft-Geschwindigkeits-Kurve erklärt. Außerdem können Eigenschaften des stabilen Lamellipodiums von Keratozyten, wie die Längen der Filamente und die Dichte der Verzweigungspunkte, abgeleitet werden. Es wird gezeigt, dass die mit dem Cantilever gemessene Kraft-Geschwindigkeits-Beziehung ein dynamisches Phänomen ist. Eine stationäre Kraft-Geschwindigkeits-Beziehung, die unter der Bedingung gilt, dass die Zellen einer konstanten Kraft ausgesetzt sind, wird vorhergesagt. Diese ist z. B. für Zellen im Gewebe entscheidend, die eine konstante Kraft durch ihre Nachbarzellen erfahren.

Contents

1 Introduction

The subject of this thesis is the movement of cells over surfaces. Many different cell types exhibit this crawling type of motion. In the developing embryo, undifferentiated cells move towards the site, where they form a certain tissue or organ. Immune cells like neutrophils squeeze through the walls of blood vessels and crawl towards the site of an infection. Skin cells start crawling when they have to close a wound (Bray [2001], Lodish et al. [2007]). During metastasis, cancer cells dissociate from the primary tumor, crawl towards blood vessels and spread all over the body (Yamaguchi et al. [2005], Condeelis and Pollard [2006]).

In vitro, cells are typically plated on a surface. They form a flat membrane protrusion in the direction of motion, the lamellipodium, which is usually only about 200 nm thick but several µm long (Small et al. [2002]). Cell migration is often described as a cycle of three subsequent steps (Ananthakrishnan and Ehrlicher [2007]). First, the leading edge of the cell protrudes. Second, the newly formed protrusion adheres to the substrate. Third, adhesion at the trailing edge is disrupted and the cell body with the nucleus is retracted. *In vivo*, such a movement on a two dimensional (2d) surface occurs for example when cells move along epithelial sheets like the walls of blood vessels. Cells can also move in 1d, for example along the fibers of the extracellular matrix (Doyle et al. [2009]). However, the most important case *in vivo* is certainly the movement in 3d through the extracellular matrix or a layer of other cells. Here, cells not only move by means of lamellipodia in the so called mesenchymal type of motion, but may also form blebs due to hydrostatic pressure in the amoeboid type of motion (Yamazaki et al. [2005]). Nevertheless, the insight gained in *in vitro* experiments and modeling of cell motility in 2d will also help to understand how cells move through tissues in 3d.

The major component of the cytoskeleton inside the lamellipodium is actin (see Fig. 1.1). This biopolymer forms longstranded filaments that preferentially polymerize at one end and depolymerize at the other end (Pollard and Borisy [2003], section 2.1 of this thesis). They can therefore generate motion. Inside the lamellipodium, they are aligned into the direction of movement, polymerize at the leading edge and depolymerize at the rear (see section 2.2). The actin filaments can exert a force on the leading edge membrane that leads to the protrusion of the lamellipodium. Further back, they stabilize each other by being cross-linked and entangled into a dense network (Medalia et al. [2002], Stricker et al. [2010]). Transmembrane proteins called integrins establish the connection between the actin network and the substrate and build adhesions (see section 2.3). Motor molecules called myosin are important for the retraction of the cell body. They can attach to actin filaments and walk along them in a certain direction (Lodish et al. [2007]). They can contract actin bundles connected by myosin, so called stress fibers.

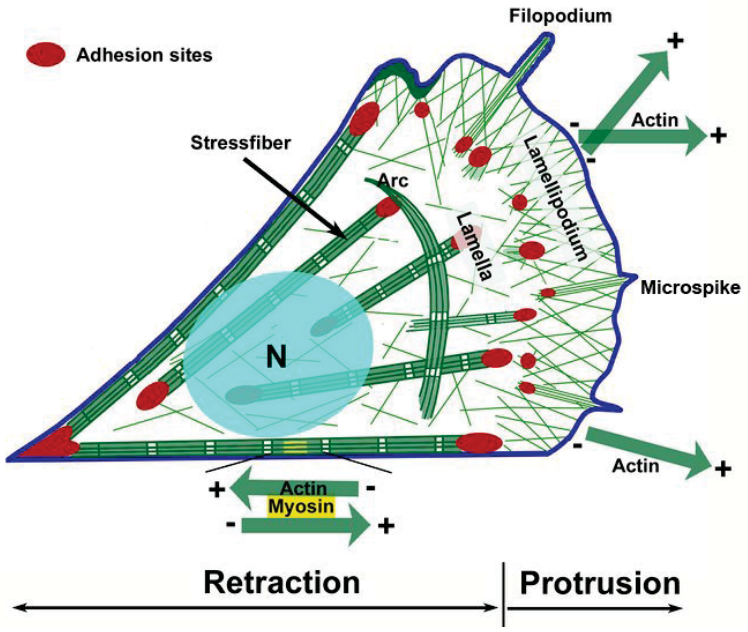

Figure 1.1: Schematic representation of the actin cytoskeleton in a migrating fibroblast. The polarized actin network in the lamellipodium polymerizes at the leading edge and pushes it forward. The cell attaches to the substrate at adhesion sites. Stress fibers cross-linked by myosin can contract and retract the cell body with the nucleus (N). Figure taken from the web page of the Vic Small lab of the Austrian Academy of Sciences in Salzburg and Vienna (IMBA) (http://cellix.imba.oeaw.ac.at/3-actin-cytoskeleton/).

A popular model system are fish keratocytes (Fig. 1.2 *A*). Those cells are with about 15 µm/min very fast. They have a broad lamellipodium, exhibit a persistent arc-like shape and move with a constant velocity. The lamellipodium of other cell types, like melanoma cells (Fig. 1.2 *C*), is dynamic and shows phases of protrusion and retraction. In some cell types, one even observes the regular spreading of waves along the leading edge of the lamellipodium (see also section 2.5). Often, the broad lamellipodial protrusion is overlaid by spiky finger-like protrusions called filopodia (Fig. 1.1, Fig. 1.2 *B*). In chapter 2 "Fundamentals of cell motility", the biological background will be further elucidated and some important experimental findings will be presented.

In this thesis, a mathematical model for the lamellipodium is developed. A detailed description is presented in chapter 3 "The model". Two regions in the lamellipodium are distinguished. The dense cross-linked actin network in the bulk is called the actin gel. In contrast to that, the newly polymerized tips of the filaments at the leading edge that are not cross-linked yet constitute a boundary layer called "semiflexible region" (SR). The two layers are maintained dynamically since filaments keep polymerizing at the front and afterwards cross-linkers keep attaching to the filaments. While we are aware that the transitions occurs gradually, we draw a defined boundary between actin gel and SR. It is defined by a critical density of cross-linkers bound to the actin filaments above

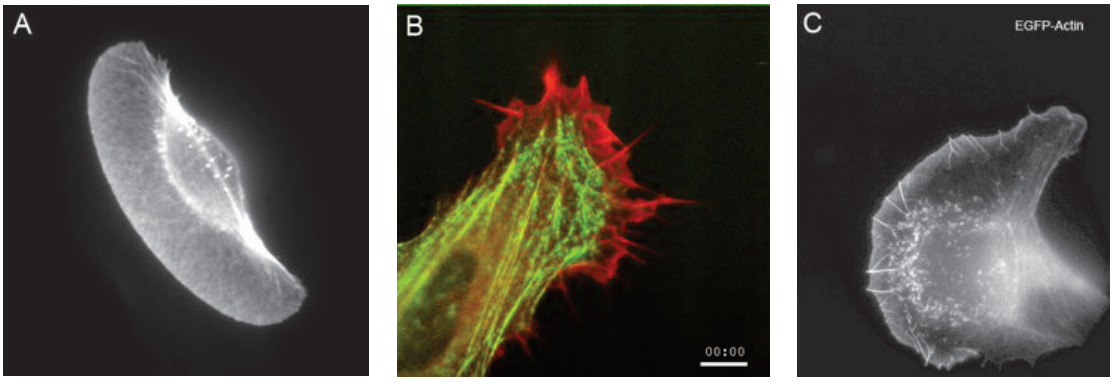

Figure 1.2: Different cell types moving over surfaces. (*A*) Fish keratocyte visualized by labeling actin with fluorescent phalloidin. (*B*) Fish fibroblast expressing mCherry-actin (red) and myosin light chain (green). Scale bar 10 µm. (*C*) B16 melanoma cell expressing GFP-actin. Pictures taken from the web page of the Vic Small lab of the Austrian Academy of Sciences in Salzburg and Vienna (IMBA) (http://cellix.imba.oeaw.ac.at/3-actin-cytoskeleton/). Corresponding videos can also be downloaded there.

which a gel-like behavior of the actin network is expected. The forces that the single actin filaments exert on the membrane are calculated. They are counteracted by viscous forces from surrounding and internal fluid, actin gel flow, gel flow past adhesion sites, membrane tension and external forces. The balance between filament and counteracting forces determines the velocity of the leading edge. The forces exerted by the filaments in the SR depend on the depth of that region and the length of the filaments. The tips of filaments can also attach to the leading edge. The attached filaments then either exert a pushing force when compressed, or a pulling force when stretched out. In section 3.1, expressions for the filament forces are given and the basic model for the SR, that has been published before (Gholami et al. [2008], Enculescu et al. [2008]), is introduced.

Following up, the existing model is improved. First, the backwards directed actin gel flow, called retrograde flow is calculated with the continuum theory of the active polar gel (Kruse et al. [2005, 2006]) in section 3.2. Retrograde flow can arise from insufficient adhesion to the substrate, so that polymerization is not completely turned into forward protrusion but the internal actin network is pushed backwards. It can also arise from contraction in the actin meshwork, for example due to myosin motor activity. We solve the gel equations in a quasistatic approximation and find an analytic expression for the retrograde flow as a function of the filament force exerted on the gel boundary and the gel cross-linking velocity, which we include into our filament model. It also depends on parameters like a friction coefficient of the gel to the substrate that represents adhesion, the viscosity of the actin gel and the active contractile stress in the gel.

Results of the model and fits of experimental data are presented in chapter 4 “Modeling results”. After including retrograde flow, we can model the measured force-velocity relation of keratocytes with a surprisingly good agreement between experiment and theory in section 4.2. To measure the force-velocity relation, a cell crawls towards the

cantilever of a scanning force microscope (SFM). When the leading edge of the cell touches the cantilever, its velocity first drops significantly, before it pushes forward again and deflects the cantilever. The force-velocity relation is the deflection velocity as a function of the deflection which is proportional to the force exerted on the leading edge. The deflection velocity first increases with increasing force before it drops to zero at the stall force. The concave shape of the force-velocity curve of the lamellipodium does not reflect the dependence of the polymerization rate of single filaments on force, which is convex. While the force-velocity relation has been measured already some years ago (Prass et al. [2006]), its characteristic shape in contrast to the expected result for single filaments remained not understood. Our model captures the velocity and retrograde flow velocity of the freely moving cell, the initial velocity drop upon cantilever contact and the following concave force-velocity relation. Due to the good agreement, we can not only suggest an explanation for the characteristic features of the force-velocity relation, but by fitting the detailed data we also obtain results for properties of the freely moving keratocyte. Especially, the free length of the actin filaments between the leading edge membrane and a grafting point has been a matter of debate recently (Pollard and Borisy [2003], Urban et al. [2010]) and our results favor long free filaments. We show that the force-velocity relation of keratocytes hitting an obstacle is a dynamic phenomenon. We also predict a stationary force-velocity relation that describes the behavior of cells if they experience a constant force, e.g. exerted by surrounding tissue (section 4.1.3).

As a second improvement to the model, nucleation of new and capping and severing of existing filaments is included in section 3.3. Hence the density of filaments in the SR can now vary whereas it has been a constant parameter before. Our model without capping and nucleation describes the free filament length and binding state dynamics of the filaments to the membrane in the SR. Because shortening of the filaments by cross-linking is compensated for by filament elongation due to polymerization, all attached and detached filaments quickly assume the same length. Based on a monodisperse approximation, we solve ordinary differential equations for the mean filament length. That monodisperse approximation cannot be applied to capped filaments since they do not polymerize and their length depends on the time point of capping. An exact solution requires a time dependent solution of the partial differential equation for the length distribution dynamics of capped filaments. That can be done analytically but only up to a remaining time integral, which renders the model very slow in simulations and rather inaccessible to analysis. Though analytical calculations have been addressed before (Faber et al. [2010]), we now introduce simplifications that make the problem feasible and computationally fast.

A stability analysis of the model is performed in section 4.1. It reveals that there are parameter regimes where the system exhibits oscillations of the leading edge, regimes with a stationary filament density, length and leading edge velocity, and parameter regimes where a filament density of zero and no leading edge movement is the only stable fixed point. This defines criteria for the existence of stable lamellipodia. In the regime with zero filament density, however, the system shows excitability and the density of filaments transiently increases before it drops to zero. Hence, a lamellipodium can transiently form. In section 4.3, it is shown that random nucleation of single filaments

from the cortex can lead to the periodic formation of lamellipodia as it has been observed experimentally (Burnette et al. [2011]). The model very well fits the measured data, showing that no change in cell signaling is necessary for subsequent protrusion and retraction of lamellipodia. The modeling results also support ideas on the initial formation of lamellipodia by nucleation of single filaments from the actin cortex, and the formation of actin filament arcs in the lamellum (see Fig. 1.1).

Different sets of parameters in the model correspond to different cell types or different levels of expression or activation of signaling molecules within one cell type. The parameters applying to keratocytes are determined by fitting the force-velocity relation. However, by changing parameters we can also describe other cell types. Our model offers an explanation why some cells, like keratocytes, exhibit stable lamellipodia whereas others, like epithelial cells, show protrusions and retractions while exploiting the same mechanism for lamellipodial protrusion. It is proposed which factors could induce a transition from a stable to a protruding and retracting and eventually collapsing lamellipodium and vice versa.

The model improves our understanding of several aspects of cell motility, for example during cancer metastasis. For efficient motion, the cells have to form lamellipodia which are stable and able to overcome membrane tension and external forces. The transient formation of lamellipodia by nucleation of single actin filaments from the cortex illustrates how lamellipodia initially form. The model predicts conditions for stable lamellipodia which determine whether a cell will move or not. The stationary force-velocity relation gives the velocity of a cell that experiences a constant force, for example a cell in a tumor surrounded by other cells. The dynamic force-velocity relation describes what happens if a cell that is already moving encounters an obstacle and how the actin cytoskeleton can adapt to the increasing external force. The model explains a large variety of biological observations and makes quantitative predictions. The detailed mathematical formulation provides a specific hypothesis on the set of underlying biological processes that is necessary and sufficient to explain the different experiments.

2 Fundamentals of cell motility

2.1 The cytoskeleton

2.1.1 Actin, microtubules and intermediate filaments

The cytoskeleton of most eukaryotic cells consists of actin, intermediate filaments and microtubules (Lodish et al. [2007]). Those biomolecules are all long-stranded filaments built up of monomers. They form a dense network, maintain the cell shape, and are responsible for interior and whole cell movements. Microtubules provide a "transport network", span throughout the cell, define the shape and stabilize certain structures. Intermediate filaments are located at the cell body around the nucleus, whereas actin is more present in the cell periphery and the cell cortex beneath the plasma membrane (Lodish et al. [2007]). The presence of actin filaments in lamellipodia and filopodia already shows that they play an important part in cell movement (Bray [2001]).

The different filaments of the cytoskeleton vary in diameter and stiffness. Actin filaments (F-actin) are two-stranded right-handed double helices twisting around themselves every 37 nm with a diameter of $7 - 9$ nm (Mogilner [2009]). Each globular actin monomer (G-actin) has a size of 5.4 nm (Mogilner [2009]). Intermediate filaments are about 10 nm thick. Microtubules are tubes with a diameter of about 25 nm formed from tubulin protofilaments (Lodish et al. [2007]).

Actin filaments and intermediate filaments are much more flexible than microtubules. The persistence length l_p can be taken as a measure for the stiffness of a polymer. It is the length above which the correlation between the tangent at one end and the other end is lost. At the persistence length, the bending energy of a polymer equals the thermal energy k_BT, $l_p = \kappa/k_BT$ with polymer's bending modulus κ. Actin has a persistence length of $3 - 17$ µm, intermediate filaments of $0.2 - 1.3$ µm (Wagner et al. [2007]) and microtubuli of $0.1 - 8$ mm (Van den Heuvel et al. [2008]). A polymer shows thermal fluctuations at lengths in the range of the persistence length.

2.1.2 Treadmilling

The cytoskeleton is highly dynamic. A driving mechanism that leads to the protrusion of the lamellipodium is the treadmilling of actin filaments. It means that the binding rate of actin monomers is higher at the one end of the filament than at the other. In a range of monomer concentrations in solution between the critical concentrations of both ends, the filament polymerizes at the plus (or barbed) end and depolymerizes at the minus (or pointed) end, thereby generating motion. More specifically, ATP-Actin binds

at the (+)-end, ATP is hydrolyzed to ADP-P_i-Actin, the phosphate unbinds and ADP-Actin dissociates from the (–)-end (Pollard and Borisy [2003]). Although we focus on the treadmilling of actin filaments here, a similar phenomenon is observed with microtubules.

The following reasoning shows, that filaments can treadmill when ATP-Actin monomers are hydrolyzed to ADP-Actin monomers within the filament. The critical concentration is the concentration of actin monomers in solution at which the filament switches from polymerization to depolymerization. Exactly at the critical concentration c_c, the binding of monomers to is balanced by the dissociation of monomers from the filament, hence the growth velocity of a filament end v_a is zero:

$$v_a = k_{on}c_c - k_{off} = 0 \quad \Longleftrightarrow \quad c_c = \frac{k_{off}}{k_{on}}. \tag{2.1}$$

Unlike the dissociation rate k_{off}, the binding rate $k_{on}c_c$ depends on the concentration of monomers in solution. The critical concentration is now the same at the (+)- and at the (–)-end, because the energy difference is the same for monomer loss from either end (Alberts et al. [1994]), but different for ATP- and ADP-Actin monomers:

$$c_c^{\mathrm{ATP}+} = c_c^{\mathrm{ATP}-} \neq c_c^{\mathrm{ADP}+} = c_c^{\mathrm{ADP}-}. \tag{2.2}$$

If there was no hydrolysis, hence no transition from ATP- to ADP-Actin, both ends would shrink or grow simultaneously. However, since the conformation of an actin monomer changes when it is incorporated into a filament, the binding and dissociation rates are much higher at the (+)-end than at the (–)-end. G-Actin monomers have a high affinity for ATP (Neuhaus et al. [1983]). Since ATP is usually abundant in a cell, we can assume that the concentration of ADP-actin monomers in the cytosol is very low compared to the concentration of ATP-actin monomers c^{ATP}. At a certain concentration, the (+)-end grows with the velocity

$$v_a^+ = k_{on}^{\mathrm{ATP}+}c^{\mathrm{ATP}} - k_{off}^{\mathrm{ATP}+} = k_{on}^{\mathrm{ATP}+}\left(c^{\mathrm{ATP}} - c_c^{\mathrm{ATP}}\right), \tag{2.3}$$

which is always positive, if the concentration of G-ATP-Actin is above the critical concentration. We have neglected hydrolysis since it is slow compared to the binding and unbinding of monomers at the (+)-end. Due to the binding of ATP-actin, an "ATP-cap" forms at the (+)-end. At the (–)-end, the rates are much lower and hydrolysis cannot be neglected. The growth velocity reads here

$$v_a^- = k_{on}^{\mathrm{ATP}-}c^{\mathrm{ATP}} - p_0k_{off}^{\mathrm{ATP}-} - (1-p_0)k_{off}^{\mathrm{ADP}-} = k_{on}^{\mathrm{ATP}-}\left(c^{\mathrm{ATP}} - p_0c_c^{\mathrm{ATP}}\right) - (1-p_0)k_{off}^{\mathrm{ADP}-}, \tag{2.4}$$

with the probability p_0 that ATP has not been hydrolyzed yet. On long time scales, every ATP-actin will become an ADP-Actin, therefore we set $p_0 = 0$. The growth velocity at the (–)-end simplifies to

$$v_a^- = k_{on}^{\mathrm{ATP}-}c^{\mathrm{ATP}} - k_{off}^{\mathrm{ADP}-}. \tag{2.5}$$

We now see that v_a^- can also get negative. For a concentration in the range $c_c^{\mathrm{ATP}} <$

$c^{\mathrm{ATP}} < k_{off}^{\mathrm{ADP}-}/k_{on}^{\mathrm{ATP}+}$, we are in a treadmilling situation where the (+)-end grows and the (–)-end shrinks.

In the experiment, one can of course not strictly distinguish critical concentrations for ADP- and ATP-actin. A filament will bind and loose ADP- and ATP-actin at both ends. We have also completely ignored the intermediate ADP-P_i state. Since the binding affinity of a monomer type may depend on the neighboring monomer in the filament, there are also more than four rates. The "effective critical concentration" denotes the G-Actin concentration at which a filament end switches from depolymerization to polymerization, regardless of the monomer state. It is lower at the (+)-end than at the (–)-end. If the number of actin monomers is limited, the G-actin concentration will reach a value between the two critical concentrations and the filaments treadmill.

2.1.3 Motor molecules, cross-linkers and actin structures

There are motor molecules associated with the cytoskeletal actin filaments and microtubules. Those proteins are ATPases and can transform chemical into mechanical energy (Lodish et al. [2007]). Thus, they can walk along the filaments in a certain direction and transport a cargo. Myosin, a motor protein associated with actin filaments, contains a head, neck and tail domain. The head domain changes its conformation upon ATP hydrolysis and P_i release. Since it is bound to the filament during the "power stroke" and unbinds afterwards, it moves with respect to the filament. Myosin II, a motor found in skeletal muscle, assembles into thick polar filaments (Lodish et al. [2007]). The myosin filaments bind to actin filaments and cross-link them into bundles with filaments aligned into opposite directions. In motile cells, those bundles of actin filaments are called stress fibers because myosin can contract them.

The actin filaments in the cytoskeleton are cross-linked. One cross-linker is myosin, another example is α-actinin. Specific types of cross-linkers are associated with different actin structures. α-Actinin connects actin filaments in parallel bundles found in finger-like filopodial protrusions, whereas filamin assembles filaments into meshworks found in lamellipodia (Lodish et al. [2007]). Fascin cross-links actin filaments in unipolar bundles, similar to α-actinin, but it not only induces the formation of microspikes in epithelial cells but also enhances lamellipodium formation and cellular motility (Yamashiro et al. [1998]). The Arp2/3 complex, mediating actin branching in dendritic networks at the leading edge, is also an important cross-linker (see next section). Cross-linkers stabilize the actin network. Since they dynamically attach and detach, they give the cytoskeleton viscoelastic properties. On short time scales, the cross-linked actin network behaves like an elastic body. On long time scales, the cross-linkers can rearrange and the network behaves like a viscous fluid. Therefore, we also call the cross-linked network actin gel (Mahaffy et al. [2000], Kruse et al. [2006]).

Sometimes, two regions are further distinguished in the flat and broad protrusions of motile cells: the lamellipodium and the lamellum (Gardel et al. [2010], see also Fig. 1.1). In this context, the lamellipodium spans the first $1-3$ µm depth behind the leading edge and contains a dendritic actin network. It is thought to be the "protrusive unit" of the cell. Filaments were suggested to assemble at the leading edge and disassemble

within the lamellipodium (Ponti et al. [2004]). Behind the lamellipodium extends the lamellum which contains actin arcs, bundles or stress fibers. It is the "contractile unit". The existence and location of two independent actin structures is still a matter of debate (Danuser [2009]). The actin gel and semiflexible region distinguished in the mathematical model are not the same as lamellum and lamellipodium. The gel boundary is thought to be located within the lamellipodium. Hence, the whole protrusion will be referred to as lamellipodium, unless a concrete distinction is made.

2.2 The dendritic nucleation model

2.2.1 Regulation of treadmilling in vivo

The treadmilling rate *in vivo* is up to tenfold higher than with pure actin *in vitro* (Lodish et al. [2007]). There are several proteins that regulate treadmilling in the lamellipodium.

The critical step in actin filament formation is nucleation, i.e. the assembly of three monomers as a seed for filament polymerization (Sept and McCammon [2001]). Different actin nucleators support the de novo formation of filaments. Formins nucleate single filaments. They posses two adjacent FH2 domains that can bind two actin monomers which form the core for the two strands of the actin filament. The formin can now alternately detach from one of the monomers and add a new monomer to the corresponding filament strand while it remains bound to the other strand, thereby elongating the (+)-end of the filament. Formins are activated by membrane-bound Rho-GTP (Lodish et al. [2007]). Another actin nucleator is the actin related protein complex Arp2/3. Arp2/3 binds to existing actin filaments and nucleates a new branch under a 70° angle upon activation by binding of Wiskott-Aldrich syndrome protein (WASp). WASp changes the conformation of the protein complex in such a way that Arp2 and Arp3 resemble the (+)-end of an actin filament from which the new filament can grow. When GTP binds to the membrane associated small GTPase Cdc42, it can activate WASp (Lodish et al. [2007]).

The polymerization of actin filaments is terminated by capping. Proteins like capZ and gelsolin bind to the filaments' (+)-ends and prevent them from further growing. It was speculated that capping restricts actin polymerization to a region close to the leading edge membrane. Furthermore, it gives rise to faster polymerization because the number of (+)-ends is limited, which leads to a higher concentration of monomers in the cytosol. In order to free actin monomers, actin depolymerization is enhanced *in vivo*. Actin depolymerization factor (ADF) or cofilin binds to two adjacent ADP-actin-monomers in a filament and weakens the bond between them. Consequently the filament breaks more easily. If caged cofilin is photoreleased locally, it induces the formation of a protrusion (Ghosh et al. [2004]), presumably because a high number of (+)-ends is generated. However, cofilin binds to actin filaments collectively and therefore first of all stimulates their disassembly. At very high concentrations, cofilin can also stimulate

nucleation (Andrianantoandro and Pollard [2006]). Profilin is a protein that binds to actin monomers and leads to the release of ADP. ADP is replaced by ATP which is abundant in the cell. Therefore, profilin maintains a pool of monomeric ATP-actin in the cell.

The insight in the function of those different proteins and electron microscopy images of the actin network in the lamellipodium have lead to a picture for the processes at the leading edge that drive protrusion. It is termed the "dendritic nucleation model" (Pollard et al. [2000], Pollard and Borisy [2003], see Fig. 2.1). Membrane bound WASp activates the Arp2/3 complex which nucleates new filament branches that grow into a dendritic actin network. The polymerizing actin filaments push the membrane forward. Capping proteins terminate barbed end growth. Monomers are recycled by depolymerization at the rear, severing of filaments by cofilin and exchange of ADP for ATP by profilin. They diffuse to the front and are again available for nucleation and polymerization.

It was assumed that the actin filaments have to be relatively short and stiff (about $50 - 200$ nm) to push the membrane effectively (Mogilner and Oster [1996], Pollard and Borisy [2003]). Recent electron tomograms however showed, that filaments are considerably longer, about 1 µm (Urban et al. [2010]). The tomograms revealed that most of what had been interpreted as branches are actually just filaments crossing. Filaments are also oriented under a variety of angles and not only $\pm 35°$ (Koestler et al. [2008]). Those findings do not question the "dendritic nucleation model" but suggest that the branching frequency is much lower than previously assumed (Vinzenz et al. [2012]). It was also speculated that besides Arp2/3 formins play a role as nucleators at the leading edge (Urban et al. [2010]).

2.2.2 Intracellular pathogens and reconstituted systems

Some bacteria and viruses exploit the same mechanism, that drives protrusion of the leading edge, to propel themselves forward inside an infected cell. The bacterium *Listeria monocytogenes* has a protein called ActA on its surface that can bind and activate the Arp2/3 complex. Consequently polymerizing actin assembles around the bacterium and will eventually form a comet tail that pushes the bacterium forward. ActA can also bind vasodilator-stimulated phosphoprotein (VASP), a protein that has binding sites for both profilin-ATP-actin monomers and actin filaments. It therefore establishes a connection between bacterial surface and actin filaments while recruiting actin monomers (Lodish et al. [2007]).

In vitro, *Listeria* and *Shigella*, another bacterium, will form comet tails and move in a medium containing just five proteins (actin, Arp2/3, N-WASp, ADF/cofilin and capping protein), a so called minimum motility medium. The movement becomes more effective if profilin, α-actinin and VASP are added as well. The motility rate of the bacteria shows a maximum as a function of the concentration of Arp2/3, capping protein, ADF, VASP and profilin (Loisel et al. [1999]). The same type of motion can *in vitro* even be reconstituted with N-WASp coated polystyrene beads (Wiesner et al. [2003], Bernheim-Groswasser et al. [2005]) or oil droplets (Trichet et al. [2007]). Those objects show continuous or saltatory "hopping" motion, depending on parameters like bead size,

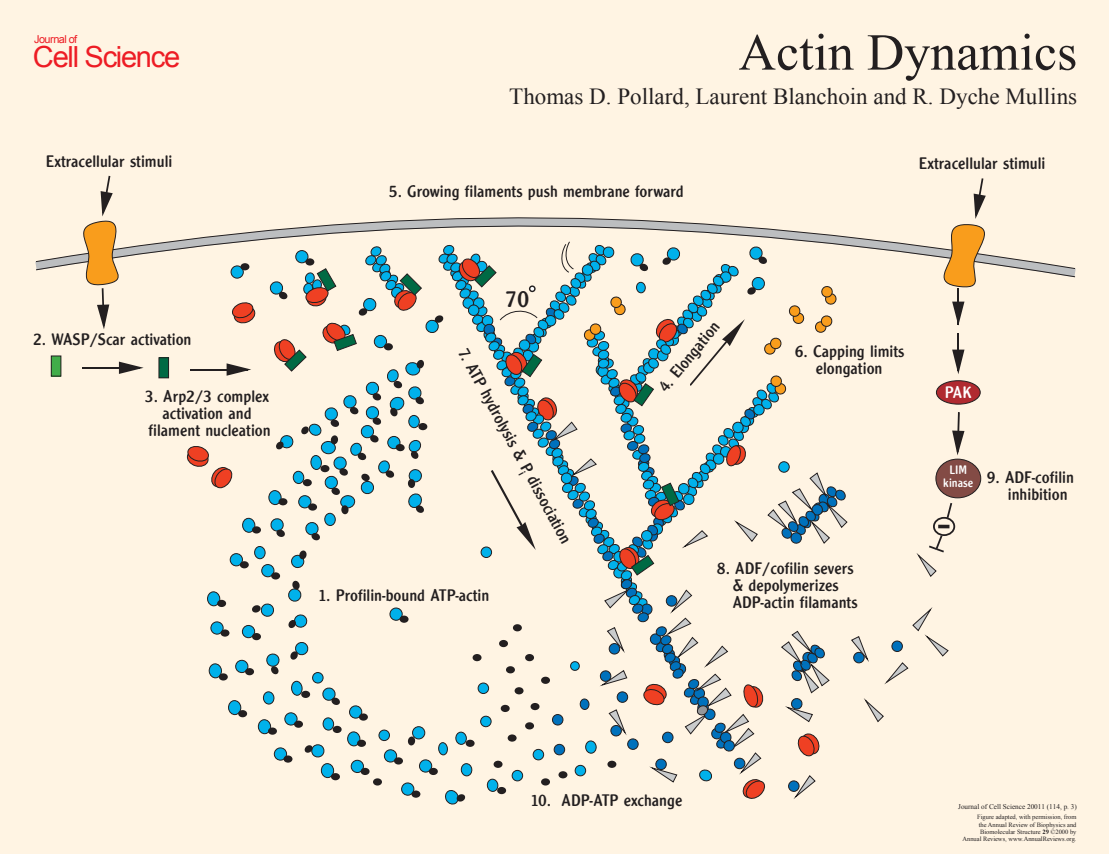

Figure 2.1: A dendritic actin network in the lamellipodium pushes the leading edge plasma membrane forward and leads to protrusion. Treadmilling of actin filaments *in vivo* is regulated and enhanced by several proteins (see text for details). This figure is taken from Pollard et al. [2001].

coating density or protein concentration.

Also some viruses use the "actin machinery" to move, like the cell-associated extracellular form of *Vaccinia virus* propelling itself into neighboring cells (Rottner and Stradal [2009]). However, because viruses are very small particles, the number of actin filaments in their tail is much lower than in the tails of bacteria.

2.3 Retrograde flow and adhesions

Not all actin polymerization at the leading edge is converted into forward protrusion. Since there are viscous forces counteracting membrane motion and the membrane is under tension, there has to be a friction force between the actin network and the substrate to push the membrane forward effectively. If the friction is not strong enough, the actin network in the lamellipodium is pushed backwards. The movement of actin opposite to the direction of protrusion is called retrograde flow. Retrograde flow is also generated by myosin motors that contract the actin network and pull the actin at the leading edge backwards. Contraction may arise from depolymerization, too (Zajac et al. [2008]).

Adhesions are the "points of friction" between the actin network and the substrate. A major component of adhesions are integrins, heterodimeric transmembrane receptors comprising an α- and a β-subunit that can bind to extracellular ligands. Integrins can be in an active state with high affinity or in an inactive low-affinity state (Vicente-Manzanares et al. [2009]). Several molecules build the linkage between integrins and the actin cytoskeleton, e.g. α-actinin, vinculin, talin, paxilin and focal adhesion kinase (FAK). Talin activates integrins and subsequently paxilin is recruited to integrin clusters. The strength of the linkage might depend on its actual composition that can vary. α-Actinin is always tightly attached to the actin filaments, in contrast to the other components that may unbind and favor "slippage". Therefore adhesions can be viewed as a molecular "clutch" that is engaged when actin is connected to the substrate via integrins, and disengaged when one of the several involved bonds breaks (Vicente-Manzanares et al. [2009]). The intracellular interface between integrins and actin is the "weak link" in adhesion complexes (Selhuber-Unkel et al. [2010]).

Adhesions exist at different stages in the cell. Close to the leading edge, small clusters of integrins form nascent adhesions that assemble with protrusion and partly disassemble within minutes. Some of the nascent adhesions however grow larger and mature into more stable focal complexes and focal adhesions (Gardel et al. [2010]). Focal adhesions are located at the more proximal part of protrusions, the lamellum, and the cell body, and are connected to stress fibers. Accordingly, mechanical stress stimulates the maturation of adhesions. On a molecular level, this is possibly due to a change in protein conformation unmasking binding sites (Nicolas et al. [2004], Gardel et al. [2010]). Also, the lifetime of the bond between integrins and extracellular ligand increases if a force is applied. This phenomenon is called catch bond behavior (Gardel et al. [2010]). Stress fibers of the lamellum can also assemble and polymerize at focal adhesions.

Adhesions are "mechanosensors". This term is sometimes used in two different contexts. On the one hand, adhesion strength increases when a force acts on them (see above). On the other hand, the adhesion strength increases with increasing mechanical stiffness and density of the extracellular matrix (Gardel et al. [2010]). The two phenomena are correlated since a soft substrate is compliant and only week forces can be exerted on adhesions. However, it is also possible that adhesion strength increases because more integrin binding sites are available in a stiff substrate (Cavalcanti-Adam et al. [2007]). It has been shown, that there is an optimal adhesion level for the cell migration rate (Palecek et al. [1997]). At low adhesion levels, the retrograde flow will be high and prevent protrusion. However, for the cell body to be pulled forward, adhesions have to be turned over and disassemble at the rear. This is impaired if adhesion is too strong. Adhesions are assumed to be stronger at the leading edge of the cell than at the trailing edge, a phenomenon known as graded adhesion, to allow more effective protrusion of the front and retraction of the rear (Mogilner [2009]).

2.4 Small GTPases signaling

In vivo, cells will move in response to external signals. For example white blood cells, like neutrophils, will "sense" molecules secreted by bacteria and move towards the site of an infection. Fibroblasts, cells of the skin, move towards a wound site during healing. The process of cells moving in response to an external gradient of a chemical, often a growth factor, is called chemotaxis (Lodish et al. [2007]). Growth factors bind to membrane receptors and stimulate signaling cascades that lead to a polarization of the cytoskeleton, directed polymerization, formation of stress fibers and adhesion sites, and other processes necessary for cell movement. Not all motile cells are chemotactic. Some cells, like keratocytes, polarize and move spontaneously or react to a force that pushes them into a certain direction. Also without external cues, the polarity of the cytoskeleton is maintained once established. The same holds for fragments of keratocytes that continue to move after mechanical stimulation (Verkhovsky et al. [1999]). It is not entirely clear how the cell maintains its polarity. The formation of a lamellipodium at the front must lead to the suppression of other lamellipodia around the cell and at the rear. However, it is very likely that internal cell signaling plays a major role in those processes, too.

Key players in the signaling pathways leading to cell motility are the the small guanosine trisphosphate binding proteins (GTPases) of the Rho family, namely Cdc42, Rac and Rho. They can be in an inactive state when they have GDP bound and in an active state with GTP bound. Guanine nucleotide exchange factors (GEFs) can catalyze the exchange of GDP for GTP and switch them from the inactive to the active state, whereas GTP is hydrolyzed by GTPase-activating proteins (GAPs) which switches Rho-proteins "off" to the inactive form. In the cytosol, they remain in the inactive state since they are bound to a guanine nucleotide displacement inhibitor (GDI). Membrane bound GEFs

are activated by growth factors. They promote the release of the GDI and switch the Rho proteins on at the membrane (Lodish et al. [2007]).

If a GTPase is "locked" in the active form, it is said to be constitutively active. A cell that expresses the constitutively active protein is called a dominant active mutant. The dominant negative mutant expresses a GTPase that is always inactive. Some bacteria secret chemicals that interfere with the small GTPases signaling pathways and render Rho proteins constitutively active or inactive and therefore e.g. prevent being engulfed by immune cells (Burridge and Wennerberg [2004]).

Upstream of Rho activation, lysophosphatidic acid (LPA) binds to membrane receptors and activates RhoGEFs via G proteins (Burridge and Wennerberg [2004]). If dominant active Rho is overexpressed in a cell, the formation of stress fibers and adhesion sites is elevated. One of the downstream effectors of Rho is Rho kinase (ROCK). Its activation leads to increased myosin activity and an inhibition of cofilin. Another target of Rho is the formin mDia. Consistently with its role in stress fiber formation and contraction, activated Rho is rather found at the cell body and the rear of a cell (Lodish et al. [2007]). However, recently it was shown that Rho is also activated at the leading edge synchronous with edge advancement and might be important for protrusion formation (Machacek et al. [2009]).

Rac can be activated by growth factors that bind to membrane receptors and stimulate the activation of the Phosphoinosite 3-kinase (PI3K). Expression of constitutively active Rac favors the formation of lamellipodia and membrane ruffles. One important function of Rac is the activation of the WAVE complex which subsequently activates Arp2/3. An additional downstream effector of Rac is the p21-activated kinase (PAK). It stimulates the actin cross-linker filamin. PAK activation can also lead to the inhibition of cofilin and myosin activity (Burridge and Wennerberg [2004]). Active Rac is predominantly found at the leading edge, in lamellipodia and membrane ruffles.

The dominant active mutant of Cdc42 shows a high number of filopodia. The primary effector of Cdc42 is WASp that activates Arp2/3, though this is presumably not the reason for enhanced filopodia formation (Ridley et al. [2003]). Cdc42 is essential for chemotaxis and said to be a "master regulator of cell polarity" (Ridley et al. [2003]). It is active at the cell front.

Small GTPases are not only activated through growth factors that bind to membrane receptors. There are crosstalks between the different Rho proteins. Cdc42 activates Rac (Machacek et al. [2009]). Rac can activate or, under different conditions, also inactivate Rho (Burridge and Wennerberg [2004]). Vice versa, Rho inactivates Rac. This negative feedback loop might be important for maintaining cell polarity. Adhesions influence small GTPase activity, too. Paxilin, a protein of the linkage between integrins and actin, contains several domains that can activate Rac. However, when stress is applied to adhesions, integrin initiated signaling can also lead to the activation of Rho. Since Rho activates myosin and enhances stress fiber formation, which in turn promote adhesion clustering, there is a positive feedback favoring stable adhesion formation (Vicente-Manzanares et al. [2009], Gardel et al. [2010]).

2.5 Dynamic regimes of lamellipodium motion

Different cell types can have very distinct shapes and exhibit different "modes" of motion. Fish keratocytes have a crescent shape with a broad lamellipodium and migrate fast and uniformly. In contrast to that, the social amoeba *Dictyostelium discoideum* protrudes and retracts pseudopodia in all directions, apparently testing its environment, and moves in a more random fashion towards a chemoattractant. Keratocytes with less regular and smooth-edged morphologies also show less persistent motion (Lacayo et al. [2007]). When cells are plated on a surface, they develop lamellipodia and spread, some assume a pancake-like shape. Some, but not all spread cells, will eventually start moving, spontaneously or in response to mechanical or chemical cues.

Distinct cycles of protrusion and retraction have been observed at the edge of spreading and motile cells (reviewed in Ryan et al. [2012], Enculescu and Falcke [2012]). A variety of spreading cells exhibit lateral waves traveling around their circumference (Doebereiner et al. [2006]). Machacek and Danuser [2006] find other characteristic "morphodynamic patterns" in motile cells, like synchronized retraction and protrusion ("I-state"), or random bulges splitting and traveling along the leading edge of a lamellipodium laterally in different directions ("V-state"). Those patterns vary from cell type to cell type, but can also change upon Rac1 activation in epithelial cells. Patterns are not restricted to the edge of existing lamellipodia, but the whole lamellipodium can be dynamic, too. Upon PAK3 depletion, a whole lamellipodium has been observed to travel around a circular *Drosophila* cell (Asano et al. [2009]). Burnette et al. [2011] monitor the structure of the actin network in epithelial cells during subsequent cycles of protrusion and retraction and show that the lamellipodium evolves into the lamellum during retraction. Similar observations have been made with melanoma cells (Koestler et al. [2008]). A yet different phenomenon are waves of high F-actin density traveling along the ventral membrane attached to the substrate that lead to the formation of a protrusion when impinging on the cell perimeter (Bretschneider et al. [2004, 2009]). Cycles of protrusion and retraction are thought to help the cell exploring the chemical and mechanical properties of its environment.

Pathogens and reconstituted systems show distinct regimes of motion, too. They can move with a constant velocity or "hop" forward with a periodically increasing velocity (Rafelski and Theriot [2005], Trichet et al. [2007]). Beads exhibit a transition from continuous to saltatory motion with increasing bead size and coating density (Bernheim-Groswasser et al. [2005]).

2.6 The force-velocity relation

The forces that can be exerted by growing actin networks and lamellipodia have been measured quantitatively. The force-velocity relation is generally the velocity of a motile system as a function of an applied force.

The force-velocity relation was first measured for Listeria (McGrath et al. [2003]) and beads (Wiesner et al. [2003]) by increasing the viscosity of the surrounding fluid with seemingly contradictory results. Listeria experiments result in a convex force-velocity relation whereas the velocity of beads is load-independent. Marcy et al. [2004] attached a bead to a flexible microneedle and covered it with N-WASp. The actin comet tail growing behind the bead in a minimum motility medium was held with a micropipette. By applying a feedback loop, a constant pushing or pulling force, proportional to the deflection of the microneedle, was exerted and the growth velocity of the comet tail was measured. The resulting force-velocity curve decreases linearly for negative (pulling) forces and decays more slowly for increasing pushing forces. Thus it is convex, similar to the Listeria measurements, but the range of applied forces is much broader and the decrease in velocity at positive forces weaker.

The force-velocity relation of an actin network growing under an atomic force microscope (AFM)-cantilever coated with ActA was measured, too (Parekh et al. [2005]). First the velocity stays constant with increasing force, before it drops and motion stalls at a force of 150 ± 120 nN, depending on coating density and area. The force-velocity curve has a concave shape. Surprisingly, when the cantilever is retracted during the load-independent phase and the force is decreased, the velocity stabilizes at a higher value than before. Thus, hysteresis in the force-velocity relation is observed.

Mogilner and Oster [1996] calculated the force-velocity relation of a single filament, i.e. the barbed end growth velocity V as a function of an applied force f, as

$$V = V_{max} \exp(-fl/k_BT) - V_{dep}, \tag{2.6}$$

with the free polymerization velocity V_{max}, the depolymerization velocity V_{dep}, the length increment added by one monomer l and the thermal energy k_BT. The measurements with Listeria by McGrath et al. [2003] and with beads by Marcy et al. [2004] are in agreement with this prediction and can be interpreted to reflect the relation of the single filaments. The weaker decay in velocity could arise from a higher filament density (Mogilner and Oster [2003]). It was argued that filament networks behave differently because the density of filaments increases with increasing load (Parekh et al. [2005]). Therefore, the load per filament, and consequently also the obstacle velocity, remains constant as the force increases. That could also explain the hysteresis. The autocatalytic branching model (Carlsson [2003]), which assumes nucleation of new filaments from existing filaments, indeed exhibits a constant force-velocity relation and provides an explanation for the bead measurements by Wiesner et al. [2003], too.

Prass et al. [2006], Heinemann et al. [2011] were the first to measure the force-velocity relation of whole cells, namely keratocytes. They used an AFM cantilever and placed it into the cell's migrating path. When the cell hits the cantilever, it deflects the cantilever and the force exerted on the cell's leading edge increases. The force is proportional to the deflection. By differentiating the deflection time-course, one can calculate the force-velocity relation. Similar to the relation for actin networks, the observed curve is concave, with a load-independent velocity at lower forces and decreasing velocity at higher forces up to the stall force.

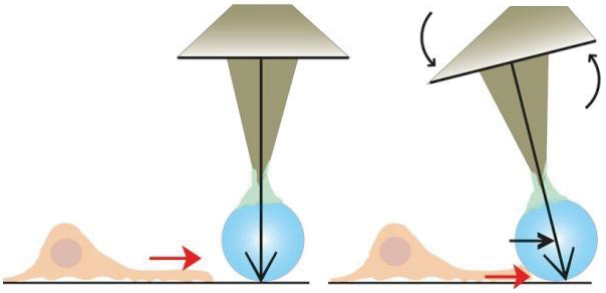

Figure 2.2: Spherical probe attached to an SFM-cantilever to measure the force-velocity relation of a keratocyte. The probe is placed with a preset force of 10 nN in the path of a forward moving cell and stalls the leading edge. The torsional bending of the cantilever measures the force. Figure published in Zimmermann et al. [2012].

Similar measurements with keratocytes were performed by Brunner et al. [2006, 2009] (see Fig. 2.2). Here, a polystyrene bead is attached to the tip of a scanning force microscopy (SFM)-cantilever and positioned on the substrate in front of a migrating cell with a preset force to assure tight contact. Cells move unhindered until they encounter the bead, push it, and cause torsion of the cantilever that corresponds to a lateral force (Zimmermann et al. [2012]). If the vertical preset force is chosen low, the cell is able to squeeze beyond the bead and to push the cantilever upwards (Brunner et al. [2006]). Thereby, the height of the lamellipodium can be measured and the torsion measured on top corresponds to retrograde forces. Finally, the cell body forces can be evaluated also. High-resolution interference reflection microscopy measures the free cell velocity and monitors precisely the position of the lamellipodial edge with respect to the spherical probe. In addition, lamellipodium feature tracking analysis is used to measure the retrograde flow in some cells during unhindered motion. Thus, a complete map of forces and velocities associated with cell motility is obtained. We use our model to fit and explain the leading edge stall force measurements (see section 4.2 and Zimmermann et al. [2012]).

We have to note that there are crucial differences between the force-velocity relation of actin networks and keratocytes, although they both have a concave shape. First of all, keratocytes are fast cells that move with about 15 µm/min. However, when a cell touches the SFM cantilever, the visual impression is that it stops the leading edge motion instantaneously, like a rigid wall, whereas the cell body keeps moving. The deflection velocity measured with the cantilever is indeed two or three orders of magnitude lower than the velocity of the freely moving cell. That already a weak force of a few piconewtons can stall leading edge motion has also been demonstrated by placing keratocytes into a fluid flow from a pipette (Bohnet et al. [2006]). Secondly, the maximum deflection of the cantilever, that corresponds to the stall force, is reached within $5 - 20$ s during measurements with keratocytes, whereas it takes up to 200 min for actin networks. It is unlikely that in keratocytes the number of filaments changes significantly due to nucleation within such a short time. Accordingly, no hysteresis has been observed in keratocytes (Heinemann et al. [2011]). When the cantilever is retracted after a measurement, the result of the following measurement is the same. Third, the stall force of keratocytes is approximately 1 nN in contrast to the 150 nN

of actin networks. Finally, our simulations revealed that there is an adaptation phase to the stalled state after the first deflection maximum (Zimmermann et al. [2012] and section 4.2), indicating that the cell state at the stall force does not correspond to a stationary state of the lamellipodium dynamics.

2.7 Quantitative models of actin-based motility

Actin-based motility has been subject to extensive mathematical modeling in the past, thus only a few of the models can be mentioned here (see also Mogilner [2009] and Enculescu and Falcke [2012] for reviews). One of the first mathematical models for actin-based motility was the "Brownian Ratchet Model" (Peskin et al. [1993]). It was shown that actin polymerization can produce a force on an obstacle. Actin filaments are oriented with their barbed ends towards the obstacle. Due to Brownian motion of the obstacle, from time to time, a sufficiently large gap between filament tip and obstacle occurs, so that an actin monomer can attach to the filament. Since the probability for instantaneous detachment is low, the obstacle cannot fluctuate backwards again and a net forward protrusion is achieved. Later, it was shown that Brownian motion of the obstacle alone is not sufficient for motion under biological conditions. In particular, the dependence of the velocity on the diffusion coefficient of the obstacle predicted by this model could not be verified. Consequently, bending of filaments was considered also, leading to the "Elastic Brownian Ratchet Model" (Mogilner and Oster [1996]). Finally, in the "Tethered Ratchet Model" (Mogilner and Oster [2003]), transient attachment of the filaments to the obstacle was taken into account, with the important conclusion that forward motion is possible despite attached filaments exerting a pulling force on the obstacle.

Generally, one can distinguish "filament models", like the ratchet models, that start from the properties of single actin filaments, and "continuum" or "gel models", that describe the actin network via constitutive equations and material constants (Enculescu and Falcke [2012]). Often, the different models concentrate on different aspects of actin-based motility and aim at explaining different experimental findings including:

1. *The velocity of the leading edge or another obstacle like Listeria or a bead* is a basic feature that is reproduced by most of the published models. Groundbreaking was the work by Peskin et al. [1993], Mogilner and Oster [1996, 2003].

2. *Symmetry breaking and comet tail formation in Listeria or beads* was e.g. treated by the gel model by John et al. [2008].

3. *The different regimes of Listeria / bead / oil droplet motion (stationary and saltatory).* Gerbal et al. [2000] provide an explanation for oscillatory motion of *Listeria* with their gel model. Stress is thought to increase with gel growth and relax periodically. A similar mechanism - force on the bacterium or bead increases while

the tail is attached to it until the connection is disrupted abruptly and the bacterium jumps forward - can also account for oscillations in the filament model by Gholami et al. [2008]. Enculescu and Falcke [2011] showed that the same model also reproduces transitions between the states of motion with bead size.

4. *The bell-shaped dependence of the velocity on protein concentrations.* The velocity dependence on Arp2/3 concentration and capping rate is nonmonotonic in the explicit simulations of Lee and Liu [2008].

5. *The structure of the actin network.* Continuum models can be used to calculate concentration profiles, e.g. of F-actin (Alt et al. [2009]). However, filament models can naturally make stronger predictions in this field. Explicit modeling of actin filament networks helped to elucidate their structure (e.g. Carlsson [2001, 2004], Atilgan et al. [2005]). In accord with the dendritic nucleation model, filaments arranged at angles of $\pm 35°$ in the simulations by Schaus et al. [2007]. Weichsel and Schwarz [2010] showed that a stable $+70/0/-70°$ orientation pattern exists besides the $\pm 35°$ pattern. With the model presented in this thesis, we could show that filaments at the leading edge might be longer and have less branch points than previously assumed (Zimmermann et al. [2012]).

6. *The formation of two distinct actin structures in cell protrusions, often referred to as lamellipodium and lamellum,* was treated by Shemesh et al. [2009]. However, their gel model concentrates on adhesion maturation and does not cover e.g. actin bundle formation explicitly. Gradients in filament length and distinct regions of polymerization and depolymerization activity where found by Huber et al. [2008] and Ditlev et al. [2009] using kinetic modeling.

7. *The formation and maturation of adhesions, dependence of adhesion strength on force*, can be nearly seen as a modeling field on its own, see Bershadsky et al. [2006] for a review and e.g. Dembo et al. [1988], Stéphanou et al. [2008].

8. *The bell-shaped dependence of the cell velocity on adhesion strength* was first predicted by DiMilla et al. [1991] and e.g. reproduced with a continuum model by Gracheva and Othmer [2004].

9. *Mechanotaxis / Durotaxis (that is, the velocity of a cell and the area of spreading cells increases with increasing stiffness of the substrate)* is closely related to the force-dependent strengthening of adhesions, as demonstrated by Krzyszczyk and Wolgemuth [2011]. Dokukina and Gracheva [2010] can reproduce the experimental findings by calculating the force balance at several nodes interconnected by elastic springs and viscous dashpots. A continuum theory is used by Zemel et al. [2010a] to predict the spreading area of cells.

10. *Chemotaxis*, see e.g. Iglesias and Devreotes [2008], Jilkine and Edelstein-Keshet [2011] for reviews. An important concept was the "LEGI" model ("local excitation global inhibition") providing a possible explanation of how cells can sense very

shallow gradients of chemoattractants. Dawes and Edelstein-Keshet [2007] model small GTPase signaling pathways coupled to motility in 1d. Xiong et al. [2010] use a LEGI-model to describe dictyostelium response to chemoattractants. Similarly, Hecht et al. [2011] use a reaction-diffusion system to model the formation of patches of an activator molecule at the membrane, and couple it to a mechanical model of the membrane to simulate protrusion formation and dictyostelium motility in response to external cues. In this model, an "internal direction" and a graded response of the cell to the strength of the external stimulus is assumed, without specifying a precise underlying mechanism. Such a molecular mechanism has been proposed by Levine et al. [2006].

11. *(Spontaneous) cell polarization* is closely related to the previous point since it is always the first step of chemotaxis. However, whether purely mechanical cues, like membrane tension, are sufficient for establishing and maintaining cell polarity (as demonstrated experimentally by Houk et al. [2012]), or intrinsic signaling is essential, has to be further studied. Zemel et al. [2010b] take a step in that direction and show that stress fiber alignment depends on matrix rigidity.

12. *The shape of cells.* A prominent example is the filament model by Keren et al. [2008] accounting for the shape variability in keratocytes. Another example reproducing cell shape is the model by Kabaso et al. [2011]. Satulovsky et al. [2008] reproduce the shape of dictyostelium, fibroblasts, keratocytes and neurons with their top-down rule-based model built on a LEGI-mechanism.

13. *Morphodynamic patterns at the leading edge of cells.* Models accounting for patterns are reviewed in Ryan et al. [2012]. Shlomovitz and Gov [2007] find membrane waves due to the aggregation of curvature-sensing, actin activating membrane proteins coupled to myosin contraction. Contraction is also necessary to generate waves in the continuum two-phase flow model by Kuusela and Alt [2009]. Enculescu et al. [2010] can reproduce measured morphodynamic patterns with a myosin independent model. Carlsson [2010] simulates actin density waves at the ventral membrane with his explicit filament model. Doubrovinski and Kruse [2011] also model such polymerization waves in a mean field description and show that they can give rise to lateral waves at the leading edge of spreading cells. Morphodynamics are also closely related to cell shape.

14. *The distribution of traction forces and gel flow velocities within a cell, retrograde flow,* were predicted by continuum models, e.g. the theory of the active polar gel by Kruse et al. [2005, 2006].

15. *Contraction.* It is commonly accepted that contraction at the rear of the lamellipodium mostly arises from myosin motors sliding along actin filaments, though not many modeling studies have addressed this problem. Kruse and Jülicher [2000] study filament bundles connected by motor proteins. In continuum models, contraction usually enters as an active contractile stress. Zajac et al. [2008] show that depolymerization of the actin network can also lead to contraction.

16. *The force-velocity relation of keratocytes, Listeria and actin networks.* With most of the models that account for movement, it is possible to calculate a force-velocity relation. The tethered ratchet model has a convex force-velocity relation (Mogilner and Oster [2003]). This prediction was in agreement with the Listeria measurements, reflecting the force-velocity relation of single filaments (McGrath et al. [2003]). Some models provide an explanation for the force-velocity relation of filament networks (Carlsson [2003], Lee and Liu [2009], Weichsel and Schwarz [2010]) (see also the Discussion chapter 5 of this thesis). However, the force-velocity relation of keratocytes has only been modeled satisfactorily in Zimmermann et al. [2012] (this thesis).

Though some models account for several of the points, like polarization, chemotaxis, shape and morphodynamic patterns of dictyostelium (Hecht et al. [2011]), an integrated model describing all the features of actin based motility however remains elusive. It is also not clear to which extend different cell types and pathogens use the same mechanisms and can be described by the same model. It is of course not possible to include processes on different scales, like detailed adhesion formation and whole cell movement, in one model. A "bottom-up" approach starts from detailed microscopic modeling of the underlying processes and subsequently simplifications are made to describe processes on a higher level. A "top-down" approach does not start from molecular mechanisms but makes assumptions to correctly describe the macroscopic phenomena and then evaluates which could be the underlying. Both approaches lead to a better understanding of cell motility. A big challenge for the future is modeling of cell motility in 3d, since all the mentioned models are 1d or 2d models, but realistic *in vivo* motion occurs in 3d.

3 The model

In the mathematical model presented in this chapter, we distinguish two regions of the actin network inside the lamellipodium. In the bulk, we find a dense cross-linked actin gel (red in Fig. 3.1). At the leading edge, the newly polymerized tips of the actin filaments (green) are not cross-linked yet, can freely fluctuate and form a boundary layer called semiflexible region (SR). We draw a sharp boundary between SR and gel that is defined by the density of bound cross-linkers. In Fig. 3.1, a sketch of the SR is shown and all processes that will finally be accounted for in the model are depicted: polymerization and elongation of actin filaments, attachment of cross-linkers, retrograde flow in the gel, attachment of filament ends to the leading edge membrane, detachment of attached filaments, nucleation of filaments, capping and severing. We perform our calculations on a one dimensional cross section through the flat lamellipodium.

The model will be developed in three steps, corresponding to succeeding publications. A microscopic model of the SR with constant filament density was first described in Gholami et al. [2008] and will be explained in section 3.1. In section 3.2, the retrograde flow at the gel boundary is calculated with the theory of the active polar gel and included in the model. This has been published in Zimmermann et al. [2010]. Finally, a variable filament density due to nucleation of new, and capping and severing of existing filaments is introduced in section 3.3. Analytical calculations were published in Faber et al. [2010], but important approximations for fast computations are first presented here.

3.1 Basic Microscopic Model

The forces that the single filaments in the SR exert on the membrane determine the velocity of the leading edge. Support is provided by the actin gel. Filaments in the SR can attach to the leading edge membrane via linker proteins. Attached filaments can then not only push, but also pull the membrane. Therefore we have to calculate the forces of attached and detached filaments.

3.1.1 Filament forces

Detached filaments

The bending energy of a polymer κ/l equals the thermal energy k_BT at the persistence length $l = l_p$. Semiflexible actin filaments posses a persistence length l_p of about 15 µm. Therefore, detached filaments are subject to Brownian motion at the length scale of cells.

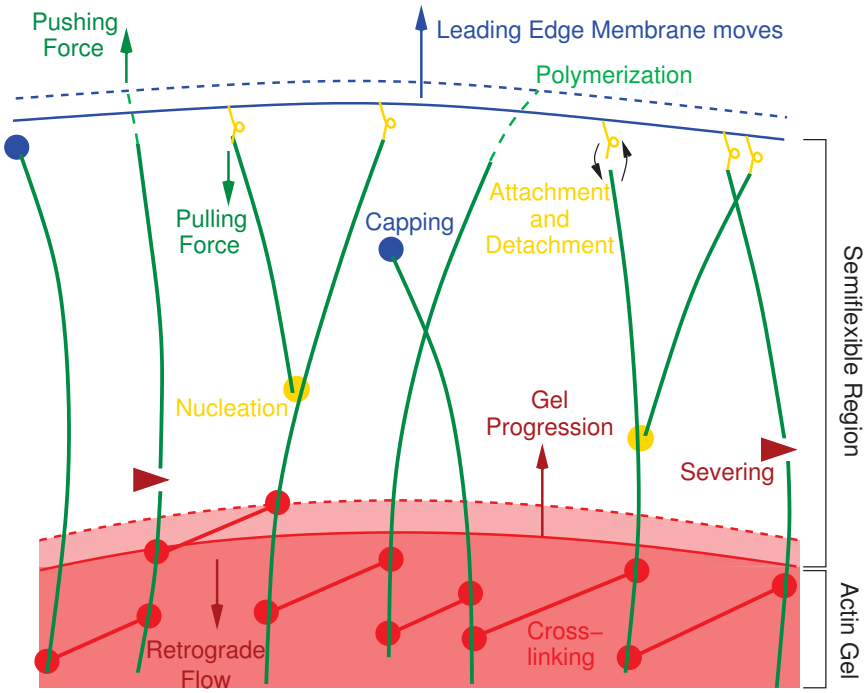

Figure 3.1: Schematic representation of processes included in the model. The actin filaments (*green*) in the semiflexible region (SR) can fluctuate and bend. They exert forces on the leading edge membrane (*blue line*) and push it forward. They elongate by polymerization and shorten by attachment of cross-linkers (*red dumbbells*) which advances the gel boundary (*red line*). Retrograde flow in the actin gel counteracts forward motion of the gel boundary. Filaments can also attach to the leading edge membrane and exert a pulling force. New filaments are nucleated from attached filaments. Filaments can get capped or severed and vanish into the gel afterwards.

Filaments of contour length l grafted at one end exert an entropic force on an obstacle at distance z. The force is calculated in Gholami et al. [2006]. The obstacle is considered as a rigid wall and constrains the Brownian fluctuations of the filament, which leads to an increase in free energy. This results, on time scales larger than the relaxation time of the polymer, in a force exerted on the wall. The entropic force can be written as

$$\langle F_d \rangle(z) = k_B T \frac{\partial}{\partial z} \ln \mathcal{Z}(z), \tag{3.1}$$

where $\mathcal{Z}(z)$ is the partition sum (a path integral over all possible polymer configurations). Upon defining the free energy $\mathcal{F}(z) = -k_B T \ln \mathcal{Z}(z)$ it reads

$$\langle F_d \rangle(z) = -\frac{\partial}{\partial z} \ln \mathcal{F}(z). \tag{3.2}$$

Using a hard wall potential for the obstacle, the entropic force can be expressed as

$$\langle F_d \rangle(z) = k_B T \frac{\mathcal{P}(z)}{\mathcal{Z}(z)}. \tag{3.3}$$

Hence, the probability density distribution $\mathcal{P}(z)$ has to be calculated (see Gholami et al. [2006]).

It is now assumed that the filament is oriented orthogonal to the wall at its grafting point. The entropic force is calculated in three spatial dimensions. We introduce a scaling variable

$$\tilde{\rho} = \frac{l - \zeta}{l_{||}} \tag{3.4}$$

that expresses the compression of a filament in units of the length $l_{||} = l^2/l_p$. It is shown, that the probability density of finding the tip of a filament at position ζ can be written as

$$\mathcal{P}(\zeta, l, l_p) = l_{||}^{-1} \tilde{\mathcal{P}}(\tilde{\rho}). \tag{3.5}$$

The restricted partition sum is given by integrating the probability distribution:

$$\mathcal{Z}(z) = \int_{-l}^{z} d\zeta \mathcal{P}(\zeta). \tag{3.6}$$

The calculation yields that it has a scaling property

$$\mathcal{Z}(z, l, l_p) = \tilde{\mathcal{Z}}(\tilde{\eta}), \tag{3.7}$$

with the scaling variable

$$\tilde{\eta} = \frac{l - z}{l_{||}}. \tag{3.8}$$

Combining equations 3.3, 3.5 and 3.7, the entropic force can be written as

$$F_d(z) = \frac{k_B T}{l_{||}} \frac{\tilde{\mathcal{P}}(\tilde{\eta})}{\tilde{\mathcal{Z}}(\tilde{\eta})}. \tag{3.9}$$

It shows a scaling behavior

$$F_d(z, l, l_p) = F_{crit} \tilde{F}(\tilde{\eta}), \tag{3.10}$$

where

$$F_{crit} = \frac{\pi^2}{4} \frac{k_B T}{l_{||}} \tag{3.11}$$

is the critical force for the buckling instability of a classical Euler-Bernoulli beam. In Gholami et al. [2006], it is shown that for small compression $\tilde{\eta} \lessapprox 0.2$ the scaling function

of the entropic force can well be approximated as

$$\tilde{F}^{<}(\tilde{\eta}) = \frac{4\exp(-\frac{1}{4\tilde{\eta}})}{\pi^{5/2}\tilde{\eta}^{3/2}\left[1-2\,\mathrm{erfc}\left(1/(2\sqrt{\tilde{\eta}})\right)\right]}. \tag{3.12}$$

For $\tilde{\eta} \gtrapprox 0.2$ the calculation yields

$$\tilde{F}^{>}(\tilde{\eta}) = \frac{1-3\exp(-2\pi^2\tilde{\eta})}{1-\frac{1}{3}\exp(-2\pi^2\tilde{\eta})}. \tag{3.13}$$

Hence, the scaling function increases monotonically with increasing $\tilde{\eta}$ in 3d. It approaches the Euler buckling force, which presents an upper limit for the entropic force. These analytical results are valid in the "weakly bending limit" for $\epsilon = l/l_p \lessapprox 0.1$.

Attached filaments

The situation is different for attached filaments. Those filaments can, depending on their length, exert pushing or pulling forces. The tip of the filament is always positioned at the membrane and cannot fluctuate. The proteins linking the filaments to the membrane are assumed to behave like elastic springs. We distinguish three different regimes for the force f_a exerted by the serial arrangement of polymer and linker, depending on the relation between the depth of the semiflexible region z, the equilibrium end-to-end distance $R_{||} = l(1 - l/2l_p)$, and the contour length l (Gholami et al. [2008]):

$$F_a(l,z) = \begin{cases} -k_{||}(z - R_{||}),\ z \le R_{||}, & \text{i)} \\ -k_{eff}(z - R_{||}),\ R_{||} < z < l, & \text{ii)} \\ -k_l(z-l) - k_{eff}(l - R_{||}),\ z \ge l. & \text{iii)} \end{cases} \tag{3.14}$$

The three cases correspond to: i) a compressed filament pushes against the membrane; ii) filament and linker pull the membrane while being stretched together; iii) a filament is fully stretched but the linker continues to pull the membrane by being stretched further. Here, $k_{||}$, k_l and $k_{eff} = k_l k_{||}/(k_l + k_{||})$ are the linear elastic coefficients of polymer, linker and serial polymer-linker arrangement, respectively. For $k_{||}$ we use the linear response coefficient of a worm-like chain grafted at both ends $k_{||} = 6k_BTl_p^2/l^4$ (Kroy and Frey [1996], Kroy [1998]).

3.1.2 Rates of filament elongation, shortening and exchange

While the total density of filaments n is first assumed to be conserved, there are transitions between the populations of attached and detached filaments. Detached filaments attach to the membrane with a constant rate k_a. The detachment rate of attached filaments is force-dependent since a pulling force facilitates detachment. It can be expressed as

$$k_d = k_d^0 \exp(-dF_a/k_BT), \tag{3.15}$$

with the force-free detachment rate k_d^0. The length d added by an actin monomer to the filament is 2.7 nm.

Detached filaments can polymerize and grow. The velocity of polymerization is also force dependent because the probability, that the filament fluctuates away from the membrane and a gap, sufficiently large for an actin monomer, appears, decreases with increasing force (Mogilner and Oster [1996]). The polymerization velocity reads

$$v_p = v_p^{max} \exp(-dF_d/k_BT). \tag{3.16}$$

The maximum polymerization velocity v_p^{max} depends on the actin monomer concentration. Unlike detached filaments, attached filaments do not polymerize.

The filaments shorten by the attachment of cross-linking molecules and incorporation of filament length into the actin gel. The gel boundary is defined by a certain concentration of bound cross-linkers beyond which the actin network is considered a gel. The cross-linking velocity is contour length dependent, since cross-linkers have had more time to bind to longer existing filament parts. It is unlikely that very short filaments get cross-linked. In the next section (see also Zimmermann et al. [2010]), we show that the cross-linking velocity can be expressed as

$$v_g(l, n) = \hat{v}_g^{max} n \tanh(nl/\bar{l}). \tag{3.17}$$

It is proportional to the filament density n, because denser filament packing allows cross-linkers to span the inter-filament distance more easily. In the rate of filament shortening

$$\tilde{v}_g(l, z, n) = v_g \max(1, l/z) \tag{3.18}$$

the additional factor l/z accounts for the fact that a larger portion of filament length is incorporated into the gel during cross-linking when filaments are bent.

3.1.3 Derivation of cross-linking rate

This section is taken from Zimmermann et al. [2010].

The transition from the semiflexible region with little cross-links to the gel with many cross-links occurs gradually. The concentration of cross-linkers bound to the actin network C_b is saturated far inside the gel and decreases towards the leading edge membrane to 0, since newly polymerized filament parts have no cross-linker bound yet. We denote as the gel boundary the position of a concentration value C_b^{crit}, above which we expect gel-like behavior of the network. We calculate the cross-linking velocity v in stationary state with steady motion. We consider a reference frame along the contour length of a filament in which the gel boundary is fixed. The tip of the filament is located at $x = 0$ and the gel boundary at $x = -l$. We denote with L_G the width of the gel region of the lamellipodium close to the gel boundary where C_b is not saturated yet. C_f is the concentration of free cross-linkers. We have a pool of cross-linkers in the cell body of constant concentration C_f^{cb}. We use a constant binding rate of cross-linkers in order to obtain linear, analytically solvable differential equations for the concentrations. We

describe binding of cross-linkers in the SR by the rate p and binding inside the gel by p_G with $p_G \leq p$. That allows taking partial saturation of binding sites inside the gel into account. The stationary spatial distributions of bound and unbound cross-linkers are described by

$$\begin{aligned} D\frac{\partial^2 C_f}{\partial x^2} - p_G C_f &= 0, \text{ gel}, \\ D\frac{\partial^2 C_f}{\partial x^2} - pC_f &= 0, \text{ SR}, \\ v\frac{\partial C_b}{\partial x} + pC_f &= 0, \text{ SR}, \end{aligned} \tag{3.19}$$

with the diffusion coefficient D. Boundary conditions at the gel boundary guarantee a continuous and smooth function C_f. Additionally, we require

$$C_f(-(L_G + l)) = C_f^{cb} \quad \text{and} \quad \frac{\partial C_f}{\partial x}\Big|_{x=0} = 0\,. \tag{3.20}$$

The solution for C_f in the SR $-l \leq x \leq 0$ is given by

$$\begin{aligned} C_f &= \frac{GC_f^0 \cosh(kx)}{k\sinh(kl) + G\cosh(kl)},\ k = \sqrt{\frac{p}{D}}, \\ G &= \frac{k_G}{\tanh(k_G L_G)},\ C_f^0 = \frac{C_f^{cb}}{\cosh(k_G L_G)},\ k_G = \sqrt{\frac{p_G}{D}}\,. \end{aligned} \tag{3.21}$$

With the boundary condition $C_b(0) = 0$, the solution for the bound cross-linker concentration inside the SR reads:

$$C_b = -\frac{p}{vk}\frac{GC_f^0 \sinh(kx)}{k\sinh(kl) + G\cosh(kl)}\,. \tag{3.22}$$

Reaching the critical concentration of cross-linkers bound to filaments C_b^{crit}, above which the actin network becomes a gel, defines the gel boundary $x = -l$ and we can write

$$\frac{p}{vk}\frac{GC_f^0 \sinh(kl)}{k\sinh(kl) + G\cosh(kl)} = C_b^{crit}\,. \tag{3.23}$$

The cross-linking velocity is then given by

$$v = \frac{p}{C_b^{crit} k}\frac{GC_f^0 \tanh(kl)}{k\tanh(kl) + G}\,. \tag{3.24}$$

We assume that the binding rate p is proportional to the filament density n squared, since filaments have to get sufficiently close to each other to cross-link: $p = bn^2$. That

yields in the limit $G \gg k \tanh(kl)$

$$v = \frac{nC_f^0\sqrt{Db}}{C_b^{crit}} \tanh(nl\sqrt{b/D})\,. \tag{3.25}$$

That is, we retrieve Eq. 3.17 with $\hat{v}_g^{max} = C_f^0\sqrt{Db}/C_b^{crit}$ and $\bar{l} = 1/\sqrt{b/D}$.

The contour length in the semiflexible region rarely approaches 0. Even when the leading edge motion is stalled, retrograde flow maintains an SR and the cross-linking velocity compensates for the flow. Nevertheless, we would like to add a remark applying to the case $l \to 0$. We need to take into account that cross-linker binding sites are located at average distances l_b along the filament, if l becomes smaller than l_b. For $l \ll l_b$, the probability to find a cross-linker between $x = 0$ and $x = -l$ is l/l_b. That probability turns the cross-linker binding rate into $p = bn^2 l/l_b$. Therefore the cross-linking velocity Eq. 3.24 then reads

$$v = \frac{\sqrt{Dbl/l_b}nC_f^0 G}{C_b^{crit}} \frac{\tanh(n\sqrt{bl^3/(Dl_b)})}{\sqrt{bl/(Dl_b)}\tanh(n\sqrt{bl^3/(Dl_b)}) + G}\,. \tag{3.26}$$

3.1.4 Dynamic equations and monodisperse approximation

The length distributions of attached filaments $N_a(l)$ and detached filaments $N_d(l)$ change due to shortening of attached and detached filaments by cross-linking, elongation by polymerization of detached filaments only and transitions between both populations:

$$\frac{\partial}{\partial t}N_d(l,t) = \frac{\partial}{\partial l}((\tilde{v}_g - v_p)N_d(l,t)) + k_d N_a(l,t) - k_a N_d(l,t), \tag{3.27}$$

$$\frac{\partial}{\partial t}N_a(l,t) = \frac{\partial}{\partial l}(\tilde{v}_g N_a(l,t)) - k_d N_a(l,t) + k_a N_d(l,t). \tag{3.28}$$

The assumption that attached filaments do not polymerize excludes formins as the polymerization mechanism from the model. However, one could simply add polymerization in the convection term (after the derivative with respect to l) in Eq. 3.28 to include them.

It has been shown (Gholami et al. [2008]) that the length distributions quickly collapse to narrow distributions around the mean length of attached or detached filaments, l_a or l_d, due to the existence of a root with positive length derivative of the convection term of 3.27. To simplify the calculations we replace them by delta-distributions $N_d(l,t) = n_d\delta(l - l_d(t))$ and $N_a(l,t) = n_a\delta(l - l_a(t))$, where n_d and n_a are the total densities of detached and attached filaments. Inserting the ansatz into Eq. 3.27 and integrating over l we find

$$\begin{aligned}\int_0^\infty \dot{n}_d\delta(l-l_d)dl - \int_0^\infty n_d\dot{l}_d\frac{\partial}{\partial l}\delta(l-l_d)dl \\ = \int_0^\infty \frac{\partial}{\partial l}[(\tilde{v}_g - v_p)n_d\delta(l-l_d)]dl + \int_0^\infty k_d(l)n_a\delta(l-l_a)dl - \int_0^\infty k_a n_d\delta(l-l_a)dl,\end{aligned}$$

which, by evaluating the integrals, leads to

$$\dot{n}_d = k_d(l_a, z)n_a(t) - k_a n_d(t). \tag{3.29}$$

Assuming a constant filament density n, the density of attached filaments is given by $n_a = n - n_d$.

Comparing

$$\frac{\partial}{\partial t}\int_0^\infty lN_d(l,t)dl = \frac{\partial}{\partial t}\int_0^\infty ln_d\delta(l - l_d(t))dl = \frac{\partial}{\partial t}(l_d n_d) = \dot{l}_d n_d + l_d(k_d n_a - k_a n_d)$$

and

$$\begin{aligned}\frac{\partial}{\partial t}\int_0^\infty lN_d(l,t)dl &= \int_0^\infty l\frac{\partial}{\partial t}N_d(l,t)dl \\ &= \int_0^\infty l\left(\frac{\partial}{\partial l}((\tilde{v}_g - v_p)N_d(l,t)) + k_d N_a(l,t) - k_a N_d(l,t)\right)dl \\ = l((\tilde{v}_g - v_p)N_d(l,t))|_0^\infty - \int_0^\infty (\tilde{v}_g(l) - v_p(l))N_d(l,t)dl + \int_0^\infty lk_d(l)N_a(l,t) - lk_a N_d(l,t)dl \\ &= -(\tilde{v}_g(l_d) - v_p(l_d))n_d(t) + l_a k_d(l_a)n_a(t) - l_d k_a n_d(t)\end{aligned}$$

gives the dynamics of the mean length of detached filaments

$$\dot{l}_d = -(\tilde{v}_g(l_d, z) - v_p(l_d, z)) + k_d(l_d, z)\frac{n_a(t)}{n_d(t)}(l_a(t) - l_d(t)). \tag{3.30}$$

The analogous calculation for the dynamics of the length of attached filaments yields

$$\dot{l}_a = -\tilde{v}_g(l_d, z) + k_a(l_d, z)\frac{n_d(t)}{n_a(t)}(l_d(t) - l_a(t)). \tag{3.31}$$

Going back to Eqs. 3.27, 3.28 we see that the right-hand sides will be zero for $N_a = N_d = 0$. That means the length distributions, and consequently the total number as well as the mean lengths, do not change for zero filaments. Accordingly, the length of the first filament created for a protrusion is undetermined. Similarly, the filament number can vanish and the protrusion disappear even for long filaments without shortening.

The dynamics of the distance z between the membrane and the gel boundary is given by the difference of membrane velocity and gel velocity

$$\begin{aligned}\frac{\partial}{\partial t}z = \frac{1}{\kappa}\int_0^\infty [N_a(l,t)F_a(l,z) + N_d(l,t)F_d(l,z)]dl \\ - \frac{1}{n}\int_0^\infty v_g(l)[N_a(l,z) + N_d(l,z)]dl.\end{aligned} \tag{3.32}$$

All viscous drag and friction counteracting membrane motion is described by the coefficient κ. We assume here that the gel simply advances by cross-linking of the steadily

polymerizing filament tips. Retrograde flow is neglected for the time being. It will be included into the system in the following section. In the monodisperse approximation, the z-dynamics reads

$$\dot{z} = \frac{1}{\kappa}[n_a(t)F_a(l_a, z) + n_d(t)F_d(l_d, z)] - \frac{1}{n}[n_a(t)v_g(l_a) + n_d(t)v_g(l_d)]. \tag{3.33}$$

3.2 The velocity of the gel boundary: including retrograde flow

It has been shown that the cross-linked actin network inside the lamellipodium has viscoelastic properties. It behaves like an elastic solid on short time scales and like a viscous fluid on longer time scales. A typical value for the viscoelastic relaxation time, that characterizes the solid to fluid transition, is 3 s, which is also in agreement with the typical binding times of cross-linkers (Wottawah et al. [2005]).

Continuum models for the lamellipodium describe protrusion and the flow and forces inside the actin gel. One special feature that is found in cells and cannot be reproduced with our basic microscopic model is the dynamics of the backwards directed gel retrograde flow. While the filaments keep polymerizing at the leading edge of the lamellipodium, the actin network itself moves opposite to the direction of motion because: a) forces acting on the leading edge are also exerted on the gel and push it backwards, and b) contractile forces occur inside the gel, e.g. due to the action of myosin motor molecules.

In our microscopic model, retrograde flow affects the velocity of the gel boundary. To find an expression for the retrograde flow as a function of filament and contractile forces, we use the theory of the active polar gel (Kruse et al. [2005, 2006]). Its equations are solved in the viscous limit for a cross-section through the lamellipodium in a thin film approximation and under the assumption of stationary motion. An algebraic expression for the retrograde flow is found by solving the differential equations for different force boundary conditions and different values of the cross-linking rate. The two following sections are taken in a slightly modified form from Zimmermann et al. [2010].

3.2.1 The gel model

We use the theory of the active polar gel developed by Kruse et al. [2005]. In the thin film approximation, one takes a radial cross-section through the lamellipodium and averages over its height (see Fig. 3.2). It yields the simplified one-dimensional constitutive equation (Kruse et al. [2006])

$$\frac{dv}{dx} = \frac{1}{4\eta}\left(\frac{f(x)}{h(x)} - \mu\right), \tag{3.34}$$

with the gel viscosity η and the active contractile stress μ from motor molecules. Stress in the gel is described by the force $f(x)$. The height of the gel film is denoted by $h(x)$,

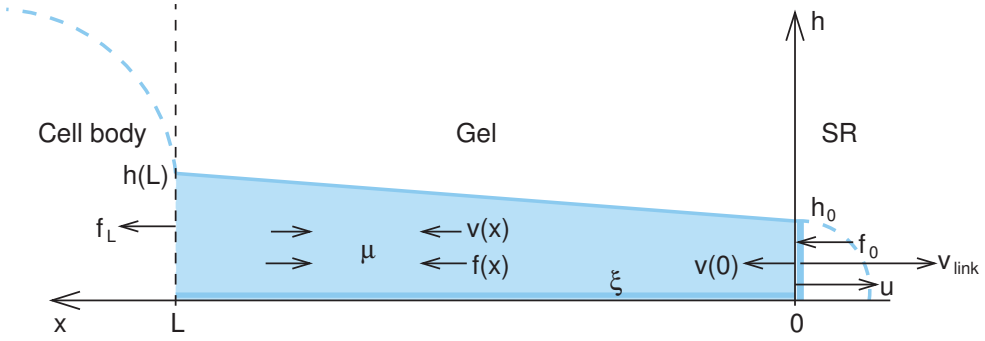

Figure 3.2: Schematic representation of the bulk of the lamellipodium described by the theory of active polar gels (see Kruse et al. [2006]). The cross-section through the thin lamellipodium is assumed to have a stationary height profile $h(x)$ and length L. It is characterized by a gel flow $v(x)$ and stress inside the gel $f(x)$. The gel has a viscosity η, friction of the gel with the substrate due to adhesions is described by the coefficient ξ, and there is an active contractile stress μ. The gel boundary with the SR at $x = 0$ moves with the velocity u. The forward motion due to cross-linking with the velocity v_{link} is counteracted by a retrograde flow, i.e. the gel flow at the boundary $v(0) = v_0$. We solve the gel equations 3.34-3.36 and calculate the retrograde flow and the velocity of the gel boundary for different force boundary conditions at the SR boundary $f(0) = f_0$ and at the cell body $f(L) = f_L$.

and $v(x)$ is the flow field in the lab frame. We neglect inertial forces in the force-balance

$$\frac{df}{dx} = \xi v(x), \tag{3.35}$$

where ξ is the friction coefficient of the gel with the substrate, which also describes adhesion (Kruse et al. [2006]).

Equations 3.34, 3.35 can be solved when boundary conditions for the force at the gel front $f(0) = f_0$ and at the cell body $f(L) = f_L$ are specified and an expression for the height profile $h(x)$ is given. This expression can be obtained from integrating the continuity equation

$$\frac{d}{dx}\left[(v(x) + v_{link} - v(0))\, h(x)\right] = h_0 v_{link} \delta(x). \tag{3.36}$$

Gel is produced at the gel front $x = 0$ (with height $h(0) = h_0$) by cross-linking the filaments of the semiflexible region at a velocity v_{link}. The velocity of the gel front is given by $u = v_{link} - v(0)$. We use the same velocity definitions as Kruse et al. [2006], i.e., $v(x)$ is directed opposite to u and v_{link}.

In conjunction with the semiflexible region model, we will use Eqs. 3.34-3.36 for the gel behavior in a quasi-steady approximation. Some cells like e.g. keratocytes move with a stationary shape of the lamellipodium, but in others the semiflexible region dynamics may become non-stationary. Results of the model indicate that even when the plasma

membrane shows an oscillatory movement, the gel still moves with a constant velocity in a wide parameter range (Zimmermann et al. [2010]). Additionally we performed calculations using a time-dependent continuity equation (Zimmermann [2009]) and could show that a stationary solution for the height profile $h(x,t)$ is usually reached after a few seconds, a short timescale compared to oscillation periods. We conclude that the assumption of a quasi-stationary gel profile is a good approximation, even when we couple the gel to the semiflexible region dynamics.

3.2.2 Solving the gel model: expression for the retrograde flow

To obtain an expression for the gel boundary velocity u that depends on force boundary conditions and gel parameters, we scale Eqs. 3.34-3.36 by using

$$v' = \frac{v}{v_{link}}, \quad x' = \frac{x}{L}, \quad f' = \frac{f}{L\xi v_{link}}.$$

Using Eq. 3.36, the differential equation 3.34 can be written as

$$\frac{dv}{dx} = \frac{1}{4\eta}\left(\frac{f(x)\,(v(x)+u)}{h_0 v_{link}} - \mu\right).$$

With Eq. 3.35, we get

$$\frac{d^2 f'}{dx'^2} = \nu_1 f' \cdot \left(\frac{df'}{dx'} + 1 - \frac{df'}{dx'}|_0\right) - \nu_2$$

and the scaling parameters

$$\nu_1 = \frac{\xi L^2}{h_0 4\eta}, \quad \nu_2 = \frac{\mu L}{4\eta v_{link}}.$$

We now solve this equation numerically for different ν_1 and ν_2 as well as different force boundary conditions $f'(0)$ and $f'(1)$. Solving the boundary value problem demands finding the root of a function of $\frac{df'}{dx'}|_0$ (shooting method). The velocity u' is then given by $1 - \frac{df'}{dx'}|_0$.

It can be seen that, in good approximation, u' depends linearly on $f'(0)$ and $f'(1)$. We therefore assume that u' has the form $u' \approx af'(0) + bf'(1) + c$ and determine the coefficients a, b and c for different parameters ν_1 and ν_2. The results are shown in Fig. 3.3. a, b and c have been fit as functions of ν_1 and ν_2 by

$$\begin{aligned} a &= (1+0.92\nu_1)^{1/2}(1+0.03\nu_2), \\ b &= -\frac{1+0.1\nu_2}{1+0.15\nu_1+0.013\nu_1^2}, \\ c &= 1 - \frac{\nu 2}{2+0.12\nu_1}. \end{aligned} \tag{3.37}$$

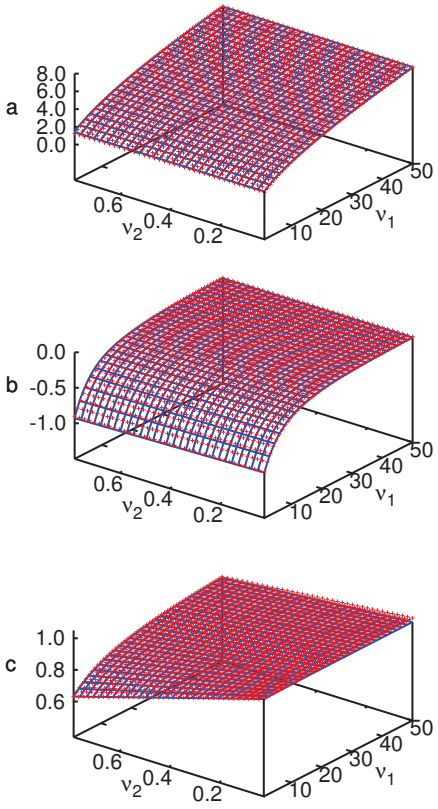

Figure 3.3: Parameters a, b and c of the fit $u' = af'(0)+bf'(1)+c$ as a function of ν_1 and ν_2. (*Blue crosses*) numerical solutions; (*red lines*) fitting functions 3.37. Fits and numerical solutions are so close that they are almost indistinguishable in the plots. Originally published in Zimmermann et al. [2010] (©2010 American Physical Society).

Scaling back to physical units yields

$$\begin{aligned} u &\approx v_{link} - \frac{\mu L}{4\eta} g_1 + \frac{f_0}{L\xi} g_2 - \frac{f_L}{L\xi} g_3, \\ g_1 &= \frac{1}{2.0 + 0.12 \frac{\xi L^2}{4\eta h_0}}, \\ g_2 &= \left(1.0 + 0.92 \frac{\xi L^2}{h_0 4\eta}\right)^{1/2} \left(1.0 + 0.03 \frac{\mu L}{4\eta v_{link}}\right), \\ g_3 &= \frac{1.0 + 0.1 \frac{\mu L}{4\eta v_{link}}}{1.0 + 0.15 \frac{\xi L^2}{h_0 4\eta} + 0.013 \left(\frac{\xi L^2}{h_0 4\eta}\right)^2}. \end{aligned} \tag{3.38}$$

We have fit g_1, g_2, g_3 for $0 \leq \frac{\xi L^2}{4\eta h_0} \leq 50$. Equations. 3.38 are valid on condition that $\frac{\mu L}{4\eta v_{link}} < 1$, since the solution of the gel equations 3.34-3.36 diverges at finite L [1].

The gel front moves slower than the cross-linking velocity v_{link} since the gel flows backwards. The second term on the right-hand side of Eq. 3.38 characterizes the retrograde flow due to contraction by myosin motors in the absence of external forces. Contraction slows down or (depending on other parameters) even retracts the gel front in agreement with experimental observations. The term proportional to f_0 reflects the retrograde flow due to filaments of the semiflexible region pushing against the gel front. A negative value of f_0 corresponds to a pushing force, which increases the retrograde flow and decreases the gel velocity u. The retrograde flow is fast for small $L\xi$, since the gel does not have the grip to stand the force exerted by the boundary layer. The cell will slow down or stop. Increasing $L\xi$ increases the cell velocity by providing grip with the substrate. Similarly, increasing the viscosity also increases u, since the gel provides better support for pushing the membrane.

The factor g_3 of the force at the cell body f_L decreases quickly with increasing friction ξ and length of the lamellipodium. That illustrates the absorption of forces at the back by adhesion sites. At realistic parameter values (see Zimmermann et al. [2010]) $g_2/g_3 \approx 40$ holds, i.e., the effect of f_0 on the gel boundary velocity is much larger than the one of f_L. Therefore, we will use $f_L = 0$ in the following.

The force exerted by the filaments on the leading edge membrane also acts on the gel boundary. Therefore, the force boundary condition is given by

$$f_0 = -(n_a F_a(l_a, z) + n_d F_d(l_d, z)). \tag{3.39}$$

Gel is produced at the average rate of cross-linking

$$v_{link} = (n_a v_g(l_a) + n_d v_g(l_d))/n. \tag{3.40}$$

[1] Despite that condition, there is a solution at v_{link}=0, with $v(x) = -u$, $u = (f_0 - f_L)/(L\xi)$ and $h(x) = \mu f(x)$, i.e., contraction forces exactly balance $f(x)$, and motion arises for $f_0 - f_L \neq 0$ only.

The equation for the z-dynamics 3.33 then changes to

$$\dot{z} = \frac{1}{\kappa}[n_a(t)F_a(l_a, z) + n_d(t)F_d(l_d, z) - f_{ext}] - u(v_{link}, f_0), \tag{3.41}$$

with expression 3.38 used for u. We have also included an external force f_{ext} that acts on the leading edge.

3.3 Capping, Nucleation and Severing

3.3.1 Dynamics of attached and detached filaments

We now also include a change in filament density in the SR by nucleation of new and capping of existing filaments (see Faber et al. [2010]). We consider the length distribution of attached $N_a(l,t)$, detached $N_d(l,t)$ and capped filaments $N_c(l,t)$. Their dynamics are described by the following equations:

$$\frac{\partial}{\partial t}N_d(l,t) = \frac{\partial}{\partial l}((\tilde{v}_g - v_p)N_d(l,t)) + k_d N_a(l,t) - k_a N_d(l,t) - k_c N_d(l,t), \tag{3.42}$$

$$\frac{\partial}{\partial t}N_a(l,t) = \frac{\partial}{\partial l}(\tilde{v}_g N_a(l,t)) - k_d N_a(l,t) + k_a N_d(l,t) + k_n N_a(l,t), \tag{3.43}$$

$$\frac{\partial}{\partial t}N_c(l,t) = \frac{\partial}{\partial l}(\tilde{v}_g N_c(l,t)) + k_c N_d(l,t). \tag{3.44}$$

Detached filaments may get capped. The binding rate of capping proteins is force dependent, similar to the attachment of actin monomers to the filament barbed ends during polymerization. We find an Arrhenius factor in the capping rate

$$k_c = k_c^{max} \exp(-F_d d/k_B T). \tag{3.45}$$

New filament branches are nucleated by Arp2/3 off attached filaments with a nucleation rate k_n. When a new filament branches from a mother filament, its length is initially two monomer diameters, but only after it has grown to span the whole width between gel and membrane, it enters the force balance and contributes to the gel boundary velocity. Hence, only then it contributes to the dynamics. Consequently, filaments emerge with the length of the mother filament in our model. The nucleation process is autocatalytic, i.e., nucleation is proportional to the number of attached filaments. Since the branching point vanishes into the gel quickly, we treat mother and daughter filament as two separate filaments with respect to their force-extension relation. The number of Arp2/3 proteins is assumed to be limited and the density of available nucleation sites decreases with increasing total number of filaments so that the effective nucleation rate reads

$$k_n = k_n^0 - k_n^N n, \tag{3.46}$$

with k_n^0 and k_n^N constant.

Analogous to the calculations in section 3.1.4, the δ-ansatz used in Eqs. 3.42, 3.43 leads to ordinary differential equations for the total density of attached and detached filaments n_a and n_d, and for their mean lengths l_a and l_d (see also Faber et al. [2010])

$$\dot{n}_d = k_d(l_a, z)n_a(t) - (k_a + k_c(l_d, z))n_d(t), \tag{3.47}$$

$$\dot{n}_a = k_a n_d(t) - (k_d(l_a, z) - k_n)n_a(t), \tag{3.48}$$

$$\dot{l}_d = -(\tilde{v}_g(l_d, z, n) - v_p(l_d, z)) + k_d(l_a, z)\frac{n_a(t)}{n_d(t)}(l_a(t) - l_d(t)), \tag{3.49}$$

$$\dot{l}_a = -\tilde{v}_g(l_a, z, n) + k_a\frac{n_d(t)}{n_a(t)}(l_d(t) - l_a(t)), \tag{3.50}$$

$$\dot{z} = \frac{1}{\kappa}\left(F_d(l_d, z)n_d(t) + F_a(l_a, z)n_a(t) + f_c(n_d, l_d, z, n)\right) - u(v_{link}, f_0). \tag{3.51}$$

3.3.2 Length distribution of capped filaments

The monodisperse approximation is not valid for the distribution of capped filaments $N_c(l, t)$. Equation 3.44 is solved using the method of characteristics. Here, we assume that filaments are long when they get capped. We neglect the length dependence of v_g and only account for $\tilde{v}_g = \max(1, l/z)\hat{v}_g^{max}n$. As before, we use the notation $v_g^{max}(n) = \hat{v}_g^{max}n$. Furthermore, we are only interested in $N_c(l, t)$ for $z \leq l \leq l_d$, since for $l < z$, capped filaments exert no force. Hence, $\tilde{v}_g = \frac{l}{z}v_g^{max}$. Using the monodisperse approximation for the detached filaments $N_d(l, t) = n_d(t)\delta(l - l_d(t))$, equation 3.44 reads

$$\frac{\partial}{\partial t}N_c = \frac{v_g^{max}}{z}N_c + \frac{l}{z}v_g^{max}\frac{\partial}{\partial l}N_c + k_c(l_d)n_d(t)\delta(l - l_d). \tag{3.52}$$

With

$$\frac{dN}{ds} = \frac{\partial N}{\partial t}\frac{dt}{ds} + \frac{\partial N}{\partial l}\frac{dl}{ds} \tag{3.53}$$

we can identify the characteristics

$$\frac{dt}{ds} = 1\,, \quad \frac{dl}{ds} = -v_g^{max}\frac{l}{z} \tag{3.54}$$

and

$$\frac{dN_c}{ds} = \frac{v_g^{max}}{z}N_c + k_c(l_d)n_d(t)\delta(l - l_d). \tag{3.55}$$

The first equation (first of Eqs. 3.54) gives $s = t$ and therefore we get

$$\frac{dl}{dt} = -\frac{v_g^{max}}{z}l \tag{3.56}$$

with the solution (obtained by separation of variables)

$$l(t) = l(t^*) \exp\left(- \int_{t^*}^{t} \frac{v_g^{max}(t')}{z(t')} dt' \right). \tag{3.57}$$

The time of capping is denoted by t^*. To solve

$$\frac{dN_c}{dt} = \frac{v_g^{max}}{z} N_c + k_c(l_d) n_d(t) \delta(l - l_d) \tag{3.58}$$

requires a little more effort. The general solution of the inhomogeneous equation equals the sum of the solution of the homogeneous equation and a special solution of the inhomogeneous equation. The solution of the homogeneous equation reads

$$N_c^h = C \exp\left(\int_{t^*}^{t} \frac{v_g^{max}}{z} dt' \right). \tag{3.59}$$

The special solution of the inhomogeneous equation is found by variation of constants:

$$\begin{aligned} N_c^{sp} &= \left[\int_{t^*}^{t} dt' k_c(l_d(t')) n_d(t') \delta(l(t') - l_d(t')) \exp\left(- \int_{t^*}^{t'} \frac{v_g^{max}}{z} dt'' \right) \right] \exp\left(\int_{t^*}^{t} \frac{v_g^{max}}{z} dt' \right) \\ &= \int_{t^*}^{t} dt' k_c(l_d(t')) n_d(t') \delta(l(t') - l_d(t')) \exp\left(\int_{t'}^{t} \frac{v_g^{max}}{z} dt'' \right) \\ &= \frac{k_c(l_d(t^*)) n_d(t^*)}{|\frac{d}{dt'}(l(t') - l_d(t'))|_{t'=t^*}} \exp\left(\int_{t^*}^{t} \frac{v_g^{max}}{z} dt' \right). \end{aligned} \tag{3.60}$$

In the last line, we have used $\delta(g(x)) = \sum_{i=1}^{n} \frac{\delta(x - x_i)}{|g'(x_i)|}$, where x_i are the roots of $g(x)$. At the time of capping t^*, $l(t^*) = l_d(t^*)$ holds. Equation 3.57 yields

$$\exp\left(\int_{t^*}^{t} \frac{v_g^{max}}{z} dt' \right) = \frac{l_d(t^*)}{l(t)}$$

and

$$\frac{d}{dt} l(t)|_{t=t^*} = - \frac{v_g^{max}(t^*)}{z(t^*)} l_d(t^*).$$

Furthermore (Eq. 3.49),

$$\frac{d}{dt} l_d(t)|_{t=t^*} = - \frac{v_g^{max}(t^*)}{z(t^*)} l_d(t^*) + v_p(l_d(t^*)) + k_d(l_a(t^*)) \frac{n_a(t^*)}{n_d(t^*)} (l_a(t^*) - l_d(t^*)).$$

Hence, inserting those into 3.60 we find

$$N_c^{sp}(t, t^*) = \frac{k_c(l_d(t^*)) n_d(t^*)}{v_p(l_d(t^*)) + k_d(l_a(t^*)) \frac{n_a}{n_d}(t^*)(l_a(t^*) - l_d(t^*))} \frac{l_d(t^*)}{l(t)} \tag{3.61}$$

for $k_d(l_a(t^*))\frac{n_a}{n_d}(t^*)(l_a(t^*) - l_d(t^*)) > -v_p(l_d(t^*))$. To find the length distribution of capped filaments, t^* has to be calculated for every length l by solving $l = l_d(t^*)$. The number of capped polymers is determined by the number of detached polymers and the capping rate at the time of capping.

3.3.3 Total number, force and cross-linking rate of capped filaments

For calculating the total number, force and cross-linking rate, we require:

$$\begin{aligned}
\frac{\partial l}{\partial t^*} &= \frac{\partial}{\partial t^*}\left[l_d(t^*)\exp\left(-\int_{t^*}^{t}\frac{v_g^{max}(t')}{z(t')}dt'\right)\right] \\
&= \left[\dot{l}_d(t^*) - \left(-\frac{v_g^{max}}{z}(t^*)\right)l_d(t^*)\right]\exp\left(-\int_{t^*}^{t}\frac{v_g^{max}(t')}{z(t')}dt'\right) \\
&= \left[-\frac{v_g^{max}}{z}l_d(t^*) + v_p(t^*) + k_d\frac{n_a}{n_d}(l_a - l_d)(t^*) + \frac{v_g^{max}}{z}l_d(t^*)\right]\exp\left(-\int_{t^*}^{t}\frac{v_g^{max}}{z}dt'\right) \\
&= \left[v_p\left(l_d(t^*)\right) + k_d\left(l_a(t^*)\right)\frac{n_a}{n_d}(t^*)\left(l_a(t^*) - l_d(t^*)\right)\right]\exp\left(-\int_{t^*}^{t}\frac{v_g^{max}(t')}{z(t')}dt'\right).
\end{aligned}$$

The total density of capped filaments is then given by

$$n_c = \int_{z(t)}^{l_d(t)} dl N_c(l,t) = \int_{t_z^*}^{t} dt^* \frac{\partial l}{\partial t^*} N_c(t^*,t) = \int_{t_z^*}^{t} dt^* k_c\left(l_d(t^*), z(t^*)\right) n_d(t^*). \tag{3.62}$$

The lower integral boundary is $z(t)$ since shorter filaments do not exert any force. The corresponding time of capping of filaments with length z at time t is denoted by t_z^*. We again use Eq. 3.57

$$z(t) = l_d(t_z^*)\exp\left(-\int_{t_z^*}^{t}\frac{v_g^{max}(t')}{z(t')}dt'\right) \tag{3.63}$$

and apply a root finding algorithm to determine t_z^*. The total number of all filaments is given by $n = n_c + n_a + n_d$.

Along these lines, we can also calculate the total force of capped filaments

$$f_c = \int_{z(t)}^{l_d(t)} dl N_c(l,t) F_d(l,z) = \int_{t_z^*}^{t} dt^* k_c\left(l_d(t^*), z(t^*)\right) n_d(t^*) F_d\left(l(t^*), z(t)\right). \tag{3.64}$$

Note that we have to calculate $l(t^*)$ according to expression 3.57 for every t^*. The average cross-linking rate yields

$$v_g^c = \frac{1}{n}\int_{z(t)}^{l_d(t)} dl N_c(l,t) v_g(l,n) = \frac{1}{n}\int_{t_z^*}^{t} dt^* k_c\left(l_d(t^*), z(t^*)\right) n_d(t^*) v_g\left(l(t^*), n(t)\right). \tag{3.65}$$

Since the total number of filaments enters v_g^{max} and is therefore already required for determining t_z^* (Eq. 3.63), it is possible to replace the dynamics of n_a (Eq. 3.48) by a dynamic equation for the total number of filaments (attached, detached and capped),

which changes according to

$$\frac{dn}{dt} = k_n n_a(t) - v_g^{max}(t) N_c(l = z, t). \tag{3.66}$$

The total number of filaments increases by nucleation and decreases because capped filaments are eaten by the gel. We only consider capped filaments longer than z that exert force. We assume that capped filaments with length $l = z$ vanish at the rate of gel cross-linking. Their number is determined by Eq. 3.61 for $l(t) = z(t)$.

3.3.4 Stationary approximation

To calculate t_z^* in every time step and integrate over F_d and v_g is computationally very demanding. We also want to avoid tracking the history of l_a, l_d, z, n_a, n_d and n. To simplify the calculation, we assume a stationary distribution $N_c(l)$. In the stationary case, we obtain (see calculation 3.60)

$$\begin{aligned} N_c(l) &= \int_{t^*}^{t} dt' k_c(l_d(t')) n_d(t') \delta(l(t') - l_d(t')) \exp\left(\int_{t'}^{t} \frac{v_g^{max}}{z} dt'' \right) \\ &= -\int_{l_d}^{l} dl' \frac{z}{v_g^{max} l'} k_c n_d \delta(l' - l_d) \frac{l'}{l} = \frac{z k_c n_d}{l v_g^{max}}. \end{aligned} \tag{3.67}$$

We have changed the integration variable according to Eq. 3.56 and used Eq. 3.57 to substitute the exponential function.

The total density of capped filaments that exert force (i.e. with length $z < l < l_d$) reads

$$n_c = \int_z^{l_d} dl N_c(l) = \frac{z k_c n_d}{v_g^{max}} \ln\left(\frac{l_d}{z}\right). \tag{3.68}$$

The cross-linking rate v_g^{max} is itself dependent on $n = n_a + n_d + n_c$. Therefore we have to solve the equation for n_c and find

$$n_c = -\frac{n_a + n_d}{2} + \sqrt{\left(\frac{n_a + n_d}{2.0}\right)^2 + \ln\left(\frac{l_d}{z}\right) \frac{k_c n_d z}{\hat{v}_g^{max}}}. \tag{3.69}$$

Note that $v_g^{max} = \hat{v}_g^{max} n$, appearing in the rate of filament shortening and gel boundary progression, depends on $n = n_a + n_d + n_c$. We use the n_c from Eq. 3.69, although we have neglected capped filaments shorter than z. We have calculated v_g from a reaction-diffusion equation of free and filament-bound cross-linkers (section 3.1.3). It is assumed that filament tips are located at the membrane. Therefore, it is unclear, how very short filaments, that do not span the whole semiflexible region, contribute to the cross-linking rate, which justifies this approximation.

To calculate the mean value of the cross-linking rate, we again only consider capped filaments with $z \leq l \leq l_d$. For those long filaments, we can neglect the length dependence of v_g and set $v_g = v_g^{max}$. For shorter filaments, v_g decreases to zero, and their contribution is therefore small. The average cross-linking velocity of attached, detached

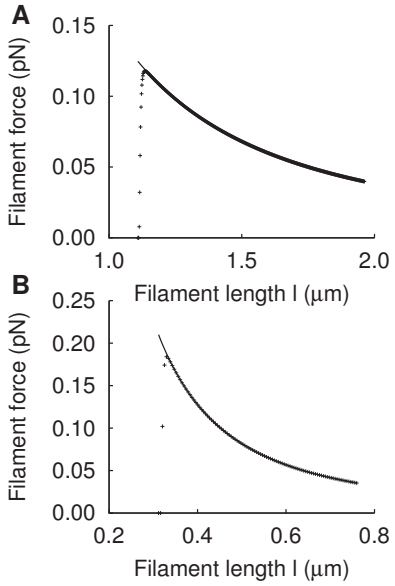

Figure 3.4: Force of capped filaments for $z \leq l \leq l_d$, which occurs in the integrand of equation 3.72, during a simulation of the system. (*Crosses*) Entropic force according to Eq. 3.10. (*Solid line*) Euler buckling force only (Eq. 3.11) with scaling function set to 1 as an approximation for the entropic force to obtain an analytic expression for the total force of capped filaments f_c (Eq. 3.73). Only for lengths slightly larger than l_d the full entropic force differs from the Euler buckling force, so that the approximated f_c is slightly too large. However, the contribution of that part to the integral is very small and the approximation is good. (*A*) $l_p = 15$ μm; (*B*) $l_p = 2$ μm. Other parameters: $k_a = 0.833$/s, $k_d^0 = 1.67$/s, $k_n^0 = 2.0$/s, $k_n^N = 0.00167$ μm/s, $k_c = 1.0$/s, $\hat{v}_g^{max} = 0.01$ μm^2/min, $v_p^{max} = 50$ μm/min, $\kappa = 0.833$ nNs/μm^2, $\bar{l} = 10$, $\eta = 33.3$ nNs/μm^2, $\xi = 10.0$ nNs/μm^3, $\mu = 2.78$ pNs/μm^2, $h_0 = 0.1$ μm, $L = 10$ μm.

and capped filaments reads

$$v_{link} = \frac{1}{n}\left(n_a v_g(l_a) + n_d v_g(l_d) + v_g^c\right), \tag{3.70}$$

with the contribution of capped filaments

$$v_g^c = \int_z^{l_d} v_g(l) N_c(l) dl = z k_c n_d \int_z^{l_d} \frac{v_g(l)}{l v_g^{max}} dl \approx z k_c n_d \int_z^{l_d} \frac{1}{l} dl = z k_c n_d \ln\left(\frac{l_d}{z}\right). \tag{3.71}$$

The force of capped filaments is given by

$$f_c = \int_z^{l_d} dl N_c(l) F_d(l,z) = \frac{k_c n_d z}{v_g^{max}} \int_z^{l_d} \frac{F_d}{l} dl, \tag{3.72}$$

with $F_d(l,z) = \frac{\pi^2}{4}\frac{k_B T l_p}{l^2}\tilde{F}(\tilde{\eta})$ (see Eq. 3.10). The scaling function $\tilde{F}(\tilde{\eta})$ (Eqs. 3.12, 3.13) cannot be integrated analytically. It increases monotonically to 1 with increasing compression $\tilde{\eta}$ of the filament. When simulating the dynamical system, we see that the $1/l^3$-dependence of F_{crit} in the integrand dominates over the increasing part of $\tilde{F}$ (see Fig. 3.4). Therefore we approximate F_d by the Euler buckling force F_{crit} and obtain

$$f_c = \frac{k_c n_d z}{v_g^{max}} \int_z^{l_d} \frac{\pi^2}{4}\frac{k_B T l_p}{l^3} dl = \frac{k_c n_d z}{v_g^{max}} \frac{\pi^2}{8} k_B T l_p \left(\frac{1}{z^2} - \frac{1}{l_d^2}\right). \tag{3.73}$$

3.3.5 Severing

We also want to include the disassembly of actin filaments by ADF/cofilin into our model. ADF/cofilin binds to ADP-Actin within filaments and promotes its dissociation by severing and depolymerization of filaments (Pollard and Borisy [2003]). We hypothesize that filaments to which cofilin is bound vanish from the SR because they cannot exert force any longer, once they are severed. Actin filaments bind ATP-actin monomers at their (+)-ends and quickly hydrolyze ATP to ADP-P_i but it takes longer to loose the y-phosphate. Cofilin only binds to ADP-actin when the y-phosphate has dissociated. We can describe the dissociation by an exponential decay. The half life time $T_{1/2}$ for y-phosphate dissociation within the filament is 6 min (Pollard and Borisy [2003]). We neglect that y-phosphate dissociation is probably accelerated by cofilin. The probability of cofilin binding is proportional to the probability of finding an ADP-actin monomer at a given site x from the tip of the filament

$$p_{ADP} = 1 - \mathrm{e}^{-\ln(2)t/T_{1/2}} = 1 - \mathrm{e}^{-\ln(2)x/(v_p^{max}T_{1/2})}. \tag{3.74}$$

We assume that the polymerization velocity is constant v_p^{max}. The probability of filament severing is found by integrating over the whole filament length

$$k_{sev} = \int_0^l 1 - \mathrm{e}^{-\ln(2)x/(v_p^{max}T_{1/2})}dx = l + \frac{v_p^{max}T_{1/2}}{\ln(2)}\left(\mathrm{e}^{-\frac{l\ln(2)}{v_p^{max}T_{1/2}}} - 1\right). \tag{3.75}$$

That leads to l-dependent terms in the n_d- and n_a-dynamics

$$\dot{n}_d = k_d n_a - (k_a + k_c)n_d - k_{sev}n_d\left[l_d - \frac{v_p^{max}T_{1/2}}{\ln(2)}\left(1 - \mathrm{e}^{-\frac{l_d\ln(2)}{v_p^{max}T_{1/2}}}\right)\right], \tag{3.76}$$

$$\dot{n}_a = k_a n_d - (k_d - k_n)n_a - k_{sev}n_a\left[l_a - \frac{v_p^{max}T_{1/2}}{\ln(2)}\left(1 - \mathrm{e}^{-\frac{l_a\ln(2)}{v_p^{max}T_{1/2}}}\right)\right], \tag{3.77}$$

with the binding rate of cofilin k_{sev}.

3.3.6 Comparison of time-dependent and approximated model

In Fig. 3.5 and Fig. 3.6, we compare the solution of our time-dependent model from section 3.3.3 including severing with the solution with the approximations from section 3.3.4. Those solutions will be discussed further in the following chapter (section 4.2.4 and section 4.3.1). The stationary values are almost indistinguishable, confirming the approximation for the force of capped filaments (Eq. 3.73). During the transient phase, the force of capped filaments is first higher, then lower than in the full model due to the stationary approximation. The transient increase in filament length is smaller with the approximations (Fig. 3.5 *B*), entailing a higher force of attached and detached filaments. Therefore the number and force of capped filaments decreases more quickly afterwards as shorter filaments vanish into the gel more quickly. In conclusion, all main features of the solutions are reproduced with the approximations from section 3.3.4.

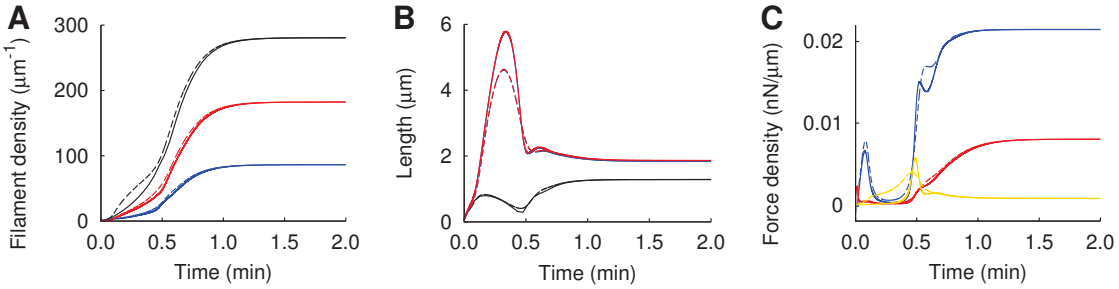

Figure 3.5: Comparison of the solution of the time-dependent model (section 3.3.3, *solid lines*) and the model with the approximations from section 3.3.4 (*dashed lines*) for the parameters from the fit of the force-velocity relation (Fig. 4.15, Table 4.4). (*A*) Density of attached filaments n_a (*blue*), detached filaments n_d (*red*) and the total filament density n (*black*). (*B*) Length of attached filaments l_a (*blue*), of detached filaments l_d (*red*) and SR depth z (*black*). (*C*) Force density of attached filaments f_a (*blue*), of detached filaments f_d (*red*) and capped filaments f_c (*yellow*).

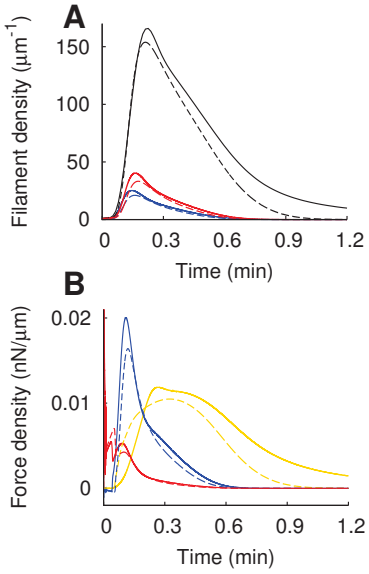

Figure 3.6: Comparison of a solution of the time-dependent model (section 3.3.3, *solid lines*) and approximated model (section 3.3.4, *dashed lines*) for parameters in the excitable regime with $n = 0$ as stationary state. Parameters are the same as in Fig. 4.18, retrograde flow is set to zero. (*A*) Density of attached filaments n_a (*blue*), detached filaments n_d (*red*) and the total filament density n (*black*). (*B*) Force density of attached filaments f_a (*blue*), of detached filaments f_d (*red*) and capped filaments f_c (*yellow*).

4 Modeling results

4.1 General features of the model and stability analysis

In this section we calculate stationary properties of the lamellipodium as a function of model parameters. The existence of a stable fixed point with a filament density $n > 0$ defines the existence of a stable stationarily protruding lamellipodium. The existence of a stable limit cycle corresponds to a stable lamellipodium that shows oscillations of the leading edge. If $n = 0$ is the only stable fixed point, lamellipodia can either only form transiently or not at all. Different sets of parameters describe different cell types, or different levels of expression or activation of signaling molecules within one cell type.

4.1.1 Stationary filament length and density

In Fig. 4.1 *A, B* and Fig. 4.2 *A, B, C*, the stationary filament length and SR depth as a function of the maximum polymerization velocity are shown. We first discuss the results of the model with constant filament density from Fig. 4.1. For low polymerization rates $v_p^{max} < v_g^{max}$, the filaments are relatively short (shorter than 300 nm). Consequently, the effective length-dependent cross-linking rate v_g (Eq. 3.17) is lower than the maximum cross-linking rate v_g^{max} and equals the effective polymerization rate v_p (Eq. 3.16). In the stationary state, the membrane velocity (Fig. 4.1 *C, D*) always equals the effective cross-linking velocity, and the total filament force is proportional to the membrane velocity. Because the leading edge moves slowly, the resulting filament force is weak. However, the single short filaments are stiff and exert relatively high forces. Attached filaments are shorter than the SR depth z and exert a pulling force which is compensated for by the pushing force of detached filaments.

As v_p^{max} increases, filaments get longer. The total filament force has to increase with the increasing velocity, but longer filaments exert weaker forces. In order to be able to exert higher forces, detached and attached filaments start to grow with respect to z and bend. Attached filaments get longer than z and also push the membrane. At a certain length, the cross-linking velocity reaches its maximum value and stays constant. The leading edge velocity stays at the same value since it cannot move faster than the gel boundary. However, when filaments get longer than about 1 µm, they become that floppy that they have to bend strongly to still exert the same force. Also, the rate of filament shortening $\tilde{v}_g = v_g l/z$ has to equal the increasing polymerization rate. Therefore, z decreases. The retrograde flow velocity is always proportional to the total filament force and therefore also proportional to the membrane and cross-linking velocity (Fig. 4.1 *C, D*).

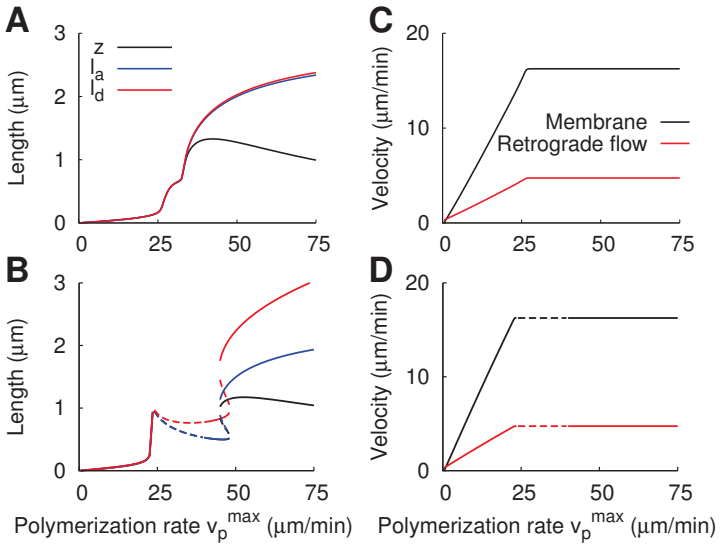

Figure 4.1: Stationary filament length, SR depth, membrane velocity and retrograde flow velocity as a function of the maximum polymerization rate for the model with constant filament density. (*A, B*) Length of attached (*blue*) and detached (*red*) filaments and SR depth (*black*). (*C, D*) Membrane (*black*) and retrograde flow (*red*) velocity. (*A, C*) For the parameters from Table 4.2. (*B, D*) For $k_a = 0.2/\mathrm{s}$ and $k_d^0 = 0.75/\mathrm{s}$, all other parameters unchanged. The *dashed line* indicates that the fixed point becomes unstable and oscillations occur.

For small attachment and detachment rates (Fig. 4.1 *B, D*) we find oscillations at intermediate filament lengths. Attached filaments are still shorter than z. Nevertheless, filaments are long enough that the rate of filament shortening $\tilde{v}_g$ is the maximum cross-linking rate v_g^{max}. At sufficiently strong forces, the effective polymerization velocity v_p still has to be smaller than $\tilde{v}_g$. Then, filaments shorten during a phase of slow movement. The pushing force of detached and pulling force of attached filaments increases until they are sufficiently strong to disrupt the attached filaments from the obstacle and push it forward. The forces relax and filaments grow long again (see Fig. 4.4 and Enculescu et al. [2008] for a detailed description of the oscillation mechanism).

At larger polymerization rates, there is a bistable regime in Fig. 4.1 *B, D*. This is the region where attached filaments become longer than z and their force changes from pulling to pushing. Detached filaments grow longer also, become floppy and exert weaker forces, because the total force does not change and their contribution to it has to decrease. Both stable fixed points exhibit the same velocity but the distribution of forces between attached and detached filaments is different.

For small capping, nucleation and severing rates, the behavior of the model with variable filament density (Fig. 4.2 *A*) is very similar to the model with constant filament density (Fig. 4.1 *A*). However, there is a small bistable regime at relatively low polymerization rates. In the stationary state, the rate of filament shortening has to equal

the effective polymerization rate. In the model with constant filament density, the filament length is small for small polymerization rates in order to achieve a small effective cross-linking rate lower than the maximum cross-linking rate and equal to the small polymerization rate. If capping, nucleation and severing are included, it is also possible that the maximum cross-linking rate decreases by decreasing filament density. Indeed, both stable fixed points in the bistable regime exhibit the same velocity (Fig. 4.2 *G*). However, the filament density is higher and filaments are shorter at one fixed point, filament density is lower and filaments are longer at the other fixed point (Fig. 4.2 *A, D*).

The result for higher capping and nucleation rates (Fig. 4.2 *C*) differs from the result with constant filament density due to the same phenomenon. In Fig. 4.2 *F*, the filament density is very low at low polymerization rates and increases with increasing polymerization rate. Filaments are long at all values of the polymerization rate. The membrane velocity equals the density dependent maximum cross-linking rate in the whole domain (Fig. 4.2 *I*). The number of capped filaments increases with the polymerization rate because the difference between l_d and z increases and it takes longer until capped filaments become shorter than z. As the force of capped filaments increases also, the force of detached filaments decreases and the capping rate increases. The rate of filament severing increases with increasing filament length, too. The number of attached and detached filaments decreases as capping and severing increases and fewer filaments are nucleated from attached filaments. Finally, the fixed point vanishes at $v_p^{max} = 72$ µm/min in Fig. 4.2 *C, F, I*. However, independent of parameter values, there is always a stable fixed point at $n = 0$, which is taken then. This fixed point is essential for the description of transient lamellipodium formation (see section 4.3).

In Fig. 4.3, we examine how the filament density in the model including capping, nucleation and severing changes with the model parameters. Since $n = 0$ means there is no protrusion, the conditions for the existence of attractors with $n > 0$ (fixed points or limit cycles) describe the conditions for the existence of protrusions. In Fig. 4.2 *F*, we already see that, if capping and nucleation rate are not too low, the filament density increases with increasing polymerization rate and reaches a maximum before it drops to zero. The stable fixed point vanishes because the rate of filament nucleation cannot compensate for filament extinction by capping and severing. Hence, it is not surprising that the filament density is zero for low nucleation rates k_n^0 (Fig. 4.3 *A*). It also vanishes for small cross-linking rates $\hat{v}_g^{max}$ since filaments are long. That entails large severing rates and renders filaments floppy which increases the capping rate. Similarly, the filament density decreases with increasing capping rate k_c^{max} (Fig. 4.3 *B*). Larger external force has among others the consequence of decreasing the capping rate via the force dependence of this rate (Fig. 4.3 *B*). Furthermore, filaments shorten to adopt to the external force which decreases the severing rate. In that way, applying an external force may cause protrusion formation in the parameter regime shown in Fig. 4.3 *B*. Nucleation is proportional to the number of attached filaments. Hence, filament binding may cause protrusion generation in Fig. 4.3 *C*.

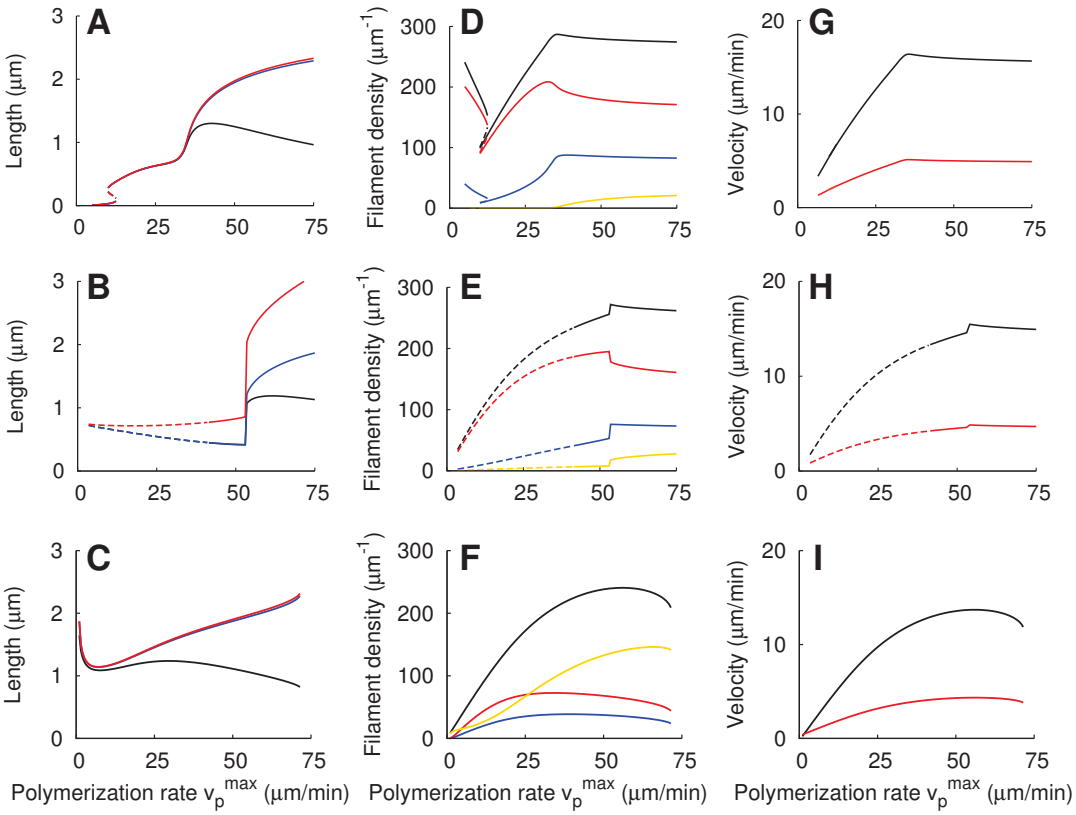

Figure 4.2: Stationary filament length, SR depth, filament density, membrane and retrograde flow velocity as a function of the maximum polymerization rate for the model including capping, nucleation and severing. (*A, B, C*) Length of attached (*blue*) and detached (*red*) filaments and SR depth (*black*). (*D, E, F*) Density of attached (*blue*), detached (*red*) and capped (*yellow*) filaments and total filament density (*black*). (*G, H, I*) Membrane (*black*) and retrograde flow (*red*) velocity. (*A, D, G*) For the parameters from Table 4.4. Between $v_p^{max} = 10$ µm/min and $v_p^{max} = 12.5$ µm/min the system shows bistability. (*B, E, H*) For $k_a = 0.2$/s and $k_d^0 = 0.75$/s, all other parameters like in Table 4.4. (*Dashed line*) Unstable fixed point, the system oscillates. Bistability with different filament lengths, analogous to Fig. 4.1 *B, D*, is not shown in the plot. (*C, F, I*) For $k_n^0 = 2.2$/s and $k_c^{max} = 1.0$/s, all other parameters like in Table 4.4. The displayed fixed point vanishes at $v_p^{max} = 72$ µm/min. However, there is always another stable fixed point at $n = 0$, zero velocity and undetermined filament length.

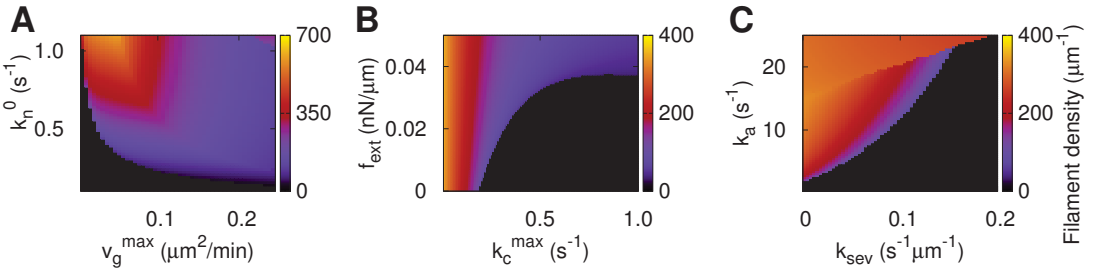

Figure 4.3: Stationary total filament density. (*A*) As a function of cross-linking rate $\hat{v}_g^{max}$ and nucleation rate k_n^0. For large cross-linking and nucleation rates, there is a small bistable domain, like for small polymerization rates in Fig. 4.2 *D*. We only show the fixed point with lower filament density. (*B*) As a function of capping rate k_c^{max} and external force f_{ext}. (*C*) As a function of the binding rate of cofilin k_{sev} and attachment rate k_a. There is a bistable domain at large attachment rates. We only show the fixed point with higher filament density. All other parameters as in Table 4.2.

4.1.2 Oscillations

In Gholami et al. [2008] it was shown that the basic model (Eqs. 3.29, 3.30, 3.31, 3.33) exhibits stationary and oscillatory motion. Those regimes are conserved when retrograde flow (Zimmermann et al. [2010]) and capping and nucleation (Faber et al. [2010]) are included.

In Fig. 4.4, we show two examples for oscillatory solutions of the model including capping, nucleation and severing. The oscillations can look rather differently for different parameters. The membrane velocity can either stay at an intermediate value most of the time and periodically drop to lower values during short "stops" (Fig. 4.4 *F*), or the membrane periodically jerks forward during short "jumps" (Fig. 4.4 *E*), depending on the value of v_p^{max}. The "spikes" in the velocities arise from small discontinuities in the position time courses and their numerical differentiation. Usually, measured data is smoother and therefore they will most likely not be found in experiments. The amplitude of the filament density can vary significantly: the density changes by about 30 /µm in Fig. 4.4 *A* and by about 100 /µm in Fig. 4.4 *B*. New filaments are nucleated from attached filaments in our model. Due to nucleation, the total filament density increases when filament forces are low and the number of attached filaments goes up. The number of capped filaments increases also, because the capping rate is higher at lower forces, and filaments are long and it takes longer until they vanish into the gel. Since the capping rate is very small in Fig. 4.4 *B*, there are almost no capped filaments, in contrast to Fig. 4.4 *A* where the number of capped filaments increases periodically with the total filament density. The retrograde flow increases or decreases with the leading edge velocity since both are proportional to the filament force (Fig. 4.4 *E, F*).

Many mathematical models equate the leading edge velocity with the polymerization rate or a monotonously increasing algebraic function of it. That excludes a phase difference between the maxima of polymerization rate and leading edge velocity in os-

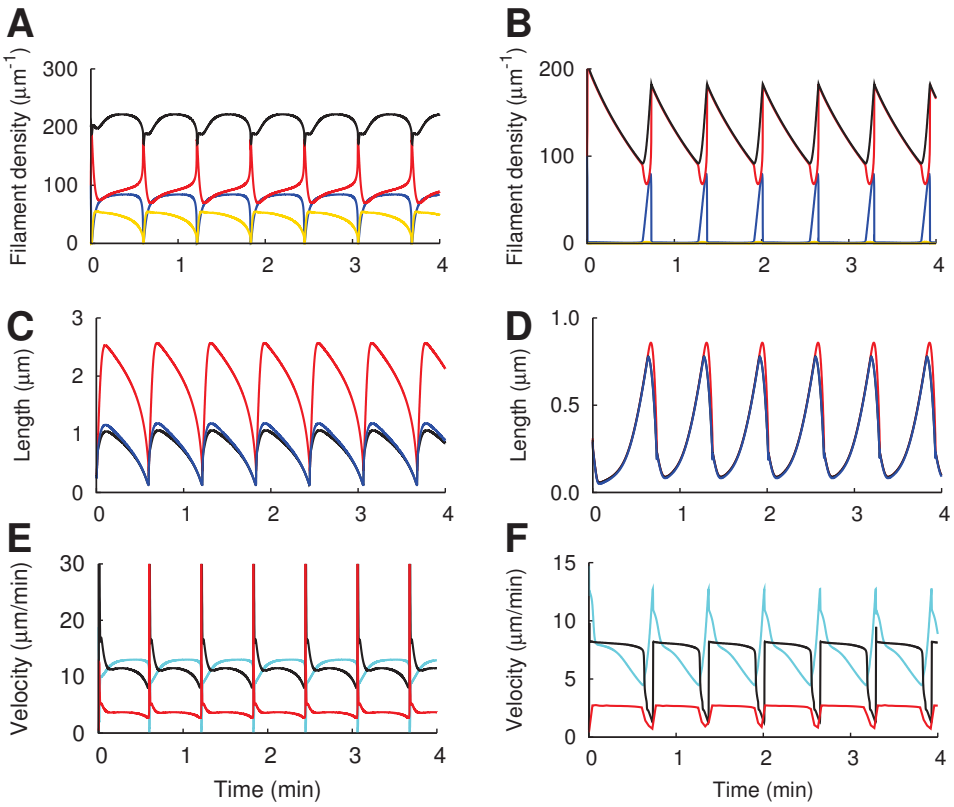

Figure 4.4: Examples for oscillatory solutions of the model including capping, nucleation and severing. (*A, B*) Density of attached (*blue*), detached (*red*) and capped (*yellow*) filaments, and total filament density (*black*). (*C, D*) Length of attached (*blue*) and detached (*red*) filaments and SR depth (*black*). (*E, F*) Membrane velocity (*black*), retrograde flow velocity (*red*) and velocity of the gel boundary (*light blue*). (*A, C, E*) For $k_a = 0.2/\text{s}$, $k_d^0 = 0.5/\text{s}$, $k_c^{max} = 0.2/\text{s}$, $v_p^{max} = 72$ µm/min. (*B, D, F*) For $k_a = 0.2/\text{s}$, $k_d^0 = 0.3/\text{s}$, $k_c^{max} = 0.025/\text{s}$, $v_p^{max} = 12$ µm/min. All other parameters like in Table 4.4.

cillations. However, such a phase difference has been observed in experiments (Ji et al. [2008]). The leading edge velocity increases first and subsequently the polymerization rate. Fig. 4.5 shows the two oscillation types as limit cycles in the phase plane spanned by polymerization velocity v_p and leading edge velocity. The system cycles clockwise in both cases. The red limit cycle corresponds to the oscillation shown in Fig. 4.4 *A, C, E*, the blue one to Fig. 4.4 *B, D, F*. There is a clear phase difference between the maxima of both velocities in the red limit cycle. It is about 9 s expressed in time. That is less than the 20 s observed by Ji et al. [2008], but the time lag could still be larger for other parameters in our model. The blue limit cycle exhibits almost no phase difference between the two maxima, but the leading edge velocity decreases earlier than the polymerization rate.

Another example for an oscillatory solution is discussed in section 4.3.2.

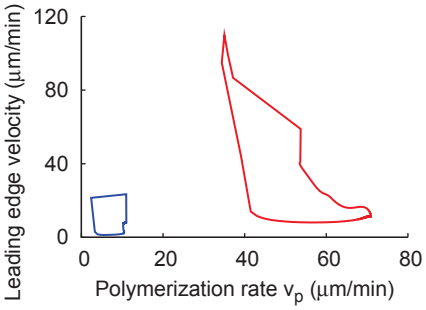

Figure 4.5: The two oscillation types as limit cycles in the phase plane spanned by polymerization velocity v_p and leading edge velocity. The system cycles clockwise in both cases. The red limit cycle corresponds to oscillations shown in Fig. 4.4 *A, C, E*, the blue one to Fig. 4.4 *B, D, F*.

4.1.3 Stationary force-velocity relation

In Fig. 4.6, the stationary membrane velocity and SR properties as a function of an external force applied to the membrane are shown. For the parameters from a fit of experimental data of keratocytes (section 4.2, Table 4.4), hence low capping and nucleation rates, the stationary force-velocity relation is almost linear (Fig. 4.6 *A*), reflecting the force-velocity relation of the gel boundary at constant cross-linking rate. The velocity decreases with increasing external force because the gel is pushed backwards and retrograde flow increases. Hence, the force exerted by the lamellipodium equals the force required to drive retrograde flow against the variety of viscous resistances to it. The slight change in slope occurs because the filament density, and therefore also the maximum cross-linking rate, first increases and then decreases (Fig. 4.6 *C*). Filaments in the SR shorten to balance the increasing external force (Fig. 4.6 *E*). However, they remain long enough that the effective cross-linking rate does not drop below its maximum value. If we increase capping and nucleation rates, the maximum in the filament density is more pronounced (Fig. 4.6 *D*). Consequently, the stationary force-velocity relation clearly has a concave shape (Fig. 4.6 *B*). The velocity first increases with increasing force, reaches a maximum and then drops.

The stationary force-velocity relation of the model with constant filament density is linear for the parameters from table 4.2. Yet, if the retrograde flow is slower because gel viscosity and adhesion are higher, the constant model can exhibit an increase in slope

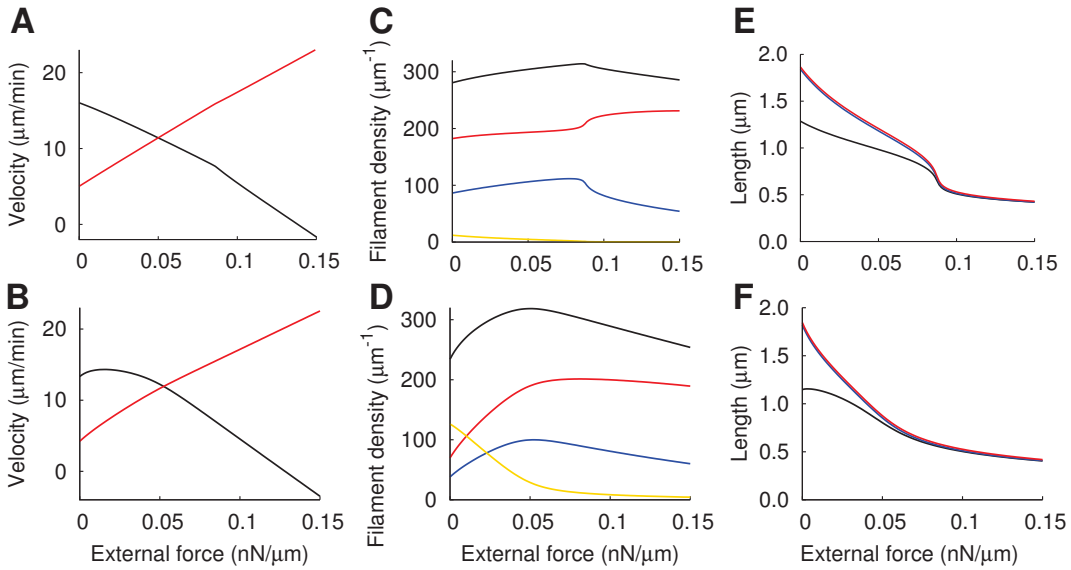

Figure 4.6: Stationary force-velocity relation and retrograde flow, filament density, filament length and SR depth as a function of the external force for the model including capping, nucleation and severing. (*A, B*) Membrane (*black*) and retrograde flow (*red*) velocity. (*C, D*) Density of attached (*blue*), detached (*red*) and capped (*yellow*) filaments and total filament density (*black*). (*E, F*) Length of attached (*blue*) and detached (*red*) filaments and SR depth (*black*). (*A, C, E*) For the parameters from Table 4.4. (*B, D, F*) For $k_n^0 = 2.2/\text{s}$ and $k_c^{max} = 1.0/\text{s}$, all other parameters unchanged.

also (see Fig. 4.7). At small external forces, filaments are long and the cross-linking rate is at its maximum value. They shorten to balance the increasing force and if the length reaches a critical value, the effective cross-linking rate decreases (see also Zimmermann et al. [2010]). Consequently, leading edge motion is slowed down not only by increasing retrograde flow but also by diminished cross-linking.

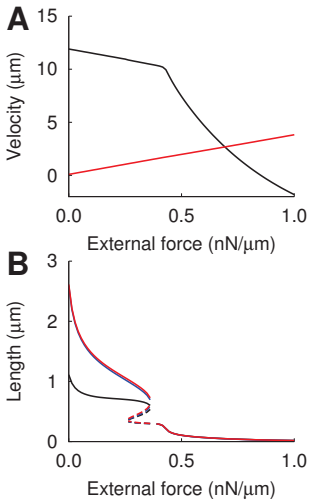

Figure 4.7: Stationary force-velocity relation and retrograde flow, filament length and SR depth as a function of the external force for the model with constant filament density. (*A*) Membrane (*black*) and retrograde flow (*red*) velocity. (*B*) Length of attached (*blue*) and detached (*red*) filaments and SR depth (*black*). Parameters are $\eta = 50$ nNs/µm^2, $\xi = 5$ nNs/µm^3 and $n\hat{v}_g^{max} = 12$ µm/min, all other parameters like in Table 4.2. Since the resistance of the gel is high, the external force induces a shortening of the filaments below the critical length for cross-linking before retrograde flow compensates for forward motion.

4.2 The force-velocity relation

The stationary force-velocity relation calculated in Fig. 4.6 cannot account for the experimentally measured force-velocity relation of keratocytes. Cells crawl towards the cantilever of a scanning force microscope (SFM) and the deflection is measured when the leading edge hits the cantilever (see section 2.6, Fig. 2.2 for description of experimental setup). In this section, the model is applied to dynamically simulate and explain the keratocyte measurements. The time from first cantilever contact until stalling is between 5 s and 10 s. It is unlikely that the filament density changes substantially during such a short time. Consequently, we use the model with constant filament density. We justify that approximation with the complete model in section 4.2.4. Most of the results (figures, tables and text) have been published in Zimmermann et al. [2012].

4.2.1 Simulating the SFM-cantilever experiment

To model the cantilever experiment we split the equation for the z-dynamics 3.41 into the dynamics of the gel boundary position y_g and the leading edge position y. At position y_0, the lamellipodium touches the cantilever and subsequently pushes against the cantilever. Hence, the external force is proportional to the deflection of the cantilever that equals

the leading edge position $y - y_0$. We now solve

$$\dot{y} = [n_a(t)F_a(l_a, z) + n_d(t)F_d(l_d, z) - k \cdot (y - y_0)]/\kappa, \tag{4.1}$$

$$\dot{y}_g = u(v_{link}, f_0), \tag{4.2}$$

using the same equations 3.39 and 3.40 for f_0 and v_{link}. The elastic modulus of the SFM-cantilever k is zero before cantilever contact.

The solutions of the model were fitted by eye to the measurements. We only change the parameters shown in Table 4.3 to account for cell variability and drug effects. All other parameter values are either determined by the experimental setup, taken from the literature whenever available, or fitted once and then kept fixed (see Table 4.2). The effects of changing some important parameters corresponding to a variety of experiments are described in section 4.2.3. The velocity of each cell before cantilever contact was obtained from movies. Moreover, feature tracking analysis was used to measure the retrograde flow in some cells during unhindered motion (see section 2.6, Zimmermann et al. [2012]). Simulations start with parameter values that reproduce the velocity of the individual free running cell and the experiment specific population average of the retrograde flow (Table 4.1). Velocity and retrograde flow fix the value of the model's maximum cross-linking rate, since it has to be equal to the sum of both during free steady motion. Gel viscosity, friction and contractile stress determine the retrograde flow velocity. Those parameters, as well as the filament density and polymerization rate, also affect the other phases of the force-velocity relation and are determined by fitting the cantilever deflection through all three of them (Fig. 4.8).

	Control measured simulated	CD measured simulated	ML-7 measured simulated
velocity of unhindered	14.4 ± 2.8	5.9 ± 3.2	7.6 ± 2.6
cell (μm/min)	14.0 ± 2.8	5.6 ± 2.8	7.7 ± 2.7
retrograde flow velocity of	4.1 ± 1.8	1.63 ± 0.66	2.49 ± 0.72
unhindered cell (μm/min)	4.3 ± 2.1	2.1 ± 1.6	1.68 ± 0.53

Table 4.1: Measured and simulated velocities before cantilever contact for control and application of cytochalasin D (CD) and ML-7. Table published in Zimmermann et al. [2012].

4.2.2 Adaptation of the cytoskeletal structure to the external force during the different phases of the force-velocity relation

Initial velocity drop

Upon first contact with the cantilever, the leading edge velocity drops from about 260 nm/s to less than 0.1 nm/s both in experiments and simulations (Fig. 4.8 *D*). The velocity drop is the difference between the free cell velocity and the first detectable

Symbol	Meaning	Control CD ML-7	Units	Reference
n	total filament density	300 230 300	μm^{-1}	Abraham et al. [1999]
k_a	attachment rate of filaments to membrane	10.0	s^{-1}	10/s in Shaevitz and Fletcher [2007]
k_d^0	detachment constant	25.0	s^{-1}	fitted
v_p^{max}	saturation value of polymerization velocity	41.5	µm/min	30 µm/min in Mogilner and Oster [2003]
$n\hat{v}_g^{max}$	saturation value of gel cross-linking rate	21.0 8.0 9.5	µm/min	fitted
$\bar{l}/n$	saturation length of cross-linking rate	0.1	µm	assumed
κ	drag coefficient of plasma membrane	0.113	nN s/μm^2	Berg [1983]
k	elastic modulus of AFM cantilever	291 148 348	nN/μm^2	as in experiments
d	actin monomer radius	2.7	nm	Mogilner [2009]
l_p	persistence length of actin	15	µm	Le Goff et al. [2002]
k_l	spring constant of linker protein	1	nN/µm	Mogilner and Oster [2003], Evans [2001]
η	viscosity of actin gel	0.833 0.5 0.783	nN s/μm^2	Bausch et al. [1998], Yanai et al. [2004]
ξ	friction coefficient of actin gel to adhesion sites	0.2	nN s/μm^3	Doyle et al. [2004]
μ	active contractile stress in actin gel	8.33 8.33 0	pN/μm^2	fitted [a]
h_0	height of lamellipodium at leading edge	0.25	µm	Anderson et al. [1996], Brunner et al. [2006]
L	length of gel part of lamellipodium	10	µm	Svitkina et al. [1997], Brunner et al. [2006]
	contact length with bead	4.4	µm	as in experiments

[a] μ was chosen to be very small compared to F/h, according to experimental findings that contraction is negligible in the fish keratocyte central lamellipodium

Table 4.2: List of model parameters and their values in Fig. 4.8. Table published in Zimmermann et al. [2012].

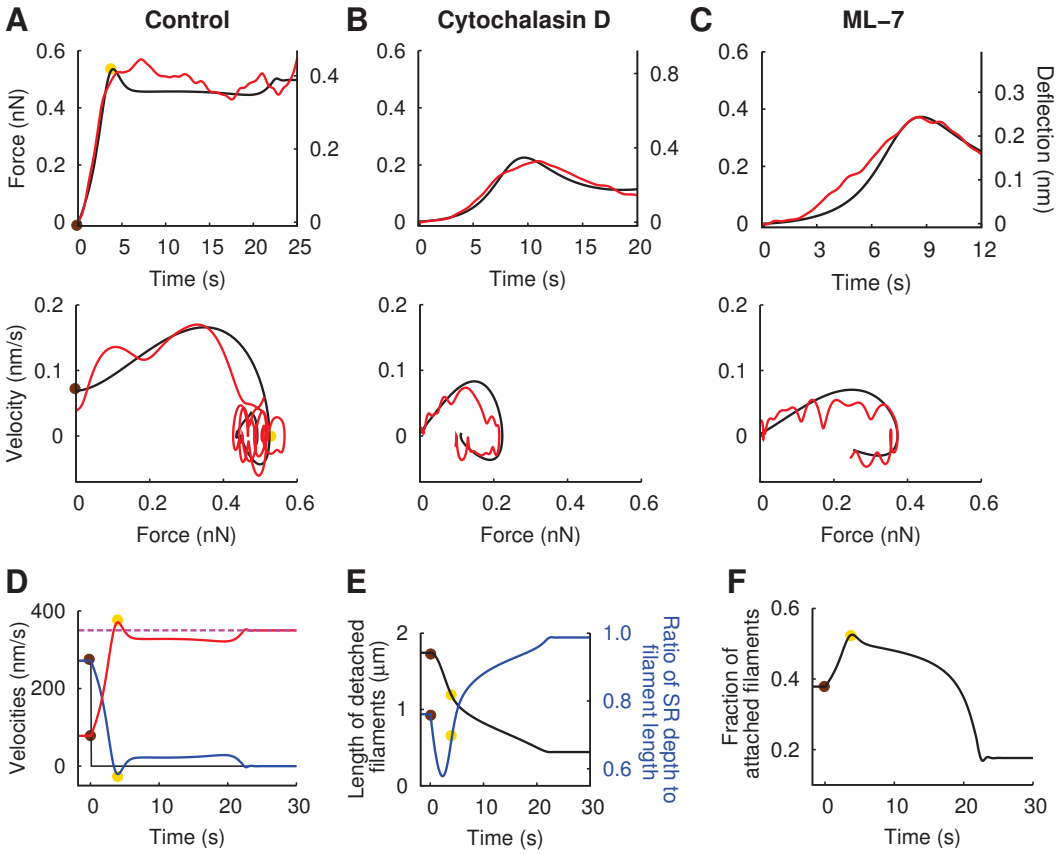

Figure 4.8: Cantilever deflections, force-velocity relations, and SR properties. (*A-C*) Comparison of simulations (*black*) and experiments (*red*) for (*A*) a control cell and cells influenced by the application of (*B*) cytochalasin D and (*C*) ML-7. (*Upper row*) Time-course of the cantilever deflection due to the lamellipodium's leading edge pushing against the bead on the cantilever; (*lower row*) force-velocity relation. (*D-F*) Simulated development of velocities and the semiflexible region (SR) after cantilever contact for the control cell. (*Brown dots*) first cantilever contact; (*yellow dots*) time when motion stalls. (*D*) Development of the leading edge velocity (*black*), the gel boundary velocity (*blue*), retrograde flow velocity (*red*) and the sum of the gel boundary and retrograde flow velocities (*dashed magenta*), which is essentially constant. (*E*) Time course of the ratio of SR depth to length of detached filaments (*blue*) and the filament length (*black*). The differential stiffness of the filaments is proportional to (free filament length)$^{-4}$ (Eq. 3.11). (*F*) Time course of the fraction of filaments attached to the membrane. Parameter values for simulations are given in Table 4.2. Figure published in Zimmermann et al. [2012].

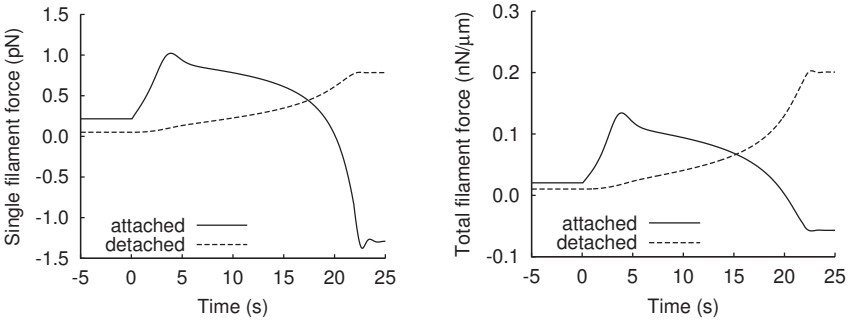

Figure 4.9: Simulation results for single filament forces and for the total forces of all attached and detached filaments for control (see Fig. 4.8). Forces with a positive value push the leading edge membrane. Figure published in Zimmermann et al. [2012].

cantilever deflection velocity. The ensuing slow cell motion causes the force-velocity relations shown in Fig. 4.8, *A*-*C*.

The boundary between the SR and gel decelerates slowly, but the initial leading edge velocity drop appears to be instantaneous (Fig. 4.8 *D*), and simulations suggest that it occurs within a few milliseconds. The forces causing this abrupt leading edge deceleration are in the range of the zero point fluctuations of the cantilever of 0.05 nN. The model explains the sensitive response of the leading edge to these minute forces by the rather long free polymer length in the SR. Fits of the model to measurements result in a filament length of the freely running cell of about 1.8 µm (Fig. 4.8 *E*). Such long filaments easily bend elastically (Eq. 3.11).

For given maximum cross-linking and polymerization rates, the free filament length is determined by the force per filament, which in turn depends on filament density. Small force per filament entails long free length. We will see in the next section, how the free filament length adapts to force changes. The free filament length also crucially affects the time course of the concave phase, in particular the time until stalling. Hence, the fitting procedure results in a filament density value (and polymerization rate) providing for a force per filament and free filament length in the freely running cell which explains the sensitive initial response and is compatible with the time course of the concave phase.

Concave phase: retrograde flow accelerates

The concave phase follows the initial velocity drop. It lasts until the first force maximum of the deflection curve, where the stall force is reached (indicated by a yellow dot in Fig. 4.8 *A*). The leading edge velocity increases slightly in the beginning, then it decreases and lamellipodium motion stalls. The leading edge velocity is small initially, since filaments are long and the SR is soft. Long filaments cannot transmit the external force to the gel effectively. Thus, the gel keeps moving forward, the SR depth shrinks and filaments bend (Fig. 4.8 *E*). Bent filaments are cross-linked into the gel more quickly as the SR depth decreases. They shorten and become stiffer, which enables them to transmit larger forces

without further bending, to straighten out and to cause the slight velocity increase.

Since the external opposing force prevents forward protrusion, the ongoing polymerization pressure pushes the actin gel rearward. Retrograde flow accelerates during the entire concave phase (see Fig. 4.8 *D*), as the force transmitted by the filaments in the SR increases with increasing stiffness. The external force shifts the partitioning of the polymerization velocity between forward protrusion and retrograde flow towards retrograde flow. The cell slows down as retrograde flow speeds up (Fig. 4.8 *D*). Cell motion stalls when all polymerization velocity is converted into retrograde flow, in agreement with experimental reports showing the sum of protrusion velocity and retrograde flow to be approximately constant (Vallotton et al. [2005]).

The polymerization rate decreases exponentially with increasing force. Nevertheless, forces per detached filament stay below 1 pN (Fig. 4.9), which is the single filament polymerization stall force (Mogilner and Oster [1996], Footer et al. [2007]). Therefore, a reduction of the polymerization rate by the load per filament is not the crucial factor in cell deceleration. It is not the force-dependence of polymerization that shapes the force-velocity curve of the lamellipodium, but the interplay between filament shortening and bending in the SR and gel retrograde flow. Since the actin filaments continue to polymerize, retrograde flow is fast in the stalled state, and the polymerization force that pushes retrograde flow balances the external force when the leading edge stalls.

The magnitude of the stall force is determined by the maximum polymerization rate and gel properties like viscosity and adhesion. The polymerization rate influences also the free filament length. The time to reach the stall force increases with increasing filament density because the force per filament decreases, filaments are longer and it takes longer to shorten them.

Adaptation to the stalled state

When the first maximum of the deflection is reached (yellow dot in Fig. 4.8 *A*), the lamellipodium has not adapted to the larger external force yet. The ensuing adaptation to the stalled state causes a third phase of the force-velocity relation, which starts with a slight leading edge retraction followed by irregular and transient oscillations with decreasing amplitude around the stall force. The durations and time courses of the transients are not generalizable and vary between cells, comprising anything between several undulations of force and velocity and a single incomplete one. However, the existence of an adaptation phase is a universal feature of the force-velocity curve, and has been observed in all simulations and experiments. Adaptation demonstrates that the force-velocity relation is a dynamic phenomenon. It does not describe the stationary velocity of the lamellipodium for a given force.

During the adaptation phase, the depth of the SR shrinks and filaments in the SR straighten further (Fig. 4.8 *E*). The detachment rate of bound filaments increases exponentially with the pulling force (Eq. 3.15) . Therefore, while the fraction of attached filaments increases during the second phase due to the increasing external pushing force, during the third phase it decreases to the value in the stalled state (Fig. 4.8 *F*).

Verifying the mechanism: application of drugs

The mechanism is confirmed by the predictions of the model for the keratocytes' force-velocity relation, when the behavior of cytoskeletal proteins is modulated by drugs (see Fig. 4.10). We compare model predictions with experiments in two steps. We first fit the model to the individual measurements as described above. Then we assess whether significant changes of parameter values of drug treated cells with respect to control cells are in line with the generally established knowledge about the action of the drug. We find that only the values of those parameters change significantly, which reflect the action of the drugs (Table 4.3). All the other model parameters vary within a reasonable range, but are not significantly different between control and drug applications.

Cytochalasin D caps barbed filament ends thus terminating their polymerization (May et al. [1998]). Consequently, it reduces the density of filaments, and also the cross-linking rate. Fits of the model to eight cells demonstrate that only the parameter values of filament density (Student's t-test $p = 7 \cdot 10^{-7}$) and cross-linking rate ($p = 8 \cdot 10^{-5}$) decrease significantly relative to control samples upon Cytochalasin D application (Table 4.3). As a consequence, Cytochalasin D reduces the velocity of an unhindered cell (Table 4.1) and delays stalling by the cantilever (Fig. 4.8 *B*). Additionally, the stall force is about one third of the control value. All these properties are found in experiments and simulations.

Myosin can contract the actin gel. However, myosin contraction does not contribute significantly to centripetal actin network flow in the central lamellipodium of fish keratocytes. Accordingly, fits of the model to control experiments resulted in a small value of the contractility parameter. Myosin motors act also as cross-linkers. Fitting the model to seven cells shows that the effect of inhibiting myosin by ML-7 (Bain et al. [2003]) can be well described by a reduction of the cross-linking rate ($p = 7 \cdot 10^{-5}$) and vanishing gel contraction (Table 4.3). ML-7 also delays stalling by the cantilever, but the average stall force does not change with respect to controls (Fig. 4.8 *C*). The quantitative agreement between experiments and simulations suggests that the protrusion mechanisms are accurately reproduced by our model.

4.2.3 Varying parameters: different conditions and scenarios

The effect of varying the cross-linking rate and filament density on the stall force is shown in Fig. 4.10. Here, we change other model parameters to discuss possible mechanisms, different experimental conditions and experiments from another lab.

Cantilever stiffness

The velocity dropped less in experiments by the Radmacher lab (to about 20 nm/s, see Prass et al. [2006]), than in our experiments (to about 0.1 nm/s, see Fig. 4.8). Accordingly, velocities in the concave phase were also larger in their experiments than in ours. The major difference between the experiments was the force constant of the cantilevers; Prass et al. used a much softer cantilever (force constant 1.4 $\mathrm{nN}/\mu\mathrm{m}^2$) than we did (290 $\mathrm{nN}/\mu\mathrm{m}^2$). Simulations show that the velocities in the concave phase are inversely proportional to the force constant (Fig. 4.11), which explains the different measured

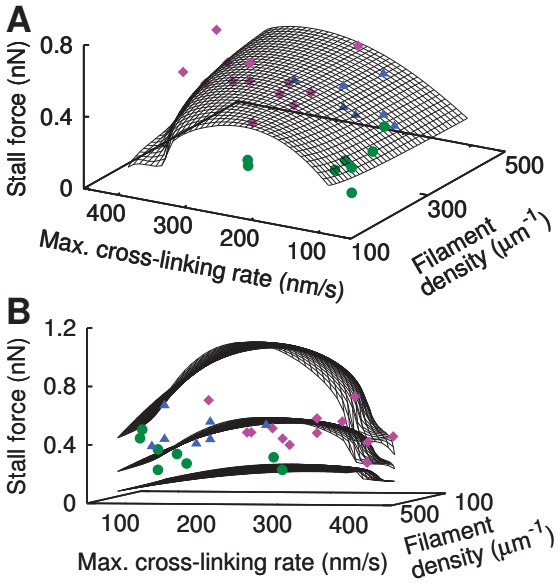

Figure 4.10: Dependence of the stall force on maximum cross-linking rate and filament density. (*A*) (*Black surface*) Prediction of the mathematical model for the control parameter values from Table 4.2. (*Dots*) Results for cross-linking rate and filament density from fits of the model to measurements like those shown in Fig. 4.8 (*magenta rectangles*, control; *green circles*, CD; *blue triangles*, ML-7). (*B*) The same data from a different angle of view showing the scatter of experimental data more clearly. The two additional surfaces demonstrate that all measured stall forces can be explained by the model within a realistic parameter value range for such parameters as cross-linking rate, filament density, the friction coefficient modeling adhesion and viscosity of the actin gel (see Table 4.2 and Table 4.3 for parameter values). Figure published in Zimmermann et al. [2012]

Parameter	Control	CD	ML-7	Surfaces Fig. 4.10	Units
n	302 ± 42	181 ± 32	300 ± 0	variable	μm^{-1}
v_p^{max}	37 ± 12	35.3 ± 4.8	36.8 ± 6.4	37.0	$\mu m/min$
v_g^{max}	18.4 ± 4.5	7.7 ± 4.4	9.4 ± 3.1	variable	$\mu m/min$
η	0.91 ± 0.38	0.90 ± 0.37	1.03 ± 0.17	0.5, 0.833, 1.33	nN s/μm^2
ξ	0.23 ± 0.12	0.22 ± 0.11	0.243 ± 0.053	0.1, 0.233, 0.4	nN s/μm^3
μ	8.33	8.33	0	8.33	pN/μm^2

Table 4.3: List of parameter values (mean ± standard deviation) from fitting several experimentally measured deflection curves (control $N = 13$, CD $N = 8$, ML-7 $N = 7$). Results of all simulations are shown in Fig. 4.10. Parameter values for the surfaces shown in Fig. 4.10 are given in the fifth column (smaller values of η and ξ correspond to *lower surface* in Fig. 4.10 *B*, higher values to *upper surface*). All other parameters are listed in Table 4.2. Table published in Zimmermann et al. [2012].

velocities. The good agreement of the simulations with both sets of experimental results (Fig. 4.11) shows that the force-velocity curve and the magnitude of the velocity drop depend on the stiffness of the cantilever, and that simply the different values of the cantilever force constants explain the differences between studies. The stall force, however, does not depend on cantilever stiffness, which confirms that it is an intrinsic lamellipodium property.

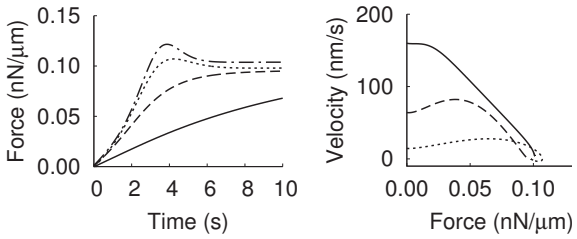

Figure 4.11: Simulated force-velocity curves for different force constants k of the SFM-cantilever. Cantilever force time courses and the corresponding force-velocity relations are shown. Smaller cantilever force constants result in larger deflections for a given force, and larger velocities in the force-velocity relation. (*Dashed-dotted curve*) $k = 290$ nN/µm^2 (force constant used in our study, see also Fig. 4.8); (*dotted curve*) $k = 1.4$ nN/µm^2 (force constant used in the study by Prass et al. [2006]); (*dashed curve*) $k = 0.28$ nN/µm^2; (*solid curve*) $k = 0.056$ nN/µm^2. Simulations also show that the velocities in the concave phase are approximately proportional to $1/k$, aside from the softest cantilever. All other parameter values as in Table 4.2, control. Figure published in Zimmermann et al. [2012].

Persistence length of actin

In Fig. 4.12 a simulation of the control experiment from Fig. 4.8 with a smaller persistence length is shown (7.5 µm instead of 15 µm). Simulations yield shorter filaments. With a smaller persistence length, filaments exert smaller forces. Since the stall force does not change, this has to be compensated for by shorter filaments. The length changes approximately with the square root of the persistence length as suggested by the force scale Eq. 3.11 (see Fig. 4.12 *C*). In the example of Fig. 4.12, we also changed v_p^{max}, which influences the filament length as well, to fit the experimental data. Hence, the scaling behavior is not found exactly.

One has to note, that with the smaller persistence length, also the difference in filament length between the freely running cell and the stalled is smaller (Fig 4.12 *C*). Therefore it takes less time to shorten filaments and the stall force is reached quicker. To still fit the time to reach the stall force given by the experimental data, that was partly compensated by a slower rate of cross-linking (18 µm/min instead of 21 µm/min). Then, also the retrograde flow had to be lower, to meet the measured velocity of the freely running cell, given by the difference of gel cross-linking rate and retrograde flow. A slower retrograde

flow is achieved by a lower drag coefficient of the plasma membrane κ and a higher gel viscosity η.

In conclusion, one can say that with increasing filament stiffness, i.e. increasing persistence length, the stall force does not change but the filament length increases like the square root of the persistence length. It takes longer to reach the stall force, i.e. the velocity in the force-velocity relation decreases. In principle, there is no upper limit for the persistence length in our model and we can still calculate a force-velocity relation with very stiff filaments, though they become unrealistically long.

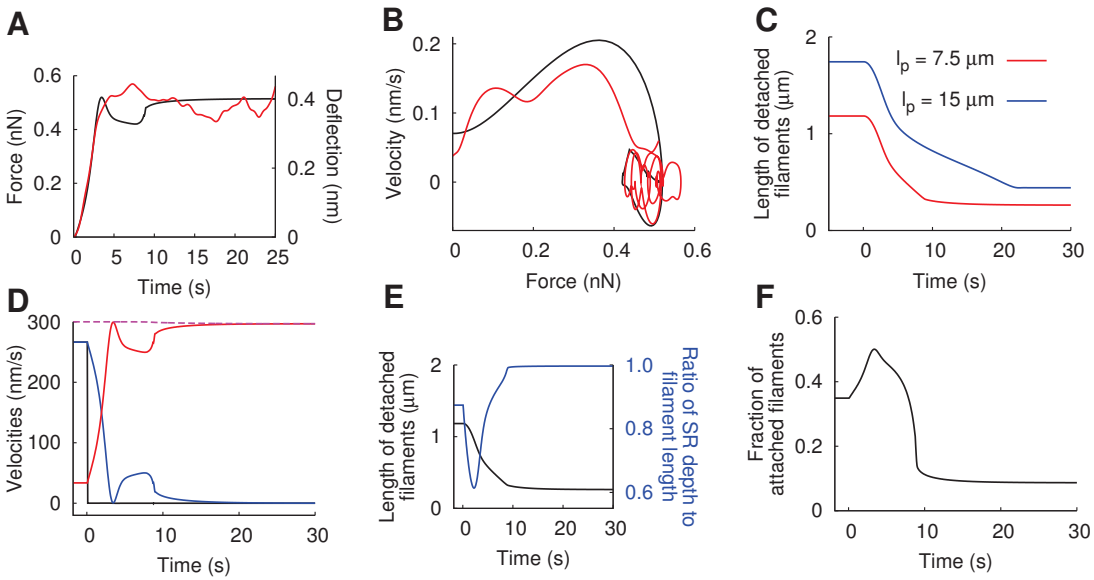

Figure 4.12: Simulation with a value of the persistence length of 7.5 µm instead of 15 µm. (*A, B*) Comparison of simulation (*black*) and control experiment (*red*). (*A*) Time-course of the cantilever deflection, which is proportional to the force exerted on the cell. (*B*) Force-velocity relation obtained from the deflection and deflection velocity. (*C*) Comparison of the time course of the free length of detached filaments for the two different values of the persistence length l_p. The ratio of the free polymer lengths of the freely running cell and after stalling is a little less than the square root of the ratio of persistence lengths, which is the value suggested by the force scaling function (Eq. 3.11). (*D-F*) Simulated development of velocities and the semiflexible region (SR) after cantilever contact. (*D*) Development of the leading edge velocity (*black*), the gel boundary velocity (*blue*), retrograde flow velocity (*red*) and the sum of the latter two (*dashed magenta*). (*E*) Time course of the ratio of SR depth to length of detached filaments (*blue*) and the filament length (*black*). (*F*) Time course of the fraction of filaments attached to the membrane. Parameter values are: $\kappa = 0.0567$ nNs/µm^2, $v_g^{max} = 18$ µm/min, $v_p^{max} = 30$ µm/min, $\eta = 1$ nN/µm^2, $\mu = 0.278$pN/µm^2, all other values like in Table 4.2, control. Figure published in Zimmermann et al. [2012].

Force-dependent gel friction: catch bonds

We tested, whether a force-dependent friction coefficient changes our results. Thus we again fitted our experimental data, this time with a friction coefficient

$$\xi = \xi_0 + a f_0. \tag{4.3}$$

It increases with the force f_0 exerted by attached and detached filaments. This scenario corresponds to increasing adhesion via catch bonds that strengthen when a mechanical pulling force is exerted.

At the stall force, the friction is strong compared to the simulation without catch bonds. Larger ξ entails a higher stall force in our model. To compensate for that, in the simulation with catch bonds shown in Fig. 4.13, the gel viscosity η, which has a similar effect on the stall force, was chosen relatively low. Stall force, time to reach the stall force and retrograde flow are also influenced by the friction coefficient of the plasma membrane κ, which was altered in the example to fit the experimental results.

The model with force-dependent friction can be fitted to the measurement rather well. Hence, we cannot exclude the mechanism of catch bonds, but our simulations suggest that it does not play an essential role for the force-velocity relation.

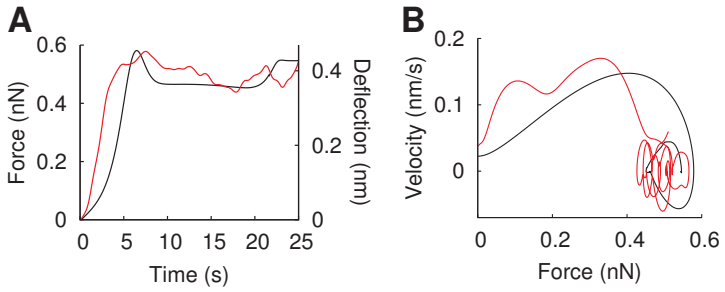

Figure 4.13: Simulation with a force-dependent friction coefficient of the actin gel to the substrate. Comparison of a simulation (*black*) and a control experiment (*red*). (*A*) Time-course of the cantilever deflection, which is proportional to the force exerted on the cell. (*B*) Force-velocity relation obtained from the deflection and deflection velocity. The linear feedback (coefficient $a = 6$ s/µm^2) increases the effective friction from 0.13 nNs/µm^3 in the freely running cell to 0.93 nNs/µm^3 at stall force. The model still reproduces the experimental results rather well. Parameter values are: $\xi_0 = 0.00054$ nNs/µm^3, $\kappa = 0.0533$ nNs/µm^2, $v_g^{max} = 22$ µm/min, $\eta = 0.15$ nN/µm^2, $\mu = 0.278$pN/µm^2, all other values like in Table 4.2, control. Figure published in Zimmermann et al. [2012].

Repeated experiments

Heinemann et al. [2011] retracted the cantilever and repeated their measurement at the same leading edge position with a time lag of about 30 s. Three consecutive measurements of the cantilever deflection gave the same result. In contrast to that, measurements

of the growth velocity of an actin network with an AFM-cantilever showed that the velocity was larger during a second measurement after retraction (Parekh et al. [2005]). That was accounted for by an adaptation of the filament density to force.

The time scales of our simulations are in agreement with the results from Heinemann et al. [2011]. If we "retract" the cantilever at the maximum of deflection (stall force), the result of the repeated simulation after 21 s is the same because the short pause is sufficient for all variables, like filament length and density of attached filaments, to relax to their steady state values. The simulation is shown in Fig. 4.14.

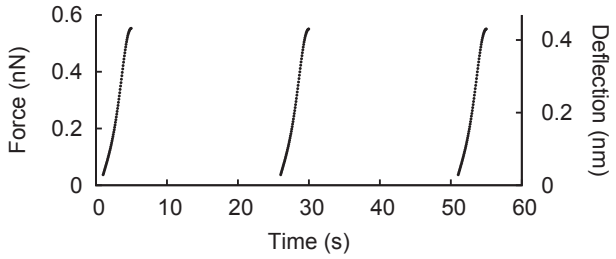

Figure 4.14: Simulation of repeated experiments. The cantilever is retracted at the maximum of deflection which corresponds to the stall force. After a time lag of 21 s, the cell is thought to touch the cantilever again and the experiment is repeated. The time lag is sufficient for the variables to relax to their steady state values so that the first, second and third simulation show the same results. Parameters are as for control in Table 4.2.

4.2.4 Including capping, nucleation and severing

Fit of experimental data

We fitted our model including the processes of capping, nucleation and severing (see section 3.3) to the experimentally measured force-velocity relation. Results for capping, nucleation and severing rates are shown in Table 4.4. They are relatively low. With the filament density of about 280 /µm (see Fig. 4.15 *D*), the effective nucleation rate per filament $k_n = k_n^0 - k_n^N n$ is approximately 9 /min. Since filaments polymerize in the freely running cell with about 31 µm/min (the rate of filament elongation equals the rate of filament shortening $n\hat{v}_g^{max} l/z$), we should find a branching point approximately every 3.5 µm along the filament. Filaments in the SR are less than 2 µm long and consequently the branch point density is low. If we keep in mind that new branches grow from attached filaments only, we find about 50 branch points in the SR per µm lateral width.

The capping rate is also low. The model result for the density of capped filaments in the freely running cell is approximately 10 /µm (Fig. 4.15 *D*). We should bear in mind that this is only the number of capped filaments with lengths between z and l_d. Hence, the total number of capped filaments in the SR amounts to 30 /µm (see Fig. 4.15 *E*). In

conclusion, to accomplish a stationary filament number, the newly nucleated filaments are partly compensated for by capping, partly by severing.

In Vinzenz et al. [2012], the authors find on average one branch point every 0.8 µm along a filament by evaluating electron microscopy tomograms. However, this value was measured in NIH 3T3 cells and treadmilling is much slower in those cells than in keratocytes. The capping and nucleation rates in their simulations ($k_{cap} = 0.03$/s, $k_{br} = 0.042$/s) are slightly lower but in the same range as in our fit (Table 4.4). The values used by Schaus et al. [2007] ($k_{cap} = 6.0$/s, $k_{br} = 0.43$/s) are higher.

When the cell touches the cantilever, the total number of filaments first increases during the concave phase because the capping rate decreases with increasing force and severing decreases with shrinking filament length. Later, the filament number decreases again because the ratio of attached to detached filaments decreases and therefore also the nucleation rate. The value in the stalled state is slightly higher than in the freely running cell. However, if we choose a higher value of k_n^N and the number of filaments is lower in the beginning, the rise in filament number can be larger. If we start with a high number of filaments, it can even decrease after a transient increase.

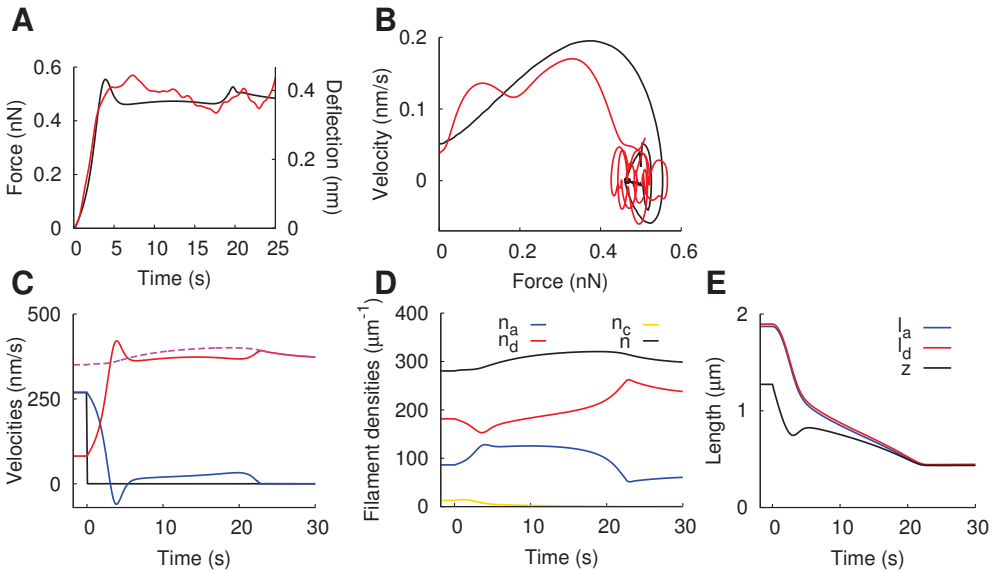

Figure 4.15: Simulation of force-velocity relation with the model including capping, nucleation and severing. (*A, B*) Comparison of simulation (*black*) and control experiment (*red*). (*A*) Time-course of the cantilever deflection, which is proportional to the force exerted on the cell. (*B*) Force-velocity relation obtained from the deflection and deflection velocity. (*C*) Development of the leading edge velocity (*black*), the gel boundary velocity (*blue*) and retrograde flow velocity (*red*). The sum of the latter two (*dashed magenta*) equals the cross-linking rate and is proportional to the filament density. (*D*) Time course of filament densities: (*blue*) attached; (*red*) detached; (*yellow*) capped; (*black*) total. (*E*) Development of filament lengths ((*blue*) attached; (*red*) detached) and the SR depth (*black*). For parameter values see Table 4.4 and Table 4.2, control.

Symbol	Meaning	Value	Units
k_n^0	nucleation rate	0.6	s^{-1}
k_n^N	limiting factor of nucleation rate	0.0016	µm/s
k_c^{max}	capping rate	0.05	s^{-1}
k_{sev}	binding rate of cofilin	0.0167	$s^{-1}µm^{-1}$
$T_{1/2}$	half life of ATP-actin within filament	6.0	min
$\hat{v}_g^{max}$	saturation value of gel cross-linking rate	0.075	$µm^2$/min
$\bar{l}$	saturation length of cross-linking rate	10.0	
v_p^{max}	saturation value of polymerization velocity	46.2	µm/min
ξ	friction coefficient of actin gel to adhesion sites	0.175	nN s/$µm^3$

Table 4.4: List of additional model parameters for capping, nucleation and severing, and their values in Fig. 4.15. Below the double line are parameters, which appear in the model with constant filament density also, but the value of which changed in the fit with the extended model. All other model parameters remained as in Table 4.2, control.

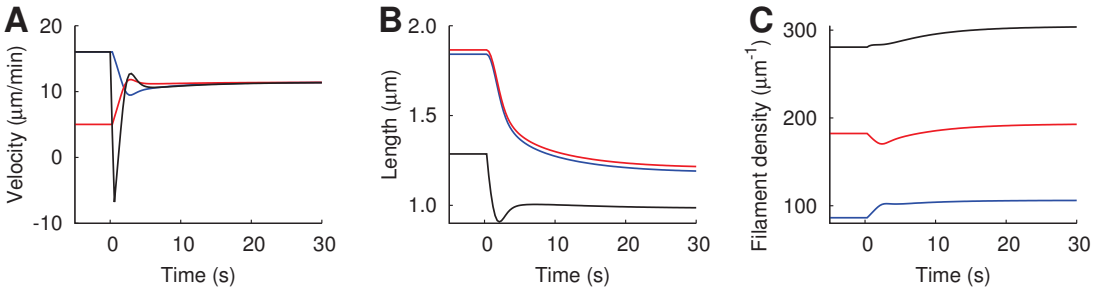

Figure 4.16: Adaptation of the lamellipodium to a constant force below the stall force. The external force is increased from 0 to 0.05 nN/µm during a simulation. The time point of force application is set to 0 s. (*A*) Development of the leading edge velocity (*black*), gel boundary velocity (*blue*) and retrograde flow velocity (*red*). (*B*) Development of filament lengths ((*blue*) attached; (*red*) detached) and the SR depth (*black*). (*C*) Time course of filament densities: (*blue*) attached; (*red*) detached; (*black*) total. Parameter values are the same as in Fig. 4.15 (Table 4.4).

Adaptation to constant force

As we have seen, the measured force-velocity relation of keratocytes differs from the stationary force-velocity relation (Fig. 4.6) because the cytoskeleton dynamically adapts to the increasing external force. We are now interested in the adaptation of the lamellipodium to a constant force. Hence, we calculate the solution of our dynamical system and apply a constant external force weaker than the stall force at a certain time point which is set to 0 s in Fig. 4.16. The results resemble those of the cantilever simulations. Since the filaments are floppy, we observe a velocity drop, similar to the initial velocity

drop. The SR depth decreases and increases again, and the filaments bend and straighten out again as they shorten according to the external force (Fig. 4.16 *B*). The retrograde flow slowly increases (Fig. 4.16 *A*). The number of detached filaments first decreases and then increases as the total filament density increases to the stationary value at the stronger force (Fig. 4.16 *C*). The major difference to the dynamic force-velocity relation is that the leading edge velocity even becomes negative (Fig. 4.16 *A*). This was not observed experimentally since a backward movement immediately also entails decreasing deflection of the cantilever and weaker forces. Nevertheless, the results shown here underline that the dynamic force-velocity relation mainly gets its characteristic shape due to the adjustment of the filament lengths, the SR depth and the retrograde flow to the stationary values at a stronger external force.

4.3 Transient formation of lamellipodia

4.3.1 Excitability

Excitability can lead to transient formation of lamellipodia

We examine the regime with a filament density $n = 0$ in the stationary state (see Fig. 4.3, black regions). This state corresponds to the existence of no lamellipodium. Interestingly, the system may exhibit excitability here. Small perturbations are amplified before the system returns to the steady state. An example for a solution is shown in Fig. 3.6. The filament density transiently increases from $\sim 1/\mu\text{m}$ to $\sim 150/\mu\text{m}$ before it drops to zero. In Fig. 4.17, the height of the transient is shown as a function of the nucleation rate. It gets large close to the transition to the stable lamellipodium. Hence, when a filament is nucleated from the actin cortex by chance, the total number of filaments increases before it drops to zero again. We can interpret this as the transient formation of a lamellipodium. While the number of filaments drops to very low values, they keep polymerizing, grow longer and longer, and exert weaker and weaker forces. However, if there are no filaments, the length of a filament is not very meaningful anymore. We can consider the lamellipodium as vanished if $n < 1$. We introduce a threshold for polymerization, $v_p = 0$ if $n < 1$, to prevent unbounded growth. To describe the transient formation of lamellipodia, we first neglect retrograde flow ($\dot{y}_g = v_{link}$). We include it again later on when fitting measured leading edge time courses.

In Fig. 4.18, the initial values of the integration are low filament number ($n_a = 1$, $n_d = 0.01$) and short filaments ($l_a = l_d = 2.7$ nm). At random time points, we increase the number of attached filaments by one, which corresponds to the nucleation of a single filament. If the number of filaments $n < 1$ at that time point, we also set the length of filaments to the initial value again, since the newly nucleated filament should be short. The simulation shows that a small perturbation, that is the nucleation of a single filament, is sufficient to induce a huge increase in filament density and the formation of a lamellipodium. As the number of filaments increases, the filaments rapidly grow

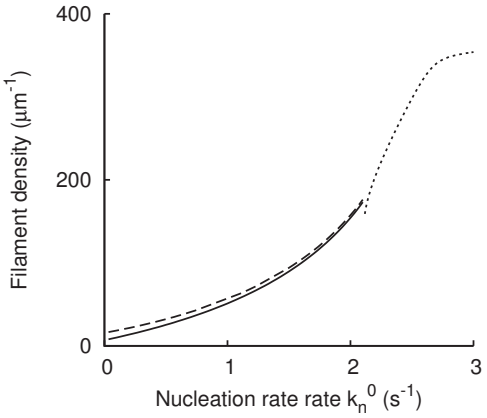

Figure 4.17: Amplitude of the transient in the excitable regime as a function of the nucleation rate. (*Solid line*) With $n_a(0) = 1/\mu\text{m}$ and $n_d(0) = 1/\mu\text{m}$ as initial conditions. (*Dashed line*) With $n_a(0) = 5/\mu\text{m}$ and $n_d(0) = 5/\mu\text{m}$ as initial conditions. All other parameters as in Fig. 4.18. Retrograde flow is set to zero. (*Dotted line*) Value of the filament density of the stable fixed point existing above $k_n^0 = 2.1/\text{s}$ (see also Fig. 4.3).

to about 2 μm. When the density has reached its maximum and decreases again, the filaments continue to grow until the density drops below the threshold for polymerization. The SR depth however remains small. We see that the rise in the number of capped filaments is about 4-fold larger than in the number of attached and detached filaments. On the one hand, this is due to high capping and nucleation rates. Newly nucleated filaments get capped quickly. On the other hand it is due to large ratio of l to z. It takes a while until capped filaments become shorter than the SR depth and hence they accumulate. However, the rise occurs during the phase when filaments are about 2 μm long. The fact that they grow even longer is not essential to achieve a transient increase in filament density. When we compare our simulation with the simplified model here with a solution of the full, time-dependent model, we see that the density of attached and detached filaments increases a bit stronger in the full model (Fig. 3.6).

If we extended the model to two dimensions and described the circumference of the cell, such excitability could give rise to waves traveling around the cell (see Enculescu et al. [2010]). Since filaments are nucleated under a certain angle, the increase in filament number "infects" neighboring regions by inducing perturbations there that are then also amplified. This can lead to a nucleation wave of high filament density encircling the cell, as it has been described experimentally (Asano et al. [2009]).

Fit of experimental data

Alternating protrusions and retractions of the leading edge have also been observed by Koestler et al. [2008] and Burnette et al. [2011]. Moreover, the structural dynamics of the actin cytoskeleton are described in those publications. Filaments grow, more or less perpendicular to the leading edge, during the phase of protrusion. As they get longer, they from arcs that orient parallel to the leading edge and are retracted. The described mechanism agrees well with our observations that lamellipodia are formed by nucleation from the cortex and vanish while filaments grow long and are cross-linked into the gel. Since the filaments get much longer than the SR depth, they have to bend and it is very likely that they form arcs. In Fig. 4.19, we have fitted our model to

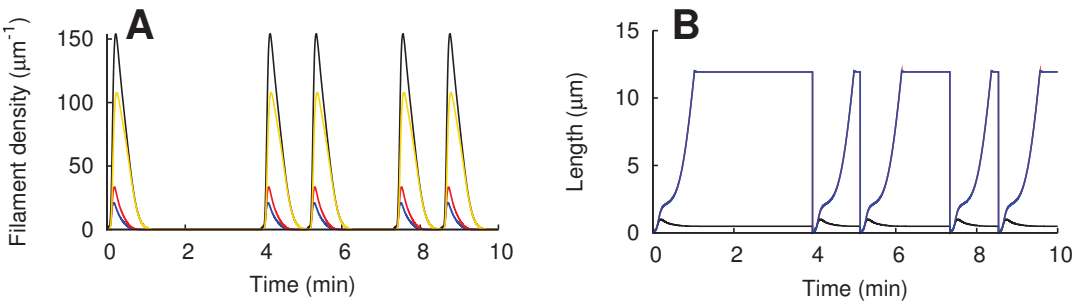

Figure 4.18: Simulation in the regime with stationary filament density $n = 0$. At random time points, the density of attached filaments is incremented by one, which corresponds to random nucleation of a filament from the cortex. The system exhibits excitability and the transients describe lamellipodium formation and collapse. (*A*) Density of attached (*blue*), detached (*red*) and capped (*yellow*) filaments and total filament density (*black*). (*B*) Filament length and SR depth (*black*). Attached (*blue*) and detached (*red*) filaments are almost equally long. Parameters are $k_n^0 = 2.0/\text{s}$, $k_c^{max} = 1.1/\text{s}$, $k_{sev} = 0.05\ \text{s}^{-1}\mu\text{m}^{-1}$, all other values like in Table 4.4. Retrograde flow is set to zero.

the experimental results from Burnette et al. [2011]. We have included retrograde flow again since otherwise the leading edge would not move backwards. The leading edge time course complies very well with the experimental data (Fig. 4.19 *B*, *D*).

Also in agreement with the measurement (see Fig. 5 *g, h* in Burnette et al. [2011]), the retrograde flow reaches a maximum when the leading edge is at its maximum retraction velocity (Fig. 4.19 *C*). The retrograde flow increases when the filament density decreases, because the cross-linking rate v_{link} decreases more quickly than the filament force f_0 and the factor g_2 in Eq. 3.38 increases. We have to treat this result with caution since retrograde flow was fitted for $\frac{\mu L}{4\eta v_{link}} < 1$ (see section 3.2). For $v_{link} = 0$, the retrograde flow should be proportional to the filament force f_0 only. However, Burnette et al. show that retraction of the leading edge is myosin independent and still takes place when cells are treated with Blebbistatin and the power stroke of myosin is inhibited. The modeling results suggest an explanation for the increase in retrograde flow, independent of myosin activity. When cells are treated with Blebbistatin, the period of retraction and protrusion events increases and they occur less frequently (see Fig. 4 *e* in Burnette et al. [2011]). We can reproduce this finding with our model simply by reducing the contractile stress in the gel μ (Fig. 4.20).

We can now make predictions by changing other parameters. If we decrease the nucleation rate k_n^0, we get further into the regime with $n = 0$ as stationary state. The amplitude of the transient of n decreases (Fig. 4.17). The duration decreases also, hence the frequency of subsequent protrusions and retractions increases. If we decrease the capping rate or increase the nucleation rate, we will quickly reach a stationary state with $n > 0$. The oscillations will vanish and we will observe the formation of a stable protrusion. An important conclusion from our modeling results is that the transient formation of the lamellipodium occurs simply due to the excitability of the system. No

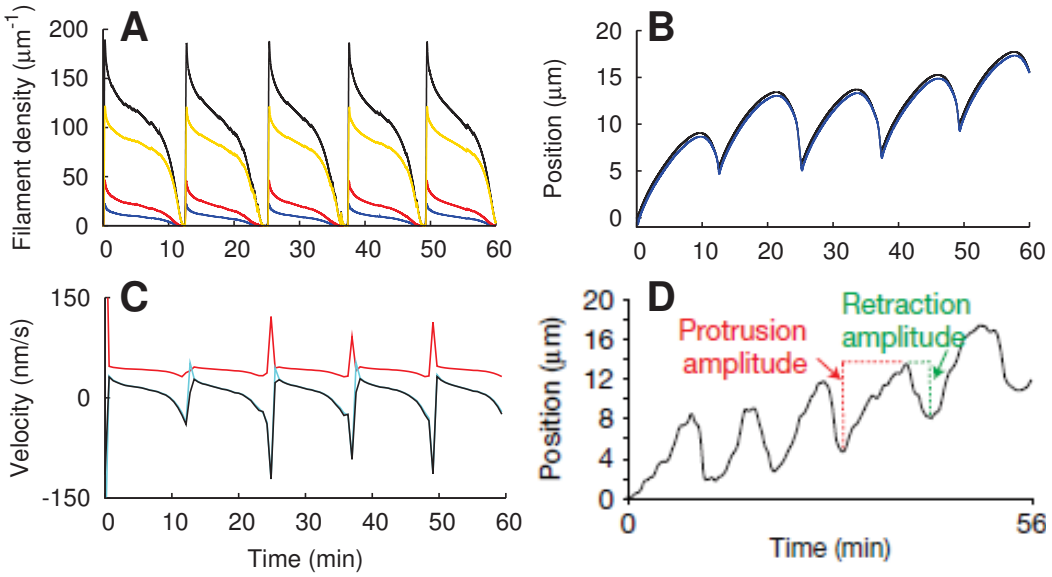

Figure 4.19: Simulation like in Fig. 4.18 (retrograde flow included), fitted to the experimental data from Burnette et al. [2011]. (*A*) Density of attached (*blue*), detached (*red*) and capped (*yellow*) filaments and total filament density (*black*). (*B*) Position of the leading edge (*black*) and the gel boundary (*blue*). (*C*) Velocities of the leading edge (*black*) and the gel boundary (*light blue*) and retrograde flow velocity (*red*). (*D*) Part of Fig. 5 *b* from Burnette et al. [2011] for comparison. Parameters are $k_n^0 = 1.0/\text{s}$, $k_c^{max} = 0.25/\text{s}$, $v_p^{max} = 36\ \mu\text{m/min}$, $\tilde{v}_g^{max} = 0.03\ \mu\text{m}^2/\text{min}$, $k_{sev} = 0.05\ \text{s}^{-1}\mu\text{m}^{-1}$, $\xi = 0.18\ \text{nN s}/\mu\text{m}^3$, $\mu = 4.17\ \text{pN}/\mu\text{m}^2$. Membrane tension is characterized by an external force $f_{ext} = 0.0139\text{nN}/\mu\text{m}$. All other values like in Table 4.4.

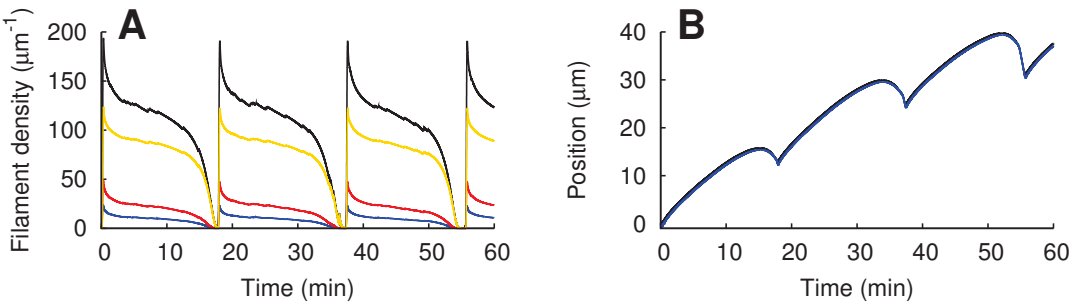

Figure 4.20: The same simulation like in Fig. 4.19, but with a myosin contractility μ of 1.67 pN/μm^2 instead of 4.17 pN/μm^2. (*A*) Density of attached (*blue*), detached (*red*) and capped (*yellow*) filaments and total filament density (*black*). (*B*) Position of the leading edge (*black*) and the gel boundary (*blue*). The increase in period induced by treatment with Blebbistatin is reproduced (see Burnette et al. [2011] Fig. 4).

change in concentration of signaling molecules is necessary to induce the protrusion.

4.3.2 Oscillations

Another way of describing the transient formation of lamellipodia is by oscillations. We find parameter regimes where the filament density is very low ($\sim 1/\mu$m) most of the time and periodically increases (Fig. 4.21). During the phase with low filament density, the cross-linking rate is also low and the filaments get longer because polymerization is faster than cross-linking. The pulling force of attached and pushing force of detached filaments decreases with increasing filament length. Consequently, the detachment rate of attached filaments decreases also and the number of attached filaments increases. The higher the number of attached filaments, the more filaments are nucleated, which leads to the increase in filament density. Now the cross-linking rate also goes up, filaments shorten and the force increases. Almost all filaments disrupt from the membrane and the detached filaments quickly get capped so that the filament density drops again.

The fact that the filament length increases during the phase with low filament density is similar to the simulation in the excitable regime (Fig. 4.18). However, because first the number of attached filaments that exert a pulling force goes up, the membrane hardly moves as the filament density increases (Fig. 4.21 *C*). Only when the number of attached filaments decreases and the number of detached filament increases, the membrane jerks forward. When we include retrograde flow, the membrane moves backwards most of the time and forward only for a very short time, which does not agree with the leading edge time course measured in Burnette et al. [2011] (Fig. 4.19 *D*). We also have to keep in mind, that the oscillatory dynamics of our model with the stationary approximation not necessarily reflect the time course of the full time-dependent model. In a 2d model, oscillatory dynamics would correspond to the periodic formation and retraction of a lamellipodium around the whole circumference of the cell ("pulsing").

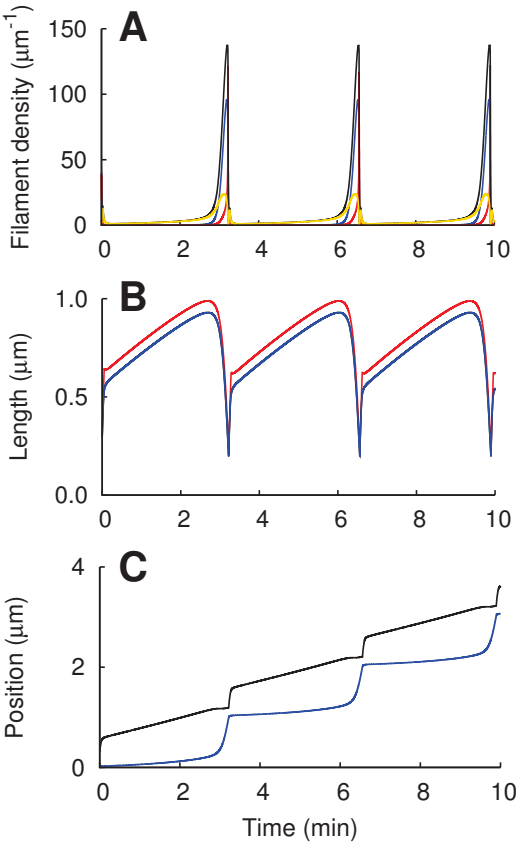

Figure 4.21: Oscillatory solution of the model that shows large variations in filament density and can be interpreted as the periodic formation and retraction of a lamellipodium. Retrograde flow is set to zero. (*A*) Density of attached (*blue*), detached (*red*) and capped (*yellow*) filaments and total filament density (*black*). (*B*) Length of attached (*blue*) and detached (*red*) filaments. The length of attached filaments almost equals the SR depth (*black*). (*C*) Position of the leading edge (*black*) and the gel boundary (*blue*). Parameters are $k_a = 0.2$/s, $k_d^0 = 0.3$/s, $k_c^{max} = 3$/s, $v_p^{max} = 12$ µm/min, $\tilde{v}_g^{max} = 0.03$ µm^2/min, all other values like in Table 4.4.

5 Summary and conclusion

5.1 The model

Cell motility is a vital process that is important for embryonic development, wound healing and immune response, but also leads to cancer metastasis. We used mathematical modeling to describe the formation and protrusion of lamellipodia during cell crawling. Actin filaments in the semiflexible region (SR) at the leading edge of the lamellipodium polymerize and push the membrane. They can also attach to the membrane and hold it back. Further towards the cell body, the filaments are cross-linked into an actin gel.

During stationary motion, the maximum polymerization rate sets the protrusion velocity if it is lower than the maximum cross-linking rate, because otherwise filaments would shorten. However, usually the rate of cross-linking is lower than the maximum polymerization rate and limits the velocity since the leading edge cannot move faster than the gel boundary. When cells move with a constant velocity, the forces that filaments in the semiflexible region exert on the membrane have to balance viscous and external forces. The length of filaments and their degree of bending adapts accordingly to those parameters. Longer filaments exert weaker forces. Also the number of attached filaments, that exert a pulling force when stretched out, can change. The leading edge may also exhibit oscillatory motion. In that case, the binding state and length of the filaments vary. They determine the force, and therefore the velocity of the leading edge membrane and the depth of the SR, which in turn influence filament length and attachment.

The model describes a one-dimensional cross-section through the thin lamellipodium. The basic new model features incorporated in this thesis are the retrograde flow in the actin gel, the parameter dependence of the cross-linking rate and a computationally feasible description of nucleation of new and capping and severing of existing filaments.

5.2 Force-velocity relation

The model can very well reproduce experimentally measured force-velocity curves of keratocytes. It can explain the velocity drop upon cantilever contact and the following concave force-velocity relation up to the stall force. The modeling results also show that the force-velocity relation is a dynamic phenomenon and that the adaptation to the stalled state continues after the stall force has been reached.

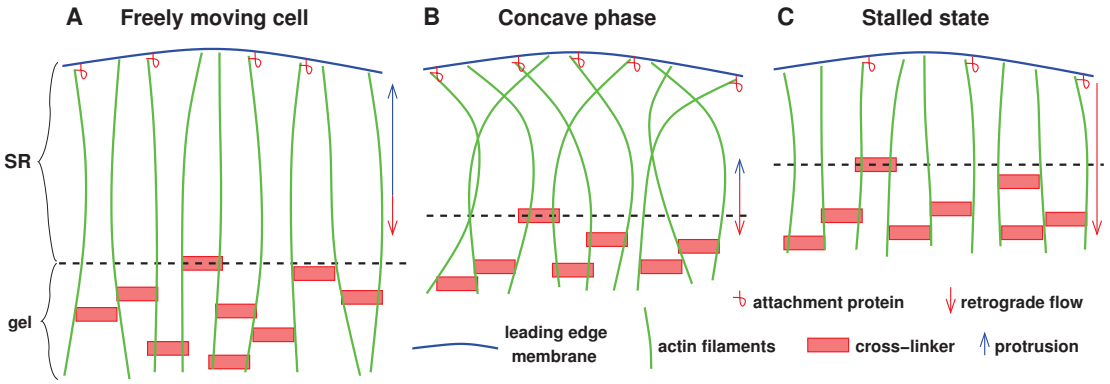

Figure 5.1: Processes in the SR during adaptation to increasing external force exerted by an SFM-cantilever. (*A*) Protrusion velocity is much faster than retrograde flow in the freely running cell during unhindered motion. The depth of the SR and the free filament length are determined by the force per filament required for protrusion. (*B*) Filaments bend and shorten upon contact with the spherical probe. Protrusion velocity is very small and retrograde flow is increasing. (*C*) Free filament length is sufficiently short for transmission of the stall force to the gel. Filaments are stiffer, because they are shorter than in the freely running cell. Retrograde flow in the stalled state is approximately equal to the sum of retrograde flow and protrusion in the freely running cell, and also equal to the polymerization velocity. The force required to drive retrograde flow with the velocity of ongoing polymerization is the stall force, because contractile forces contribute little to retrograde flow in the central fish keratocyte lamellipodium. Figure published in Zimmermann et al. [2012].

During unhindered stationary motion before cantilever contact, cells experience low forces and consequently the actin filaments in the SR are long, about $1-2$ µm. When the cell touches the cantilever, a tiny force of a few pN suffices to overcome the filament forces and almost stop the leading edge motion. However, the gel boundary further back keeps moving and the depth of the SR shrinks. The filaments in the SR bend since they keep polymerizing at an almost unchanged rate. Due to bending, they can now exert a larger force on the leading edge again and the velocity slightly increases. During cross-linking, a larger portion of filament contour length vanishes into the gel if filaments are bent. Therefore they shorten and the length adapts to the increasing external force. The force is transmitted to the gel boundary and the retrograde flow in the actin gel accelerates slowing leading edge motion. Although the rate of polymerization decreases with the increasing force, the leading edge stall force does not stall single filament polymerization. The leading edge stops in the stalled state because polymerization is completely converted into retrograde flow. The whole mechanism is summarized in Fig. 5.1.

The observation that both SR and gel shape the force-velocity relation is confirmed by comparison to other theoretical studies (Zimmermann et al. [2012]). Zhu and Carlsson [2010] investigate a variety of scenarios using a branch point distance of 200 nm along elastic filaments. Their models differ with respect to nucleation dynamics and filament-

membrane attachment mechanisms. The experimentally measured force-velocity relation of the fish keratocyte lamellipodium could not be reproduced. Simulations of branched actin networks made of rigid rod-like filaments with excluded volume effects taken into account (Schreiber et al. [2010]) produce a concave-down force-velocity relation. However, they predict stall forces by a factor of 20-50 too large. Lee and Liu [2009] also find a concave relation with Brownian dynamics simulations of single actin monomers and filaments in a branched network. In order to narrow the range of time scales in their simulations, they use a relatively high depolymerization rate and a filament persistence length of 0.1 μm. Consequently, velocities at half stall force are orders of magnitude faster than in experiments with fish keratocytes and the stall force density is by about one order of magnitude too small. Interestingly, Lee and Liu [2009] emphasize that elasticity of filaments is essential. For stiff filaments, they suppose that the velocity remains constant for all forces as in the autocatalytic branching model by Carlsson [2003]. This model explains the plateau after the initial drop by growing filament density.

No retrograde flow is found in actin networks growing under an AFM cantilever. Nevertheless, the shape of the force-velocity curve of those systems resembles that of keratocytes, though on much different scales. It takes several minutes to reach the stall force which is on the order of 200 nN. The system shows hysteresis when the cantilever is retracted and force is reduced during a measurement (Parekh et al. [2005]). This could be explained by an increasing filament density with increasing force. When the force is reduced to a lower value, the filament density first stays at the higher value, more filaments can exert larger forces and the cantilever moves faster. Weichsel and Schwarz [2010] suggest to explain the hysteresis by a configurational bistability of the actin network. However, those mechanisms have been excluded for the force-velocity relation of fish keratocytes by Heinemann et al. [2011] who repeated the measurement with the same cell after a time lag of $30 - 40$ s. Two repetitions show the same outcome as the first measurement and no hysteresis is observed. The relaxation times of our model are in agreement with the repeated experiments. We can conclude that the mechanisms shaping the force-velocity relation are different for actin networks and the lamellipodium of keratocytes. Moreover keratocytes exhibit an initial velocity drop and none of the mentioned theoretical studies takes that into account. Heinemann et al. [2011] suggest a simple mechanism similar to ours. They describe the initial velocity drop and ensuing increase in velocity by the elastic response of a spring with increasing stiffness, reflecting the adaptation of the filament length in our model.

Our model not only fits the concave force-velocity relation with the correct values of deflection velocities and stall forces but also the measured leading edge and retrograde flow velocities before cantilever contact. Also measurements with cells to which drugs had been applied were fitted and the significant parameter changes are in agreement with the known effects of the drugs. The fact that the model can fit the experiments with an accuracy that is outstanding in the field allows us not only to suggest a mechanism leading to the characteristic shape of the force-velocity relation, but also to draw conclusions on the structure of the keratocyte lamellipodium during unhindered motion. Especially, as a result of the fits, filaments are significantly longer than previously assumed. From electron microscopy pictures of the lamellipodial actin network (Svitkina et al. [1997])

and theoretical considerations (Mogilner and Oster [1996]), it was concluded that the network is highly branched and filaments have a length of about $50 - 200$ nm (Pollard and Borisy [2003]). More recent electron tomograms however revealed that filaments are longer, about 1 µm (Urban et al. [2010], Vinzenz et al. [2012]). Our results support those findings. Filaments significantly shorter than 1 µm do not bend and therefore no transient increase in velocity is observed. Additionally, a variety of stiff rod models, which would apply to short filaments, could not reproduce the measured force velocity relation.

The measured force-velocity curves can be fitted with a model with constant filament density, showing that an increase in filament density by nucleation, as it has been proposed for actin networks, is not the essential mechanism for keratocytes. It would also be difficult to reconcile a substantial change of filament density during a force velocity measurement with the results of the repetition experiments by Heinemann et al. [2011]. When including nucleation into the model, a fit of the data results in a low branch point density of about 38 $/\mu m^2$. This is lower than the observed density of $140 - 270$ $/\mu m^2$ in 3T3 cells (Yang and Svitkina [2011], Small et al. [2011]) but the value might be different for keratocytes since they also show faster protrusion. Moreover, the actual branch point density should be higher because we only account for filament branches that have already grown to the length of the mother filament in our model. Especially if the new filament branch is still very short, the branched filament probably has very similar mechanical properties to a single unbranched filament.

The force-velocity relation of keratocytes is a dynamic phenomenon and the velocity depends on the stiffness of the SFM-cantilever. It describes the behavior of a cell that encounters an obstacle during motion. It does not reflect the velocity of protrusion after a long stationary application of an external force, as for example exerted by surrounding tissue. For comparison, the stationary force-velocity relation was calculated with the parameters resulting from the fit of the dynamic force-velocity relation. Since the filament length can adapt to the external force, protrusion is faster than for the dynamic force-velocity relation. The velocity decreases almost linearly, reflecting the force-velocity relation of the gel due to increasing retrograde flow. With higher capping and nucleation rates, the stationary force-velocity relation exhibits a maximum because the filament density adapts to the increasing external force, similar to the mechanism suggested by the dendritic nucleation model. Different sets of model parameters correspond to different cells types. Measurements of the force-velocity relation have only been published for keratocytes to date. Indeed, our modeling results suggest that the dynamic force-velocity relation might be cell type specific. If the filaments in the lamellipodium are short, no transient increase in velocity will be observed. However, we should note that we have neglected any transient behavior of the gel due to the quasi stationary approximation.

We have not included any signaling events into our model. This is certainly a good approximation for the measurement of the dynamic force-velocity relation which takes $5 - 15$ s. Signaling would need to occur even faster, and its effects must have disappeared after 40 s (repeated measurements). Given additionally, that the model explains a variety of experimental observations starting with the shape of the complete relation on physical

grounds, it seems unlikely that signaling has an essential role in shaping the dynamic force-velocity relation. However, one can imagine that cell signaling, and therefore also our model parameters like nucleation or polymerization rate, change and adapt if a stationary force is applied to the lamellipodium. Our simulations of the stationary force-velocity relation allow for determining whether signaling has a role there by comparing our results with future experiments.

5.3 Formation of stable and transient lamellipodia

Different cell types exhibit a very different shape and dynamics of the lamellipodium. A stability analysis of the model with variable filament density reveals that in some parameter regimes the leading edge shows stationary protrusion, like for keratocytes, whereas it oscillates for other sets of parameters, especially lower attachment and detachment rates, corresponding to different modes of cell motion. In still other parameter regions, the number of filaments drops to zero, describing nonmotile cells that do not form any stable lamellipodia. The modeling results explain how certain parameter changes, like lowering the nucleation rate, can induce transitions from a stable to a collapsing lamellipodium even within the same cell.

No stable lamellipodium can exist, if the nucleation rate is too small compared to capping and severing rates so that filament formation can not balance filament extinction. However, lamellipodia can still form transiently in those regimes. If the number of filaments is incremented randomly during a simulation, which corresponds to the nucleation of a single filament from the actin cortex or actin bundles oriented parallel to the leading edge, the density of filaments goes up transiently, corresponding to the formation of a lamellipodium. Vinzenz et al. [2012] provide experimental evidence that stable lamellipodia can indeed initially form by such a mechanism. They make holes into the lamellipodia of B16 melanoma cells, 3T3 fibroblasts and keratocytes with a microneedle and monitor their edges in the electron microscope while they are healing. They observe that short filaments branch from long filaments that are oriented parallel to the edge of the hole. The newly nucleated filaments initiate the growth of a dendritic actin network filling the hole.

In the model, the filament density decreases after the transient increase and the lamellipodium vanishes again. The remaining filaments grow longer and longer while their number decreases. They have to bend since the depth of the SR remains small. This mechanism describes very well the protrusion and retraction of lamellipodia in PtK1 epithelial cells observed by Burnette et al. [2011]. They show that actin arcs form in the lamellipodium at the peak of the protrusion phase and are then retracted and incorporated into the lamellum. Being oriented parallel to the leading edge, they serve as the base for the protrusion of a new lamellipodium. The same mechanism has been described for B16 melanoma cells before (Koestler et al. [2008]). Our simulations support the finding that actin arcs of the lamellum form at the leading edge and provide a “stiff

substrate for actin filaments in the lamellipodium to push back against to extend the plasma membrane" (Burnette et al. [2011]). An important conclusion from the model is that no cell signaling, and e.g. change in concentration of small GTPases, is necessary to initiate subsequent protrusion and retraction. Random nucleation of single short filaments from long filaments oriented parallel to the edge is sufficient. Burnette et al. [2011] also show that the cycles of protrusion and retraction are independent of myosin activity. When cells are treated with blebbistatin that inhibits myosin ATPase activity, long filaments are less bundled and the apparent boundary between lamellipodium and lamellum is lost. However, oscillations of the leading edge with a larger period and amplitude are still observed. This effect can be reproduced with the model by simply reducing the active contractile stress in the actin gel.

A drawback of the model in the present form is that we neglect the length distribution of attached and detached filaments and assume that they all exhibit the same length. Though this is a very good approximation for stationary and oscillatory motion, it might be important in the case described above. While filaments that form arcs grow very long, the newly nucleated branches are short. We take this effect into account by setting the filament length to short values when the filament density has dropped below one. This is important for observing a new transient increase. However, we assume that filament branches have the same length as the mother filament. The fact that branches are short and can exert larger forces even before the filament density has dropped and we decrease the length is neglected. The shape of the leading edge time courses in the simulations might change if we considered the full length distribution.

Finally, we should note that the SR and gel region distinguished in our model not necessarily correspond to the distinct lamellipodium and lamellum often described (Ponti et al. [2004], Danuser [2009], Shemesh et al. [2009], Gardel et al. [2010], Burnette et al. [2011]). Since cross-linking and adhesion formation occur already in the lamellipodium, the gel boundary is rather located there. The SR describes the very front of the lamellipodium. Actin bundling, adhesion maturation and depolymerization characteristic to the lamellipodium-lamellum interface rather occur in the gel. However, the definition of that interface is not universal but rather author or lab specific. Nevertheless, our model strengthens the idea that lamellipodium and lamellum are no independent networks but the lamellum evolves from and provides mechanical support to the lamellipodium.

In conclusion, the presented model provides insight into how lamellipodia form and protrude, how their structure adapts to external forces and whether cells will eventually move. It will help to understand how wounds heal and under what conditions cancer cells will develop metastases.

Bibliography

V. C. Abraham, V. Krishnamurthi, D. L. Taylor, and F. Lanni. The actin-based nanomachine at the leading edge of migrating cells. *Biophys. J.*, 77(3):1721 – 1732, 1999.

B. Alberts, D. Bray, J. Lewis, M. Raff, K. Roberts, and J. D. Watson. *Molecular biology of the cell*. Garland, 3rd edition, 1994.

W. Alt, M. Bock, and C. Möhl. Coupling of cytoplasm and adhesion dynamics determines cell polarization and locomotion. In A. Chauvière, L. Preziosi, and C. Verdier, editors, *Cell Mechanics: From Single Scale Based Models to Multiscale Modeling*, chapter 4. Taylor & Francis, 2009.

R. Ananthakrishnan and A. Ehrlicher. The forces behind cell movement. *Int. J. Biol. Sci.*, 3:303–317, 2007.

K. I. Anderson, Y. L. Wang, and J. V. Small. Coordination of protrusion and translocation of the keratocyte involves rolling of the cell body. *J. Cell Biol.*, 134(5):1209–1218, 1996.

E. Andrianantoandro and T. D. Pollard. Mechanism of actin filament turnover by severing and nucleation at different concentrations of adf/cofilin. *Molecular Cell*, 24(1): 13 – 23, 2006.

Y. Asano, A. Jiménez-Dalmaroni, T. B. Liverpool, M. C. Marchetti, L. Giomi, A. Kiger, T. Duke, and B. Baum. Pak3 inhibits local actin filament formation to regulate global cell polarity. *HFSP Journal*, 3(3):194–203, 2009.

E. Atilgan, D. Wirtz, and S. X. Sun. Morphology of the lamellipodium and organization of actin filaments at the leading edge of crawling cells. *Biophys. J.*, 89(5):3589 – 3602, 2005.

J. Bain, H. McLauchlan, M. Elliott, and P. Cohen. The specificities of protein kinase inhibitors: an update. *Biochem. J.*, 371(1):199–204, 2003.

A. R. Bausch, F. Ziemann, A. A. Boulbitch, K. Jacobson, and E. Sackmann. Local measurements of viscoelastic parameters of adherent cell surfaces by magnetic bead microrheometry. *Biophys. J.*, 75(4):2038 – 2049, 1998.

H. Berg. *Random walks in biology*. Princeton University Press, 1983.

A. Bernheim-Groswasser, J. Prost, and C. Sykes. Mechanism of actin-based motility: A dynamic state diagram. *Biophys. J.*, 89(2):1411–1419, Aug 2005.

A. Bershadsky, M. Kozlov, and B. Geiger. Adhesion-mediated mechanosensitivity: a time to experiment, and a time to theorize. *Curr. Opin. Cell Biol.*, 18(5):472 – 481, 2006.

S. Bohnet, R. Ananthakrishnan, A. Mogilner, J.-J. Meister, and A. B. Verkhovsky. Weak force stalls protrusion at the leading edge of the lamellipodium. *Biophys. J.*, 90(5): 1810 – 1820, 2006.

D. Bray. *Cell movements - from molecules to motility*. Garland, 2nd edition, 2001.

T. Bretschneider, S. Diez, K. Anderson, J. Heuser, M. Clarke, A. Müller-Taubenberger, J. Köhler, and G. Gerisch. Dynamic actin patterns and arp2/3 assembly at the substrate-attached surface of motile cells. *Curr. Biol.*, 14(1):1 – 10, 2004.

T. Bretschneider, K. Anderson, M. Ecke, A. Müller-Taubenberger, B. Schroth-Diez, H. C. Ishikawa-Ankerhold, and G. Gerisch. The three-dimensional dynamics of actin waves, a model of cytoskeletal self-organization. *Biophys. J.*, 96(7):2888 – 2900, 2009.

C. Brunner, A. Ehrlicher, B. Kohlstrunk, D. Knebel, J. Käs, and M. Goegler. Cell migration through small gaps. *Eur. Biophys. J.*, 35(8):713–719, 2006.

C. Brunner, A. Niendorf, and J. A. Kas. Passive and active single-cell biomechanics: a new perspective in cancer diagnosis. *Soft Matter*, 5:2171–2178, 2009.

D. T. Burnette, S. Manley, P. Sengupta, R. Sougrat, M. W. Davidson, B. Kachar, and J. Lippincott-Schwartz. A role for actin arcs in the leading-edge advance of migrating cells. *Nature Cell Biol.*, 13(4):371–382, 2011.

K. Burridge and K. Wennerberg. Rho and rac take center stage. *Cell*, 116(2):167 – 179, 2004.

A. E. Carlsson. Growth of branched actin networks against obstacles. *Biophys. J.*, 81 (4):1907 – 1923, 2001.

A. E. Carlsson. Growth velocities of branched actin networks. *Biophys. J.*, 84(5):2907–2918, 2003.

A. E. Carlsson. Structure of autocatalytically branched actin solutions. *Phys. Rev. Lett.*, 92:238102, Jun 2004.

A. E. Carlsson. Dendritic actin filament nucleation causes traveling waves and patches. *Phys. Rev. Lett.*, 104:228102, Jun 2010.

E. A. Cavalcanti-Adam, T. Volberg, A. Micoulet, H. Kessler, B. Geiger, and J. P. Spatz. Cell spreading and focal adhesion dynamics are regulated by spacing of integrin ligands. *Biophys. J.*, 92(8):2964 – 2974, 2007.

J. Condeelis and J. W. Pollard. Macrophages: Obligate partners for tumor cell migration, invasion, and metastasis. *Cell*, 124(2):263 – 266, 2006.

G. Danuser. Testing the lamella hypothesis: the next steps on the agenda. *J. Cell Sci.*, 122(12):1959–1962, 2009.

A. T. Dawes and L. Edelstein-Keshet. Phosphoinositides and rho proteins spatially regulate actin polymerization to initiate and maintain directed movement in a one-dimensional model of a motile cell. *Biophys. J.*, 92(3):744–768, 2007.

M. Dembo, D. C. Torney, K. Saxman, and D. Hammer. The reaction-limited kinetics of membrane-to-surface adhesion and detachment. *Proc. R. Soc. London Ser. B*, 234 (1274):55–83, 1988.

P. DiMilla, K. Barbee, and D. Lauffenburger. Mathematical model for the effects of adhesion and mechanics on cell migration speed. *Biophys. J.*, 60(1):15 – 37, 1991.

J. A. Ditlev, N. M. Vacanti, I. L. Novak, and L. M. Loew. An open model of actin dendritic nucleation. *Biophys. J.*, 96(9):3529 – 3542, 2009.

H.-G. Doebereiner, B. Dubin-Thaler, J. Hofman, H. Xenias, T. Sims, G. Giannone, M. Dustin, C. Wiggins, and M. Sheetz. Lateral membrane waves constitute a universal dynamic pattern of motile cells. *Phys. Rev. Lett.*, 97(3):038102, 2006.

I. V. Dokukina and M. E. Gracheva. A model of fibroblast motility on substrates with different rigidities. *Biophys. J.*, 98(12):2794 – 2803, 2010.

K. Doubrovinski and K. Kruse. Cell motility resulting from spontaneous polymerization waves. *Phys. Rev. Lett.*, 107:258103, 2011.

A. Doyle, W. Marganski, and J. Lee. Calcium transients induce spatially coordinated increases in traction force during the movement of fish keratocytes. *J. Cell Sci.*, 117 (11):2203–2214, 2004.

A. D. Doyle, F. W. Wang, K. Matsumoto, and K. M. Yamada. One-dimensional topography underlies three-dimensional fibrillar cell migration. *J. Cell Biol.*, 184(4): 481–490, 2009.

M. Enculescu and M. Falcke. Actin-based propulsion of spatially extended objects. *New J. Phys.*, 13(5):053040, 2011.

M. Enculescu and M. Falcke. Modeling morphodynamic phenotypes and dynamic regimes of cell motion. In I. I. Goryanin and A. B. Goryachev, editors, *Advances in Systems Biology*, volume 736 of *Adv. Exp. Med. Biol.*, pages 337–358. Springer New York, 2012.

M. Enculescu, A. Gholami, and M. Falcke. Dynamic regimes and bifurcations in a model of actin-based motility. *Phys. Rev. E*, 78:031915, Sep 2008.

M. Enculescu, M. Sabouri-Ghomi, G. Danuser, and M. Falcke. Modeling of protrusion phenotypes driven by the actin-membrane interaction. *Biophys. J.*, 98(8):1571 – 1581, 2010.

E. Evans. Probing the relation between force and chemistry in single molecular bonds. *Annu. Rev. Biophys. Biomol. Struct.*, 30(1):105–128, 2001.

M. Faber, M. Enculescu, and M. Falcke. Filament capping and nucleation in actin-based motility. *Eur. Phys. J. ST*, 191:147–158, 2010.

M. J. Footer, J. W. J. Kerssemakers, J. A. Theriot, and M. Dogterom. Direct measurement of force generation by actin filament polymerization using an optical trap. *Proc. Natl. Acad. Sci. USA*, 104(7):2181–2186, 2007.

M. L. Gardel, I. C. Schneider, Y. Aratyn-Schaus, and C. M. Waterman. Mechanical integration of actin and adhesion dynamics in cell migration. *Annu. Rev. Cell Dev. Biol.*, 26:315–33, 2010.

F. Gerbal, P. Chaikin, Y. Rabin, and J. Prost. An elastic analysis of listeria monocytogenes propulsion. *Biophys. J.*, 79(5):2259–2275, 2000.

A. Gholami, J. Wilhelm, and E. Frey. Entropic forces generated by grafted semiflexible polymers. *Phys. Rev. E*, 74(4):041803, 2006.

A. Gholami, M. Falcke, and E. Frey. Velocity oscillations in actin-based motility. *New J. Phys.*, 10(3):033022, 2008.

M. Ghosh, X. Song, G. Mouneimne, M. Sidani, D. S. Lawrence, and J. S. Condeelis. Cofilin promotes actin polymerization and defines the direction of cell motility. *Science*, 304(5671):743–746, 2004.

M. Gracheva and H. Othmer. A continuum model of motility in ameboid cells. *Bull. Math. Biol.*, 66:167–193, 2004.

I. Hecht, M. L. Skoge, P. G. Charest, E. Ben-Jacob, R. A. Firtel, W. F. Loomis, H. Levine, and W.-J. Rappel. Activated membrane patches guide chemotactic cell motility. *PLoS Comput. Biol.*, 7(6):e1002044, 06 2011.

F. Heinemann, H. Doschke, and M. Radmacher. Keratocyte lamellipodial protrusion is characterized by a concave force-velocity relation. *Biophys. J.*, 100(6):1420 – 1427, 2011.

A. Houk, A. Jilkine, C. Mejean, R. Boltyanskiy, E. Dufresne, S. Angenent, S. Altschuler, L. Wu, and O. Weiner. Membrane tension maintains cell polarity by confining signals to the leading edge during neutrophil migration. *Cell*, 148(1 2):175 – 188, 2012.

F. Huber, J. Käs, and B. Stuhrmann. Growing actin networks form lamellipodium and lamellum by self-assembly. *Biophys. J.*, 95(12):5508 – 5523, 2008.

P. A. Iglesias and P. N. Devreotes. Navigating through models of chemotaxis. *Curr. Opin. Cell Biol.*, 20(1):35 – 40, 2008.

L. Ji, J. Lim, and G. Danuser. Fluctuations of intracellular forces during cell protrusion. *Nature Cell Biol.*, 10(12):1393–1400, 2008.

A. Jilkine and L. Edelstein-Keshet. A comparison of mathematical models for polarization of single eukaryotic cells in response to guided cues. *PLoS Comput. Biol.*, 7(4): e1001121, 04 2011.

K. John, P. Peyla, K. Kassner, J. Prost, and C. Misbah. Nonlinear study of symmetry breaking in actin gels: Implications for cellular motility. *Phys. Rev. Lett.*, 100:068101, Feb 2008.

D. Kabaso, R. Shlomovitz, K. Schloen, T. Stradal, and N. S. Gov. Theoretical model for cellular shapes driven by protrusive and adhesive forces. *PLoS Comput. Biol.*, 7 (5):e1001127, 05 2011.

K. Keren, Z. Pincus, G. M. Allen, E. L. Barnhart, G. Marriott, A. Mogilner, and J. A. Theriot. Mechanism of shape determination in motile cells. *Nature*, 453:475–480, 2008.

S. A. Koestler, S. Auinger, M. Vinzenz, K. Rottner, and J. V. Small. Differentially oriented populations of actin filaments generated in lamellipodia collaborate in pushing and pausing at the cell front. *Nature Cell Biol.*, 10(3):306–313, 2008.

K. Kroy. *Viskoelastizität von Lösungen halbsteifer Polymere*. Hieronymus, München, 1998.

K. Kroy and E. Frey. Force-extension relation and plateau modulus for wormlike chains. *Phys. Rev. Lett.*, 77(2):306–309, Jul 1996.

K. Kruse and F. Jülicher. Actively contracting bundles of polar filaments. *Phys. Rev. Lett.*, 85:1778–1781, 2000.

K. Kruse, J. F. Joanny, F. Jülicher, J. Prost, and K. Sekimoto. Generic theory of active polar gels: a paradigm for cytoskeletal dynamics. *Eur. Phys. J. E*, 16:5–16, 2005.

K. Kruse, J. F. Joanny, F. Jülicher, and J. Prost. Contractility and retrograde flow in lamellipodium motion. *Phys. Biol.*, 3(2):130–137, 2006.

P. Krzyszczyk and C. Wolgemuth. Mechanosensing can result from adhesion molecule dynamics. *Biophys. J.*, 101(10):L53 – L55, 2011.

E. Kuusela and W. Alt. Continuum model of cell adhesion and migration. *J. Math. Biol.*, 58:135–161, 2009.

C. I. Lacayo, Z. Pincus, M. M. VanDuijn, C. A. Wilson, D. A. Fletcher, F. B. Gertler, A. Mogilner, and J. A. Theriot. Emergence of large-scale cell morphology and movement from local actin filament growth dynamics. *PLoS Biol.*, 5(9):e233, 08 2007.

L. Le Goff, O. Hallatschek, E. Frey, and F. Amblard. Tracer studies on f-actin fluctuations. *Phys. Rev. Lett.*, 89(25):258101, Dec 2002.

K.-C. Lee and A. J. Liu. New proposed mechanism of actin-polymerization-driven motility. *Biophys. J.*, 95(10):4529–4539, 2008.

K.-C. Lee and A. J. Liu. Force-velocity relation for actin-polymerization-driven motility from brownian dynamics simulations. *Biophys. J.*, 97(5):1295 – 1304, 2009.

H. Levine, D. A. Kessler, and W.-J. Rappel. Directional sensing in eukaryotic chemotaxis: A balanced inactivation model. *Proc. Natl. Acad. Sci. USA*, 103(26):9761–9766, 2006.

H. Lodish, A. Berk, C. A. Kaiser, M. Krieger, M. P. Scott, A. Bretscher, H. Ploegh, and P. Matsudaira. *Molecular Cell Biology*. W.H.Freeman and Company, 6th edition, 2007.

T. P. Loisel, R. Boujemaa, D. Pantaloni, and M.-F. Carlier. Reconstitution of actin-based motility of listeria and shigella using pure proteins. *Nature*, 401:613–616, 1999.

M. Machacek and G. Danuser. Morphodynamic profiling of protrusion phenotypes. *Biophys. J.*, 90(4):1439–1452, 2006.

M. Machacek, L. Hodgson, C. Welch, H. Elliott, O. Pertz, P. Nalbant, A. Abell, G. L. Johnson, K. M. Hahn, and G. Danuser. Coordination of rho gtpase activities during cell protrusion. *Nature*, 461(3):99–103, 2009.

R. E. Mahaffy, C. K. Shih, F. C. MacKintosh, and J. Käs. Scanning probe-based frequency-dependent microrheology of polymer gels and biological cells. *Phys. Rev. Lett.*, 85:880–883, 2000.

Y. Marcy, J. Prost, M.-F. Carlier, and C. Sykes. Forces generated during actin-based propulsion: A direct measurement by micromanipulation. *Proc. Natl. Acad. Sci. USA*, 101(16):5992–5997, 2004.

J. A. May, H. Ratan, J. R. Glenn, W. Losche, P. Spangenberg, and S. Heptinstall. GPIIb-IIIa antagonists cause rapid disaggregation of platelets pre-treated with cytochalasin D. Evidence that the stability of platelet aggregates depends on normal cytoskeletal assembly. *Platelets*, 9(3-4):227–232, 1998.

J. L. McGrath, N. J. Eungdamrong, C. I. Fisher, F. Peng, L. Mahadevan, T. J. Mitchison, and S. C. Kuo. The force-velocity relationship for the actin-based motility of listeria monocytogenes. *Curr. Biol.*, 13(4):329 – 332, 2003.

O. Medalia, I. Weber, A. S. Frangakis, D. Nicastro, G. Gerisch, and W. Baumeister. Macromolecular architecture in eukaryotic cells visualized by cryoelectron tomography. *Science*, 298(5596):1209–1213, 2002.

A. Mogilner. Mathematics of cell motility: have we got its number? *J. Math. Biol.*, 58: 105–134, 2009.

A. Mogilner and G. Oster. Cell motility driven by actin polymerization. *Biophys. J.*, 71 (6):3030–3045, 1996.

A. Mogilner and G. Oster. Force generation by actin polymerization ii: the elastic ratchet and tethered filaments. *Biophys. J.*, 84(3):1591–1605, 2003.

J.-M. Neuhaus, M. Wanger, T. Keiser, and A. Wegner. Treadmilling of actin. *J. Muscle Res. Cell Motil.*, 4:507–527, 1983.

A. Nicolas, B. Geiger, and S. A. Safran. Cell mechanosensitivity controls the anisotropy of focal adhesions. *Proc. Natl. Acad. Sci. USA*, 101(34):12520–12525, 2004.

S. P. Palecek, J. C. Loftus, M. H. Ginsberg, D. A. Lauffenburger, and A. F. Horwitz. Integrin-ligand binding properties govern cell migration speed through cell-substratum adhesiveness. *Nature*, 385:537–540, 1997.

S. H. Parekh, O. Chaudhuri, J. A. Theriot, and D. A. Fletcher. Loading history determines the velocity of actin-network growth. *Nature Cell Biol.*, 7(12):1219–1223, 2005.

C. S. Peskin, G. Odell, and G. Oster. Cellular motions and thermal fluctuations: the brownian ratchet. *Biophys. J.*, 65:316–324, 1993.

T. D. Pollard and G. G. Borisy. Cellular motility driven by assembly and disassembly of actin filaments. *Cell*, 112(4):453 – 465, 2003.

T. D. Pollard, L. Blanchoin, and R. D. Mullins. Molecular mechanisms controlling actin filament dynamics in nonmuscle cells. *Annu. Rev. Biophys. Biomol. Struct.*, 29(1): 545–576, 2000.

T. D. Pollard, L. Blanchoin, and R. D. Mullins. Actin dynamics. *J. Cell Sci.*, 114(1): 3–4, 2001.

A. Ponti, M. Machacek, S. L. Gupton, C. M. Waterman-Storer, and G. Danuser. Two distinct actin networks drive the protrusion of migrating cells. *Science*, 305(5691): 1782–1786, 2004.

M. Prass, K. Jacobson, A. Mogilner, and M. Radmacher. Direct measurement of the lamellipodial protrusive force in a migrating cell. *J. Cell Biol.*, 174(6):767–772, 2006.

S. M. Rafelski and J. A. Theriot. Bacterial shape and acta distribution affect initiation of listeria monocytogenes actin-based motility. *Biophys. J.*, 89(3):2146 – 2158, 2005.

A. J. Ridley, M. A. Schwartz, K. Burridge, R. A. Firtel, M. H. Ginsberg, G. Borisy, J. T. Parsons, and A. R. Horwitz. Cell migration: Integrating signals from front to back. *Science*, 302(5651):1704–1709, 2003.

K. Rottner and T. E. Stradal. Poxviruses taking a ride on actin: New users of known hardware. *Cell Host & Microbe*, 6(6):497 – 499, 2009.

G. L. Ryan, N. Watanabe, and D. Vavylonis. A review of models of fluctuating protrusion and retraction patterns at the leading edge of motile cells. *Cytoskeleton*, 69(4):195–206, 2012.

J. Satulovsky, R. Lui, and Y. li Wang. Exploring the control circuit of cell migration by mathematical modeling. *Biophys. J.*, 94(9):3671 – 3683, 2008.

T. E. Schaus, E. W. Taylor, and G. G. Borisy. Self-organization of actin filament orientation in the dendritic-nucleation/array-treadmilling model. *Proc. Natl. Acad. Sci. USA*, 104(17):7086–7091, 2007.

C. H. Schreiber, M. Stewart, and T. Duke. Simulation of cell motility that reproduces the force–velocity relationship. *Proc. Natl. Acad. Sci. USA*, 107(20):9141–9146, 2010.

C. Selhuber-Unkel, T. Erdmann, M. López-García, H. Kessler, U. Schwarz, and J. Spatz. Cell adhesion strength is controlled by intermolecular spacing of adhesion receptors. *Biophys. J.*, 98(4):543 – 551, 2010.

D. Sept and J. A. McCammon. Thermodynamics and kinetics of actin filament nucleation. *Biophys. J.*, 81(2):667 – 674, 2001.

J. W. Shaevitz and D. A. Fletcher. Load fluctuations drive actin network growth. *Proc. Natl. Acad. Sci. USA*, 104(40):15688–15692, 2007.

T. Shemesh, A. B. Verkhovsky, T. M. Svitkina, A. D. Bershadsky, and M. M. Kozlov. Role of focal adhesions and mechanical stresses in the formation and progression of the lamellum interface. *Biophys. J.*, 97(5):1254 – 1264, 2009.

R. Shlomovitz and N. S. Gov. Membrane waves driven by actin and myosin. *Phys. Rev. Lett.*, 98:168103, Apr 2007.

J. Small, T. Stradal, E. Vignal, and K. Rottner. The lamellipodium: where motility begins. *Trends Cell Biol.*, 12(3):112 – 120, 2002.

J. V. Small, C. Winkler, M. Vinzenz, and C. Schmeiser. Reply: Visualizing branched actin filaments in lamellipodia by electron tomography. *Nature Cell Biol.*, 13:1013–1014, 2011.

J. Stricker, T. Falzone, and M. L. Gardel. Mechanics of the f-actin cytoskeleton. *J. Biomech.*, 43(1):9 – 14, 2010.

A. Stéphanou, E. Mylona, M. Chaplain, and P. Tracqui. A computational model of cell migration coupling the growth of focal adhesions with oscillatory cell protrusions. *J. Theor. Biol.*, 253(4):701 – 716, 2008.

T. M. Svitkina, A. B. Verkhovsky, K. M. McQuade, and G. G. Borisy. Analysis of the actin-myosin ii system in fish epidermal keratocytes: mechanism of cell body translocation. *J. Cell Biol.*, 139(2):397 – 415, 1997.

L. Trichet, O. Campas, C. Sykes, and J. Plastino. Vasp governs actin dynamics by modulating filament anchoring. *Biophys. J.*, 92(3):1081–1089, Feb. 2007.

E. Urban, S. Jacob, M. Nemethova, G. P. Resch, and J. V. Small. Electron tomography reveals unbranched networks of actin filaments in lamellipodia. *Nature Cell Biol.*, 12: 429–435, 2010.

P. Vallotton, G. Danuser, S. Bohnet, J.-J. Meister, and A. B. Verkhovsky. Tracking retrograde flow in keratocytes: News from the front. *Mol. Biol. Cell*, 16(3):1223–1231, 2005.

M. G. L. Van den Heuvel, M. P. de Graaff, and C. Dekker. Microtubule curvatures under perpendicular electric forces reveal a low persistence length. *Proc. Natl. Acad. Sci. USA*, 105(23):7941–7946, 2008.

A. B. Verkhovsky, T. M. Svitkina, and G. G. Borisy. Self-polarization and directional motility of cytoplasm. *Curr. Biol.*, 9(1):11 – S1, 1999.

M. Vicente-Manzanares, C. K. Choi, and A. R. Horwitz. Integrins in cell migration – the actin connection. *J. Cell Sci.*, 122(2):199–206, 2009.

M. Vinzenz, M. Nemethova, F. Schur, J. Mueller, A. Narita, E. Urban, C. Winkler, C. Schmeiser, S. A. Koestler, K. Rottner, G. P. Resch, Y. Maeda, and J. V. Small. Actin branching in the initiation and maintenance of lamellipodia. *J. Cell Sci.*, 125 (11):2775–2785, 2012.

O. I. Wagner, S. Rammensee, N. Korde, Q. Wen, J.-F. Leterrier, and P. A. Janmey. Softness, strength and self-repair in intermediate filament networks. *Exp. Cell Res.*, 313(10):2228 – 2235, 2007.

J. Weichsel and U. S. Schwarz. Two competing orientation patterns explain experimentally observed anomalies in growing actin networks. *Proc. Natl. Acad. Sci. USA*, 107 (14):6304–6309, 2010.

S. Wiesner, E. Helfer, D. Didry, G. Ducouret, F. Lafuma, M.-F. Carlier, and D. Pantaloni. A biomimetic motility assay provides insight into the mechanism of actin-based motility. *J. Cell Biol.*, 160(3):387 – 398, 2003.

F. Wottawah, S. Schikinger, B. Lincoln, R. Ananthakrishnan, M. Romeyke, J. Guck, and J. Käs. Optical rheology of biological cells. *Phys. Rev. Lett.*, 94:098103, 2005.

Y. Xiong, C.-H. Huang, P. A. Iglesias, and P. N. Devreotes. Cells navigate with a local-excitation, global-inhibition-biased excitable network. *Proc. Natl. Acad. Sci. USA*, 107(40):17079–17086, 2010.

H. Yamaguchi, J. Wyckoff, and J. Condeelis. Cell migration in tumors. *Curr. Opin. Cell Biol.*, 17(5):559 – 564, 2005.

S. Yamashiro, Y. Yamakita, S. Ono, and F. Matsumura. Fascin, an actin-bundling protein, induces membrane protrusions and increases cell motility of epithelial cells. *Mol. Biol. Cell*, 9(5):993–1006, 1998.

D. Yamazaki, S. Kurisu, and T. Takenawa. Regulation of cancer cell motility through actin reorganization. *Cancer Sci.*, 96(7):379–386, 2005.

M. Yanai, J. P. Butler, T. Suzuki, H. Sasaki, and H. Higuchi. Regional rheological differences in locomoting neutrophils. *Am. J. Physiol. Cell Physiol.*, 287(3):C603–611, 2004.

C. Yang and T. Svitkina. Visualizing branched actin filaments in lamellipodia by electron tomography. *Nature Cell Biol.*, 13:1012 – 1013, 2011.

M. Zajac, B. Dacanay, W. A. Mohler, and C. W. Wolgemuth. Depolymerization-driven flow in nematode spermatozoa relates crawling speed to size and shape. *Biophys. J.*, 94(10):3810 – 3823, 2008.

A. Zemel, F. Rehfeldt, A. E. X. Brown, D. E. Discher, and S. A. Safran. Cell shape, spreading symmetry, and the polarization of stress-fibers in cells. *J. Phys. Cond. Matter*, 22(19):194110, 2010a.

A. Zemel, F. Rehfeldt, A. E. X. Brown, D. E. Discher, and S. A. Safran. Optimal matrix rigidity for stress-fibre polarization in stem cells. *Nature Phys.*, 6:468–473, 2010b.

J. Zhu and A. E. Carlsson. Effects of molecular-scale processes on observable growth properties of actin networks. *Phys. Rev. E*, 81:031914, Mar 2010.

J. Zimmermann. Modellierung und Analyse des Aktinnetzes in kriechenden Zellen. Diplomarbeit, Freie Universität Berlin, Germany, 2009.

J. Zimmermann, M. Enculescu, and M. Falcke. Leading-edge–gel coupling in lamellipodium motion. *Phys. Rev. E*, 82(5):051925, Nov 2010.

J. Zimmermann, C. Brunner, M. Enculescu, M. Goegler, A. Ehrlicher, J. Käs, and M. Falcke. Actin filament elasticity and retrograde flow shape the force-velocity relation of motile cells. *Biophys. J.*, 102:287–295, Jan 2012.

List of Figures

List of Tables

Acknowledgement

Thank you to
Dr. Martin Falcke for supervision, support, having good ideas, survey of experimental data and always being open for questions; Dr. Mihaela Enculescu supervising me during my diploma for introducing me into the topic, help with all problems and proofreading this thesis; all other (former) members of the group “Mathematical Cell Physiology”; Prof. Josef Käs, Dr. Claudia Brunner and all “Soft Matter”-people from Leipzig for ideas, experimental data and warm welcome; all members of DFG graduate school “computational systems biology” (former IRTG) for creating an inspiring environment and financial support, especially Prof. Edda Klipp; Prof. Bernold Fiedler and SFB 555 for financial support; Dr. Jana Wolf for financial support; Christoph Erlenkämper for helpful discussions; Prof. Andreas Herrmann for supervision at Humboldt University.

Publications

Juliane Zimmermann, Mihaela Enculescu, and Martin Falcke. Leading-edge–gel coupling in lamellipodium motion. *Physical Review E*, 82(5):051925, 2010.

Juliane Zimmermann, Claudia Brunner, Mihaela Enculescu, Michael Goegler, Allen Ehrlicher, Josef Käs, and Martin Falcke. Actin filament elasticity and retrograde flow shape the force-velocity relation of motile cells. *Biophysical Journal*, 102:287–295, 2012.

Juliane Zimmermann, and Martin Falcke. On the existence and strength of stable membrane protrusions. *New Journal of Physics*, submitted.

Berlin, 30. Oktober 2012

Selbständigkeitserklärung

Ich erkläre, dass ich die vorliegende Arbeit selbständig und nur unter Verwendung der angegebenen Literatur und Hilfsmittel angefertigt habe.

Berlin, den 30. Oktober 2012 Juliane Zimmermann